# UTILIZATION OF RESERVOIR CHARACTERIZATION AND HYDRAULIC FRACTURING FOR RESERVOIR STIMULATION MODELING OF ENHANCED GEOTHERMAL SYSTEMS (EGS)

# GELİŞTİRİLMİŞ JEOTERMAL SİSTEMLER (GJS) İÇİN REZERVUAR KARAKTERİZASYONU VE HİDROLİK ÇATLATMA YÖNTEMİYLE REZERVUAR STİMÜLASYON MODELLEMESİ

**ÖZGÜN BOZDOĞAN**

**DOÇ. DR MUSTAFA KEREM KOÇKAR**

**Supervisor**

**Dr. Gence GENÇ ÇELİK**

**Co-Supervisor**

Submitted to

Graduate School of Science and Engineering of Hacettepe University

as a Partial Fulfillment to the Requirements

for the Award of Degree of Master of Science

In Civil Engineering

2022

# ABSTRACT

## UTILIZATION OF RESERVOIR CHARACTERIZATION AND HYDRAULIC FRACTURING FOR RESERVOIR STİMULATION MODELING OF ENHANCED GEOTHERMAL SYSTEMS (EGS)

**Özgün BOZDOĞAN**

**Master of Science, Department of Civil Engineering**

**Supervisor: Assoc. Prof. Mustafa Kerem KOÇKAR**

**Co- Supervisor: Asst. Prof. Dr. Gence GENÇ ÇELİK**

**January 2022, 126 Pages**

This thesis presents the characterization of the crack mechanisms in marble formations, which are likely to be potential reservoir rocks, in the exploration drilling located in a field with high geothermal potential in the south of the Menderes Graben. It covers the characterization of these reservoirs by deep borehole drilling and extensive field studies, creating an artificial enhanced geothermal system using the hydraulic fracturing method, and developing these fracture propagations with numerical modeling. The fracture-strain orientations will be obtained in the field by the exploration tests conducted in the borehole and field characterization studies. Furthermore, the principal stress and crack orientations that control the propagation of fracture-crack occurring in the reservoir rock will be determined in detail and controlled. Then, the principal stress and crack orientations in the reservoir rock will be determined in detail. In-situ stresses and their orientations, which determine the crack mechanisms and characteristics in the potential reservoir rock determined with the help of the input parameters obtained from these studies, will form

the basis of hydraulic fracturing studies. In this way, it will be possible to numerically model the fracture network development in the rock using the hydraulic cracking method. As a result of these studies, an enhanced geothermal system developed with an artificial reservoir with optimum fluid and heat transfer properties will be implemented by controlled stimulation of the crack mechanism in the reservoir rock. In this process, Mfast software educationally supplied by Baker Hughes company will be used for hydraulic fracturing modeling.

**Keywords:** Enhanced Geothermal Systems, In-situ Field Reservoir Characterization, Geological and Engineering Geological Field Studies, MFast Software, 2D Hydraulic Fracturing

# ÖZET

# GELİŞTİRİLMİŞ JEOTERMAL SİSTEMLER (GJS) İÇİN REZERVUAR KARAKTERİZASYONU VE HİDROLİK ÇATLATMA YÖNTEMİYLE REZERVUAR STİMULASYON MODELLEMESİ

**Özgün BOZDOĞAN**

**Yüksek Lisans, İnşaat Mühendisliği Bölümü**

**Tez Danışmanı: Doç. Dr. Mustafa Kerem KOÇKAR**

**Eş Danışman: Dr. Gence GENÇ ÇELİK**

**Ocak 2022, 126 Sayfa**

Bu tez çalışması Menderes Grabeninin güneyindeki yüksek jeotermal potansiyeline sahip bir sahada bulunan araştırma sondajı içerisindeki potansiyel rezervuar kaya olma olasılığı olan formasyonlardaki çatlak mekanizmalarının sondaj içerisinde ve yüzey arazi çalışmalarıyla karakterize edilmesi ve hidrolik çatlatma yöntemiyle bu rezervuarların nümerik olarak modellenerek yapay bir geliştirilmilş jeotermal sistem oluşturulması çalışmalarını kapsamaktadır. Sahada jeotermal elektrik üretimi amaçlı açılan sondajda yapılan özel kuyu araştırma testleri ile elde edilen yüzey arazi karakterizasyonu çalışmaları sonucu elde edilen çatlak ve gerilme yönelimi verileri ile karşılaştırılarak rezervuar kayada meydana gelen kırık-çatlak sistemlerini kontrol eden asal gerilme ve çatlak yönelimlerinin detaylı ve kontrollü olarak belirlenmesi amaçlanmıştır. Buradan elde edilen girdi parametreler yardımıyla potansiyel rezervuar kaya içerisindeki çatlak mekanizmalarını ve karakterini belirleyen yerinde (in-situ) gerilmeler ve bunların yönelimleri hidrolik çatlatma çalışmalarına temel teşkil edecektir. Bu sayede kaya

içerisinde meydana gelecek çatlak ağı gelişiminin hidrolik çatlatma yöntemiyle nümerik olarak modellenmesi sağlanacaktır. Bu çalışmaların sonucunda rezervuar kaya içindeki çatlak mekanizmasının kontrollü olarak stimulasyonu ve optimum akışkan ve ısı transferi özelliklerine sahip yapay bir rezervuar ile buna bağlı olarak yapay bir geliştirilmilş jeotermal sistem oluşturulacaktır. Hidrolik çatlak yönelerimlerinin modellemesinde Baker Hughes şirketinin eğitim amaçlı olarak tarafımıza sağladığı Mfast yazılımı kullanılmıştır.

**Anahtar Kelimeler:** Geliştirilmiş Jeotermal Sistemler, Yerinde Saha Rezervuar Karakterizasyonu, Hidrolik Çatlatma Modellemesi, Jeolojik ve Mühendislik Jeolojisi Saha Araştırması, MFast Yazılımı, 2 Boyutlu Hidrolik Çatlatma Modellemesi.

# ACKNOWLEDGMENT

Foremost, I would like to express my sincere gratitude to my thesis advisor, Assoc. Prof. Mustafa Kerem KOÇKAR for the endless support on my Master of Science Thesis. This thesis would not have been possible without his patience, enthusiasm, guidance, motivation, and immense knowledge. Working with him has been a genuine pleasure and privilege.

I want to express my deepest appreciation to Prof. Dr. Haluk AKGÜN, Prof. Dr. Mustafa ŞAHMARAN, Prof. Dr. Berna UNUTMAZ, and Assoc. Prof. Dr. Mustafa Abdullah SANDIKKAYA, as jury members, for their helpful comments. It has been an honor to have them on my jury committee.

I would like to thank Dr. Gence GENÇ ÇELİK, who guided me to this field and planted this thesis's seeds.

I am profoundly thankful to Prof. Dr. Haluk AKGÜN, the coordinator of the TÜBİTAK 1001/119Y535 project, for his support and contributions. Also I would like to thank Mrs. Arzu Arslan KELAM, Mr. Selim CAMBAZOĞLU, Asst. Prof. Dr. Ayten KOÇ, Mrs. Gözde Pınar YAL ÖNDER and Mr. Yusuf Emrah YILMAZ, who took part in the same project as a researcher, for their contributions.

I would like to thank my mother, who was my first teacher, and my whole family members for their support throughout my whole life.

I would like to express my deepest thanks to my significant other, Research Assistant Ebru Burcu YARDIMCI, for her patience, encouragement, and light to me on this path.

Besides, I would like to express my gratitude to Baker Hughes company for their provided software.

Finally, I would like to thank the Gazi University Faculty of Technology and my valuable colleagues and professors for their endless support.

# TABLE OF CONTENT

# LIST OF FIGURES

# LIST OF TABLES

# SYMBOLS

| | | |
|---|---|---|
| $\sigma_1$ | Maximum Principal Stress | kPa |
| $\sigma_2$ | Intermediate Principal Stress | kPa |
| $\sigma_3$ | Minimum Principal Stress | kPa |
| $\varepsilon_a$ | Axial Strain | Fraction |
| $\varepsilon_d$ | Diametric Strain | Fraction |
| $\Delta l$ | Length Variation | m |
| $l_o$ | Initial Length | m |
| $\Delta D$ | Diametrical Variation | m |
| $D_0$ | Initial Diameter | m |
| P | Load | Kg/f |
| $\nu$ | Poissons Ratio | Fraction |
| $D_e$ | Equivalent core diameter | $cm^2$ |
| $l_s$ | Uncorrected Point Load Strength Index | kPa |
| $l_{s(50)}$ | Corrected Point Load Strength Index | kPa |
| E | Young's Modulus | GPa |
| $K_{ıc}$ | Fracture Toughness | $MN/m^{1.5}$ |
| $\tau$ | Shear Stress | kPa |
| $\mu$ | Viscosity | Pa.s |
| $\gamma$ | Shear Rate | $s^{-1}$ |
| K | Consistency Index | $kPa.s^n$ |
| n | Flow Behaviour Index | Dimensionless |
| $L_c$ | Filtercake Thickness | cm |

| | | |
|---|---|---|
| $V_L$ | Volume Loss | $m^3$ |
| C | Mass Concentration | $kg/m^3$ |
| $\Phi_c$ | Filtercake permeability | cm/h |
| $\rho$ | Density | $kg/m^3$ |
| ul | Leak-off Velocity | $cm/min^{0.5}$ |

# 1.INTRODUCTION

## 1.1. Introduction

In today's world, it is seen that energy need and consumption has been on an increasing trend for a long time, and this trend will continue in the coming decades. Considering clean and environmentally friendly renewable energy sources, demanding this as a necessity has now become a condition that every country and individual must accept. Fossil resources such as coal and oil, which pollute the environment and nature and decrease reserves, need to be gradually replaced by green energy: wind, solar, and geothermal energy. Among these, the importance of geothermal energy is increasing day by day. This is because geothermal energy can profoundly contribute to economic and social goals, such as meeting the rapidly increasing energy needs. Geothermal power plants have a little negative impact on the environment thanks to their high capacity and easy installation, low noise level, generosity against air pollution. This way, geothermal power plants can be built in and near settlements-the results in lower energy transmission and infrastructure costs. Today, 24 countries produce electrical energy using geothermal energy, applying conventional (classical) geothermal methods. At the same time, the electrical energy that can be produced with conventional geothermal systems is 72 Giga Watt electrical (Tester and Smith, 1977; Sanyal and Butler, 2005). It is possible to double these values with the hydraulic fracturing method, which emerged in the third quarter of the 20th century and is still being developed. Hydraulic fracture allows geothermal systems to increase the potential electrical power generation to 168 GWe. The United States Department of Energy estimates that 100 GW of electricity will be produced by 2050 with the application of the Advanced Geothermal System method and has funded around $4.45 million (IEA, 2011., Richter, 2018), while the International Geothermal Agency predicts this value as 80 Gigawatt and the International Geothermal Agency highly supports that world CO2 emission has to reach near-zero at 2050.

The view of Turkey’s perspective is highly similar to the world. Energy demand is drastically increasing. According to Lally (2011) and the Geothermal Energy Authority (2012), the electricity network is projected to grow 6-8% annually until 2020, with an

increase of 50000 MW. The total installed power plant capacity in Turkey is 52,911 MW as of 2011 (EMRA, 2012). Considering the 351 electricity generation licenses granted in 2011, the installed capacity exceeds 63000 MW (EMRA, 2012). The capacity estimations made by TEIAS (2015) are based on the currently installed power plants, the licenses obtained, and the plants still under construction. Only reliable production and project production capacities were used to calibrate each scenario. TEIAS calculated these scenarios by including high and low demand series with an average of 7.5% and 6.5% for 2011 to 2020, respectively.

In the light of these results, the expected energy deficit based on demand and capacity types is expected to start between 2016 and 2020. However, it should be noted that as of 2011, Turkey has been able to use 77% of its total installed power. Thus, the importance of existing capacity increases. Accordingly, it can be said that the energy deficit in Turkey will occur earlier than the estimated date (EMRA, 2012). Therefore, the energy produced from the enhanced geothermal system is an essential alternative solution to reduce or even eliminate the risk. As of 2010, the total installed power based on geothermal energy is 94.2 MW. With the participation of the licensed area, the energy production capacity of geothermal fields in Turkey is expected to reach approximately 400 MW (TEIAŞ, 2015). However, even if the total licensed energy production is considered, it shares approximately 1% of the total electricity production in Turkey (EMRA, 2012). Considering Turkey's view on renewable energy, this rate is meager and should be increased. Field development should be planned to increase the share of geothermal energy in total energy production.

Considering all these, it is evident that Turkey needs to improve its energy production capability with proper and sustainable solutions. Although Turkey has a very high geothermal potential (Figure 1) and ranks 7th in the world in this regard, there is currently no study or project in which any Advanced Geothermal Systems are applied. (Kaygusuz, 2004; Basel vd., 2010; Holm vd., 2010 ve Jeotermal Enerji Kurumu, 2017).

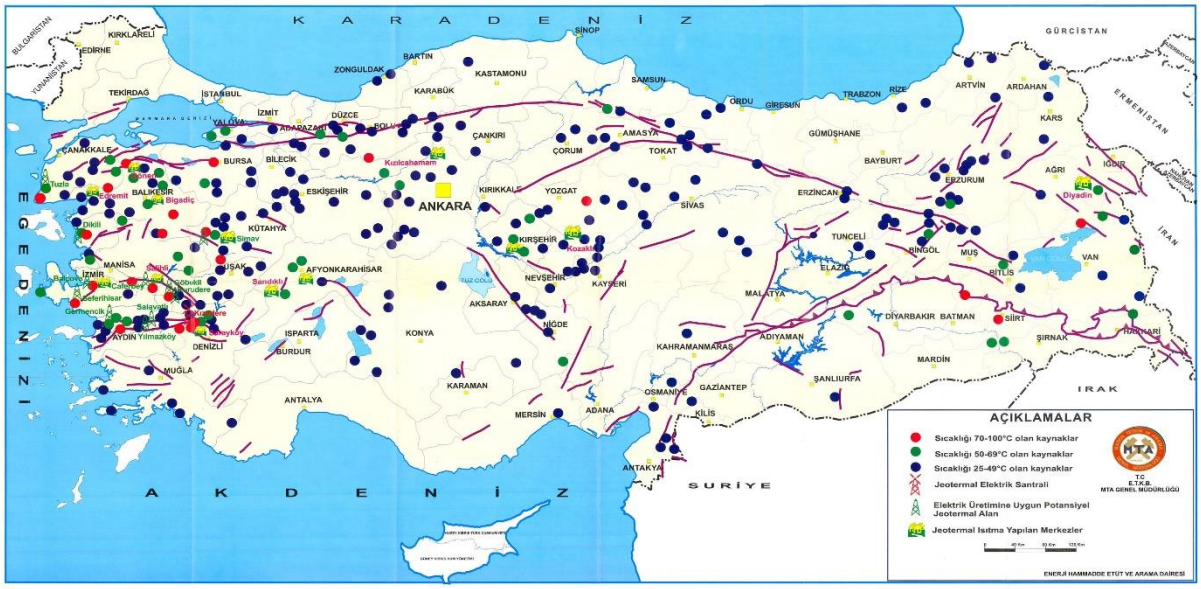


Figure 1. Turkey's distribution of geothermal resources and applications map. Taken from General Directorate of Mineral Research and Exploration

While Turkey has such a high potential even in terms of conventional geothermal energy, it has an undeniable advantage in Enhanced Geothermal Systems (EGS). Conventional methods are used in areas with an underground reservoir and other necessary elements. In addition, another technique has emerged as a technique where there is no geothermal fluid reservoir but creating a reservoir by injecting water from the wells to be drilled and generating electricity by using the geothermal fluid (water and/or steam) to be obtained from this fluid. This application has two different names: Enhanced Geothermal Systems (EGS) and Hot Dry Rock (HDR). With this method, underground heat is evaluated and is used as a source. Production trials with this technology started in the 1970s.

## 1.2 Enhanced Geothermal Systems Concept

Los Alamos Scientific Laboratory first studied the concept of Hot Dry Rock in New Mexico in the early 1970s (Potter et al., 1974). The idea was based on injecting water into the crack system with the help of an injection well by cracking the impermeable high-temperature dry rock at depth and regenerating the heated water by the rock (Figure 2).

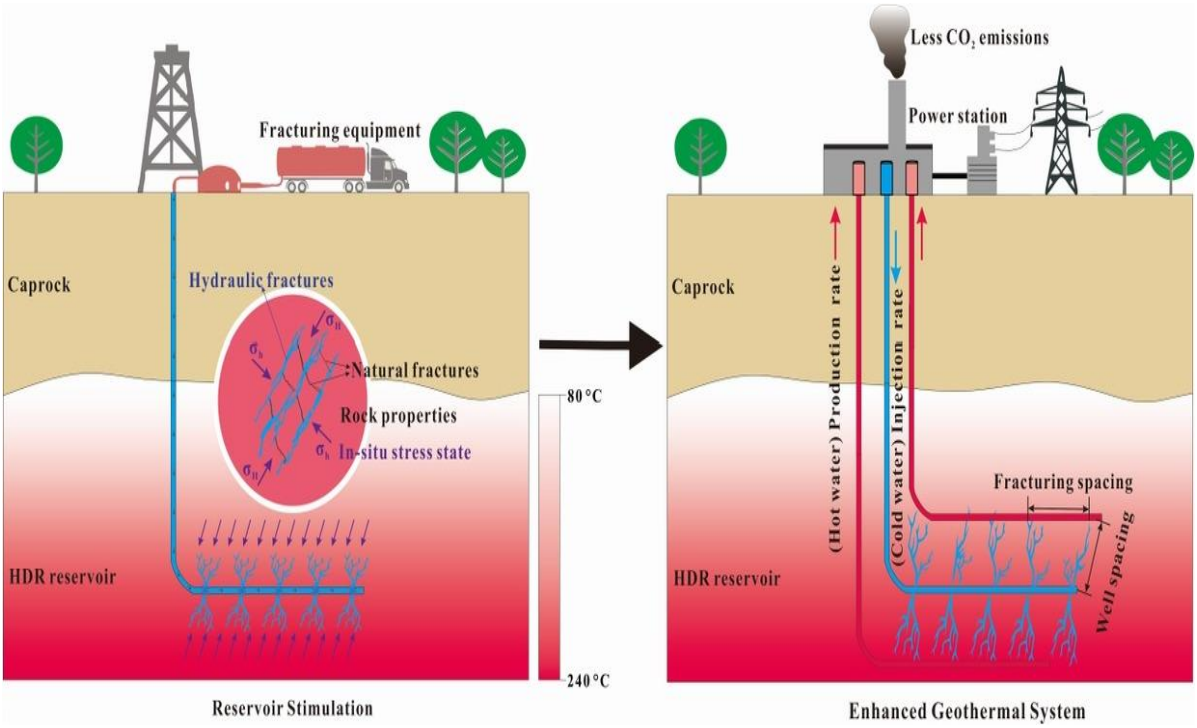


Figure 2. Enhanced Geothermal System Concept (Lei et al., 2020)

This method aims to artificially obtain the permeability and water parameters, which are the requirements of traditional geothermal energy. Since a conventional geothermal reservoir needs three parameters: heat, permeability, and fluid (Figure 3) to operate efficiently, eliminating two factors provides a huge advantage. Also, this method allows reaching higher temperature values. After successful results from the first application, research on the application of developed geothermal systems has increased. In order to obtain the best results in various implementation stages, multidisciplinary studies were needed in this area.

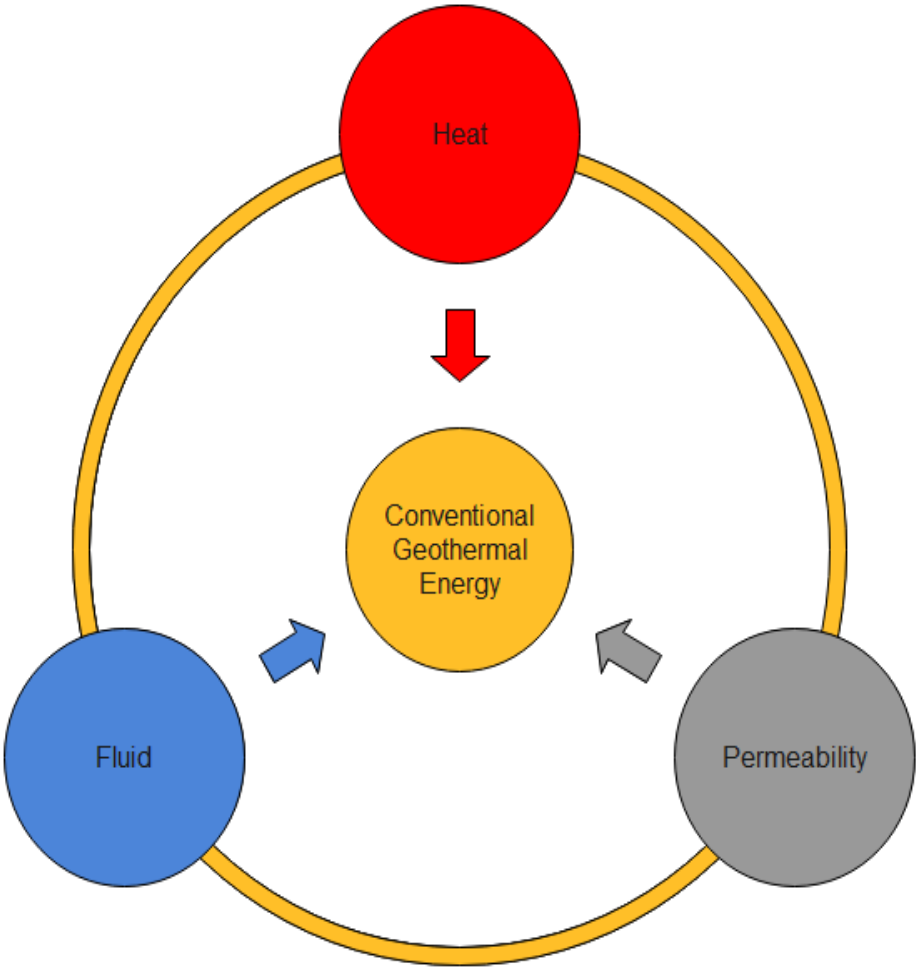


Figure 3. Required conditions for power production from conventional systems

### 1.3. Case Studies

In this section, some field studies will be examined chronologically. While examining these projects, the difficulties and problems of this method will be briefly mentioned, and the main elements of the thesis will be explained based on all these problems.

#### 1.3.1 Fenton Hill Project

The work done at Fenton Hill is considered the first of its kind and started in 1974 (Norbeck et al., 2018). Two different boreholes were drilled consecutively within this project's scope at depths of 2932 m and 3064 m. 180 °C was the maximum bottom hole temperature for these two wells, which was considered sufficient. First hydraulic fracture attempts were ineffective since the well connection was not adequate. After failing to connect the two wells, drilling another well into the fractal matrix partly shut one failed

well (Ghasemi & Alexis, 2010). After nearly a year and a half of testing, 3-5 MWt (1-1.6 Mwe) was achieved, and the continuation of the project was decided in 1979 with two new sets of well-drilled and stimulated at a depth of nearly 4400 m. However, the problem in the previous project reappeared. The expectation of the fracture propagation was not in the estimated directions. Thus, the connection of the two wells failed again, and a re-drilling operation was made to provide enough connection between the wells. During December 1983, the most effective stimulation treatment was performed in Well EE-2 (Expt. 2032, also known as the Massive Hydraulic Fracture (MHF) treatment), in which approximately 21,000 $m^3$ of water was injected over 60 hours at a maximum flow rate of 106 kg/s (Norbeck et al., 2018). Long-term tests showed that the fluid loss was minimal, temperature decrease at the reservoir rock was acceptable, and for a while, 180 °C water temperature was reached, but after some failure, this production temperature dropped back to insufficient levels. This drop was thought to be due to the low flow rate that caused heat loss while passing through cooler lithological layers.

### 1.3.2 Rosemanowes Project

Rosemanowes was a project in the Carnmenellis granite in the United Kingdom. Drilling 300-meter wells to test fracture initiation techniques began in 1977 (Macdonald et al., 1992). The direction of the minimum principal stress in the rock at Rosemanowes was vertical at 300 m; therefore, the opened fractures were primarily in the horizontal plane since fracture propagation was perpendicular to the minimum principal stress direction. At depths greater than 400-500 m, the minimum principal stress was usually horizontal, so fractures opened up preferentially in a vertical plane unless a different fault structure did not exist. Many aspects of shallow fracture behavior (i.e., mode of opening, subsequent water loss) are now recognized as distinct from those at depth. Nonetheless, the results of Phase 1 provided enough confidence in the experimental procedures at the time to justify the second phase of investigation (Macdonald et al., 1992). Thus, it was found that this shallow depth was not representative of the deeper wells. Subsequently, it was decided to drill a pair of boreholes to reach 2000 m depth. The bottom hole temperature observed at 2000 m was 80 °C. Phase 3 started in 1983, and the final borehole depth was achieved as 2600 m while the temperature was around 100 °C. After reaching these temperatures, it was decided to carry out flow tests, but at the end of four years, a decrease of 20 to 30 percent was observed in reservoir temperatures. It was also observed

that there was a short circuit in the fracturing mechanism and the reservoir was sealed to prevent this. As a result, the amount of flow in the system has decreased, and production has become more complex.

### 1.3.3 Hijiori hot-dry rock project

Hijiori's hot-dry rock project started in 1985 with the knowledge and experience gained from the Fenton-Hill HDR project. The project was developed in two parts. Because of the hydraulic characteristics of the artificial reservoir, particularly connectivity between the injection well and the production well in a domestic basement, reservoir rock had not been thoroughly investigated at the time. Consequently, a small heat extraction system known as the "upper reservoir" was planned and built first (Matsunaga et al., 2005). Drilling operations started in 1989 with four wells while three of them were producing wells and the other one was injection. The bottom hole of the production wells was approximately 1800 meters, and the other was at 2151 meters. While maximum temperature readings showed an enormous 250°C (Matsunaga et al., 2005), hydraulic fracturing operations made with 2000 $m^3$ of water and flow tests were determined for 30 days, and only 30% of the injected fluid could be recovered (Ghasemi & Alexis, 2010). Upon facing lower than expected recoveries, it was decided to move to the project's second phase and develop the system. The same wells were deepened to 2200-2300 m, and the fracturing process was repeated, targeting a larger reservoir (Figure 4).

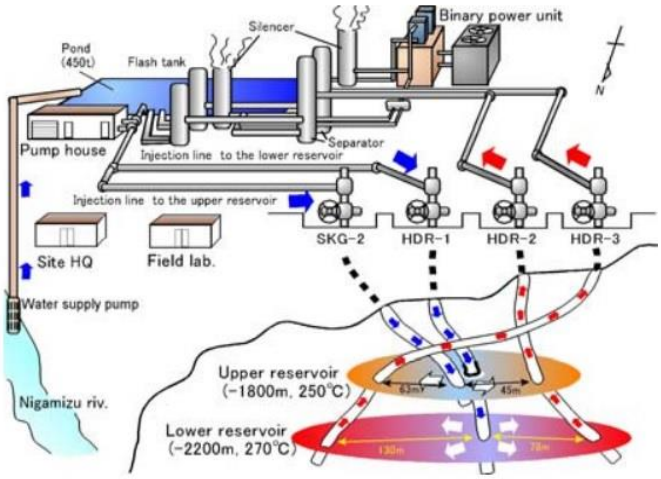


Figure 4. Hijiori Enhanced Geothermal System Project

Although the lower reservoir's production efficiency was higher than the upper reservoir, only approximately 50% of the injected fluid was returned as production (Ghasemi &

Alexis, 2010). If it is examined in terms of the produced water temperature and flow rate, the flow rate of 5 kg/s and 4 kg/ s yield 163 °C and 172 °C, respectively, while the fluid injection temperature was 36 °C. (Ghasemi & Alexis, 2010). These results showed that the total thermal energy production was around 8 MWt (2.67 MWe). Although successful operations, the project had been stalled due to an unexpected temperature decrease at the bottom hole and political issues (Ghasemi & Alexis, 2010; Matsunaga et al., 2005).

### 1.3.4 Ogachi Project

The Ogachi was also located in Japan. In the first study, two boreholes reaching a depth of 1000 meters were used where the temperature reached 230 °C (Hori et al., 1999). In this 1000-meter borehole, two different hydraulic fracturing processes were performed at the lowest point and 700th meters. This provided two layers of the fractal layer with 0.3 $km^2$ and 0.5 $km^2$ at depths of 700 and 1000 meters, respectively (Figure 5).

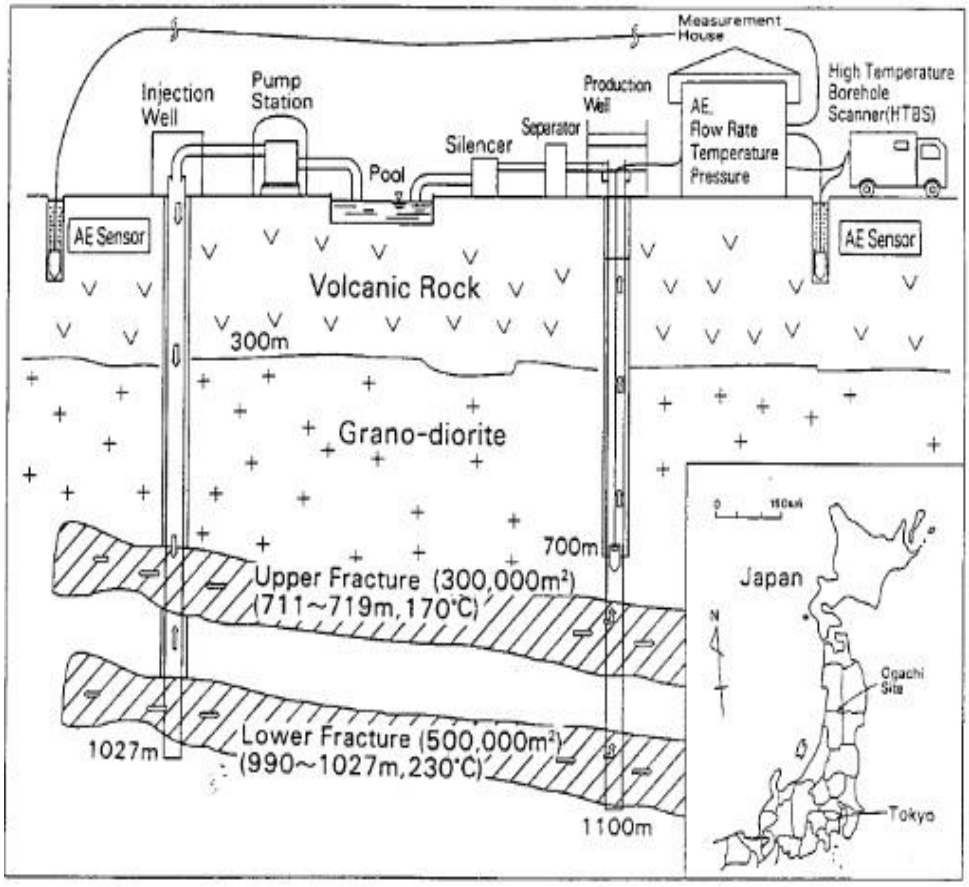


Figure 5. Ogachi Fracture Experiment (Hori et al., 1999)

First circulation tests showed just around 3% recovery of the injected water. This low production reservoir was re-stimulated in 1994. Although improvement was achieved

according to the retest results, a sufficient production level could not be reached. Production was limited to only 10%. As a result, a final cracking operation was carried out, followed by a month-long flow test. Production of the injected water amount was increased with this last stimulation; however, it reached 25% (Ghasemi & Alexis, 2010). Finally, the project was closed in 2002 (Xie et al., 2015).

### 1.3.5 Soultz Field

The European site for HDR/EGS research is at Soultz- sous-Foreˆts in northern Alsace, about 50 km north of Strasbourg, France. The Soultz project is located in the old Pechelbron oilfield in France (Ghasemi & Alexis, 2010), and it is currently the most prominent research area in this field and has continued to produce electricity effectively since 2008 (Genter et al., 2010). The site is located in granitic rocks within the Upper Rhine Graben, the most significant Central European thermal anomaly and a main active fault located 5 km east of this region (Tenzer et al., 2010). The essential factor in selecting this region was the high geothermal gradient. Gradient values were between 65 – 100 °C /km. Although the gradient changes are not constant, the change according to the layers is as follows: The gradient between 2,000–3,000 m depth is reduced to virtual zero due to convection cells and rises again to 30 °C/km at depths below 3000 m (Tenzer et al., 2010). In addition to this superior advantage, the water content in the designated reservoir was also found, whereas the older project contained hot-dry rock without any fluid content. Therefore, since the rock in the region was not dry, the name Enhanced Geothermal Systems had been used instead of HDR (Hébert et al., 2012).

In 1987, the first well re-drilled down to 2000 meters was named GPK1. In 1990, seismic surveys were performed using an old oil well (EPS1), and detailed information was obtained about the region (Gérard et al., 2006). As a result of these researches, it was decided to deepen the GPK1 well to 3600 meters where approximately 160 °C of temperature was reached (Gérard et al., 2006). Despite these, three new boreholes were drilled since the observation well, and GPK1 could not produce due to technical problems (Hébert, 2012). The depths of these three wells, GPK2, GPK3, and GPK4, were 5000 meters. The temperature at the bottom hole of the GPK2 was read as 203 °C. The horizontal distance between these three boreholes was 650 m for GPK2-GPK3 and 700

m for GPK3-GPK4, while GPK3 was well placed in the middle. (Gérard et al., 2006). Figure 6 shows the orientation of the wells.

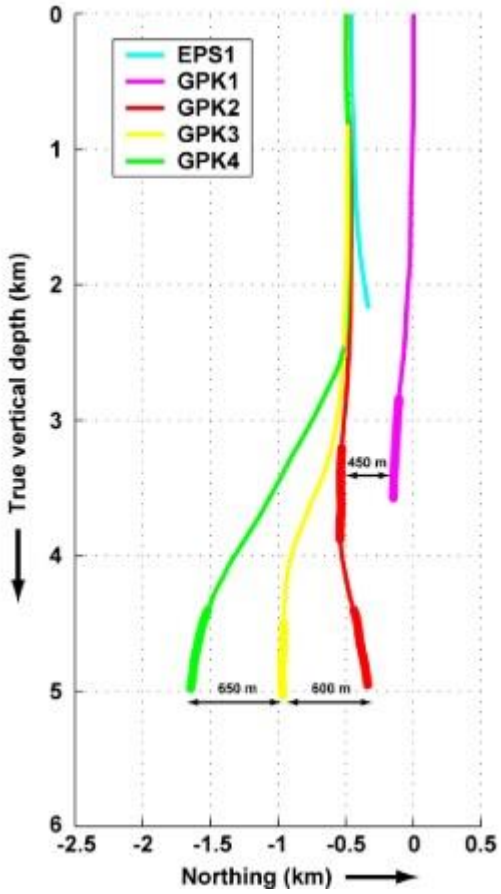


Figure 6. Soultz's well orientation (Genter et al., 2010)

Considering the problems from the previous projects, extensive borehole drilling investigations were performed to start the project. Since hydraulic fracture propagates perpendicular to minimum principal stress (Boyun et al., 2017), connecting the injection and production wells is essential after the hydraulic fracturing process. Therefore, the borehole imager and the test tools were lowered to almost all wells, except EPS1, which was cored, and borehole observations were made for the rest of the boreholes. There are two different fracture types to analyze fractal networks along bore-holes. The first fracture set induced by drilling operations can lead to misinterpretation of the stress state of the region. Thus, only natural fracture networks have been taken into account. Drilling-induced fractures are fresher than paleo-stress fractures. The differences in the directions of these drilling-induced and paleo-stress fractures provided information on the past and present stress directions (Dezayes et al., 2010). Five different measuring instruments were performed in the borehole observations. These were BHTV: BoreHole TeleViewer; UBI:

Ultrasonic Borehole Imager; FMS: Formation Micro Scanner; FMI: Fullbore Micro-Imager; ARI: Azimuthal Resistivity Imager (Dezayes et al., 2010). (Figure 7). As a result, hydraulic fracturing operation was carried out in the GPK3 boring well between 2003 and 2004, and flow tests were started between GPK3 and GPK2.

After a year, second hydraulic fracture stimulation was performed in GPK4, and circulation tests were made between the central injection well (GPK3) and two production wells (GPK2-GPK4). Test results show that connectivity between wells was sufficient for production. The circulation rate was higher than 21 kg/s, and the temperature of the injected water increased from 40 °C to 136 °C (Ghasemi & Alexis, 2010). While the amount of water produced back in the old practices was around 50%, it reached up to 90% in this region (Ghasemi & Alexis, 2010). As a result of the studies, the thermal power generation was measured as about 10 MWt. Soultz EGS site is still operating and is used as both a power generation facility and experiment field to understand the hydraulic fracture mechanism better.

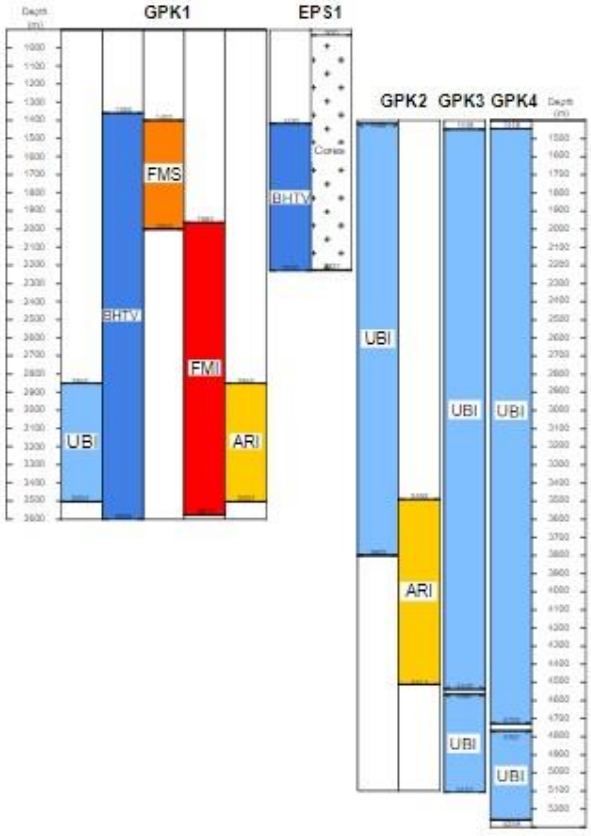


Figure 7. Soultz's boring wells and applied imager logs

In summary, this 40-50 years of hydraulic fracturing process improved geothermal energy systems. It has been proven that hydraulic fracturing can be used commercially. Despite unsuccessful attempts and high costs, the success rate has increased as information has been transferred from the past to the present. Moreover, actively used electrical facilities have emerged. (Table 1). For these reasons, this technology should be well understood and applied in Turkey.

Table 1. Completed projects and their status (Xie et al., 2015)

| Project | Country | Duration | Depth(km) | Temperature (°C) | Status |
|---|---|---|---|---|---|
| Fenton Hill | USA | 1974-1995 | 3.5 | 240 | Not-active |
| Resemanowes | UK | 1977-1991 | 2.6 | 95 | Not-active |
| Hijiori | JP | 1985-2002 | 2.3 | 270 | Not-active |
| Ogachi | JP | 1989-2002 | 1 | 230 | Not-active |
| Soultz | FR | 1987-Present | 5 | 200 | Active |

Learning outcome over the years;

- The hydraulic fracture propagating process can create lengthy fractures reaching 1-3 km.
- Acquiring a large reservoir volume is essential to the lifespan of the system. Smaller reservoirs cannot keep their heat capacity, and temperature will fade away in a much shorter time.
- In order to obtain a large reservoir volume, the gap between wells must be broad enough, but at the same time, there should be enough connection to production.
- The connection between injection and production wells is crucial for both the HDR and EGS concept

- Decreasing injection pressure will reduce the water loss and reservoir development; however, it can also cause a decrease in flow rate, which is undesirable for keeping the temperature high during the production step.
- The reservoir stress state has to be determined to estimate the direction of the propagation.
- Hydraulic fracture propagation direction is hard to estimate even with bottom-hole borehole data imager tools. A fracture can grow beyond estimations. Due to this situation, the production well has to be drilled after stimulation.
- Proppant placement needs higher pressures, and this pressure can cause short-circuiting.
- Proppant type should be chosen carefully. It must withstand high compression stresses and should not cause the particles to interlock. High thermal conductivity is essential for EGS and should be durable for years.
- Short-circuiting is almost irretrievable. Even resealing and re-stimulating will not yield any efficiency.

### 1.4 Scope of The Thesis

This thesis will be performed at the southern flank of the Büyük Menderes Graben. In order to understand the geothermal system in the field, a deep boring log having two different sections were extracted from one drilling study for research purposes, and in-hole injection, Micro-imager (Full Bore Microimager-FMI), Sonic, Caliper, Static Pressure and Temperature (Static PT) tests have been conducted. In the light of the data obtained from these experiments, it was estimated that the control of the cracks in the lithological unit was formed by the effect of geomechanical processes in the reservoir and showed behavior depending on this. In the light of previous studies, it has been proven that crack orientations have been directly affected by stress directions in the region. With these borehole data sets, it has been possible to determine the principal stresses and the orientation of the fracture system. However, it is crucial to compare the data obtained from drilling with the data obtained in field survey characterization studies and test its reliability. For this purpose, within the scope of the thesis, the results of paleo-stress distributions, scan line surveys, and focal mechanism solutions will be compared and evaluated with field studies. The principal stress and crack orientations that control the fracture-crack systems in the

region will be determined. As a result, the geomechanical behavior that characterizes the crack mechanisms occurring in the reservoir rock will be evaluated and controlled in detail at the surface and the potential reservoir depths determined in deep borehole drillings. With the help of the input parameters obtained from these, the in-situ stresses and their orientations that determine the crack mechanisms and characteristics in the potential reservoir rock will form the basis of hydraulic fracturing studies. Also, the hydraulic fracturing method will provide numerical modeling of the crack network development that will occur in the rock. As mentioned before, hydraulic fracturing is the process of creating high permeability tensile cracks at regular intervals in the borehole wall reservoir rock by the injection of a fracturing fluid containing a high percentage of water in general terms. In this way, hydrothermal waters that could not flow into the well due to low reservoir permeability before hydraulic fracturing can start to flow into the well from distant reservoir points through newly-formed high permeability cracks after fracturing. The main parameters affecting the formation, geometry, and orientation of hydraulic cracks are; drilling the well in the horizontal or vertical direction, minimum and maximum horizontal principal stress magnitudes and their directions, geometric relationship, principal vertical stress, and elastic coefficients of the rock along with the rock mass tensile strength. With the help of the obtained input parameters, crack geometries can be modeled in cracking simulations. In this way, since numerical simulation software will produce results entirely according to these values, it will be possible to create the crack in the planned geometry in natural underground conditions as much as possible. As a result, the crack mechanism in the reservoir rock will be developed (stimulation) in a controlled manner, and an artificial reservoir with optimum fluid and heat transfer properties will be developed. An artificial enhanced geothermal system will be created accordingly.

# 2. GEOLOGY AND TECTONICS

## 2.1 Geology and Tectonics

The subject of the thesis is the southern flank of the Büyük Menderes Massif, in a small scale and young-graben structure, in the western Aegean region of Turkey (Figure 8).

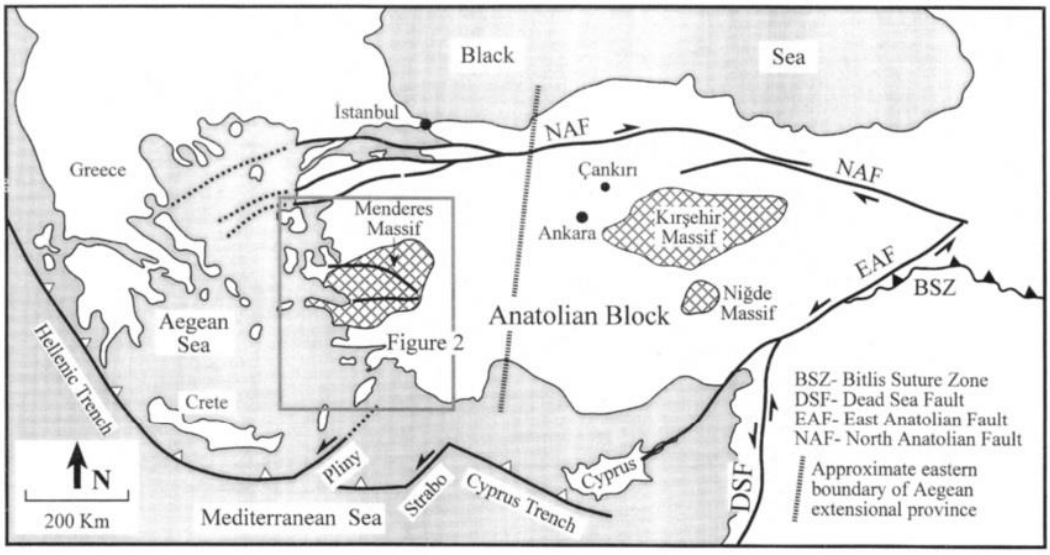


Figure 8. Menderes Massif (Barka & Reilinger, 1997)

Hydraulic fracturing mechanism requires extensive geological and tectonical surface and particularly subsurface investigations. Advanced Geothermal Systems need suitable reservoir environments that must contain both adequate temperature and the appropriate rock type for hydraulic fracturing operations. Therefore, before starting the field studies, it is necessary to investigate the paleo-stress regime, seismotectonic and geologic characteristics of the selected region from previous and literature studies and to determine the geological structure and stress regimes in the region.

To start with the geological research studies in the region, the development of Greece's and western Turkey's Aegean-west Anatolian orocline-back arc system occurred during the sinking of the African plate beneath Eurasia. This area has a well-documented structural, metamorphic, and magmatic geological record, which has been interpreted in terms of creating an accretionary prism stretched in Neogene time, permitting the exhumation of metamorphosed sections of the prism (Gautier et al., 1999; van Hinsbergen et al., 2005a; Jolivet and Brun, 2010; Ring et al., 2010). In the Neoproterozoic, the last

era of the Precambrian Supereon and the Proterozoic Eon from 1 billion to 541 million years ago, the geological development of the Menderes Massif resulted in complex geological architecture and a diverse inventory of deformation features (Siefert et al., 2021). Miocene crustal thinning caused the formation of east-west trending extensional graben structures and north-south basins (Bozkurt and Oberhänsli, 2001; Gessner et al., 2001a; Régnier et al., 2003; Reilinger et al., 2006). Menderes Massif consists of generally metamorphic crystalline units with a predominantly Alpine and some Pan–African (Şengör et al., 1984; Bozkurt and Park, 1994; Bozkurt and Oberhänsli, 2001; Gessner et al.,2001b; Ring et al., 2003). The basement rocks of the graben mainly consist of metamorphic and igneous rocks overlain by sediments and sedimentary rocks with a thickness of several hundred meters (Gürer et al., 2009). The rock type in the geothermal fields in this region is generally determined as schist and marble (Şimşek, 1985). Assuming that marble is crucial for enhanced geothermal systems since marble is known as a suitable heat exchanger, understanding the geological settlement of the area is essential for further electricity generation. Two different marble-bearing horizons are distinguishable within the area around the Büyük Menderes Graben: one of Paleozoic and another of Mesozoic (Cretaceous) age (Ring et al., 1999; Gessner et al., 2001a; Özer and Sözbilir, 2003). According to Hinsberger (2010) study, there are four nappes of different ages in the Menderes Massif. The depths of these nappes vary in the north-south direction (Figure 9). The nappes in the model forming the Menderes Massif are respectively from bottom to top; Bayındır, Bozdağ, Selimiye and Çine. Bayındır nappe mainly consists of phyllite, quartzite, marble, and greenschist, which indicates that the metamorphic grade of Bayındır Nappe is lower than other nappes. Bozdağ Nappe is mainly composed of metaperite and metagranite, including eclogite and amphibolite. According to structural data, although the age of the bedrock, Gessner et al. (1998) claim that this nappe belongs to the Precambrian age. The Çine nappe consists mainly of orthogneiss, meta-granite and pelitic gneiss accompanied by eclogite and amphibolite lenses (Siefert et al., 2021). The last nappe of the Menderes Massif formation is Selimiye, which is divided into two sections. The upper section predominantly consists of meta-pelite, meta-basite, and marble, and the lower section is composed of meta-pelite and weakly-deformed meta-granite. The age of the upper layer is estimated as carboniferous due to its fossil content, and the age of the lower section has been found as Precambrian (549 Ma) according to Uranium-Pb zircon ages (Siefert et al., 2021).

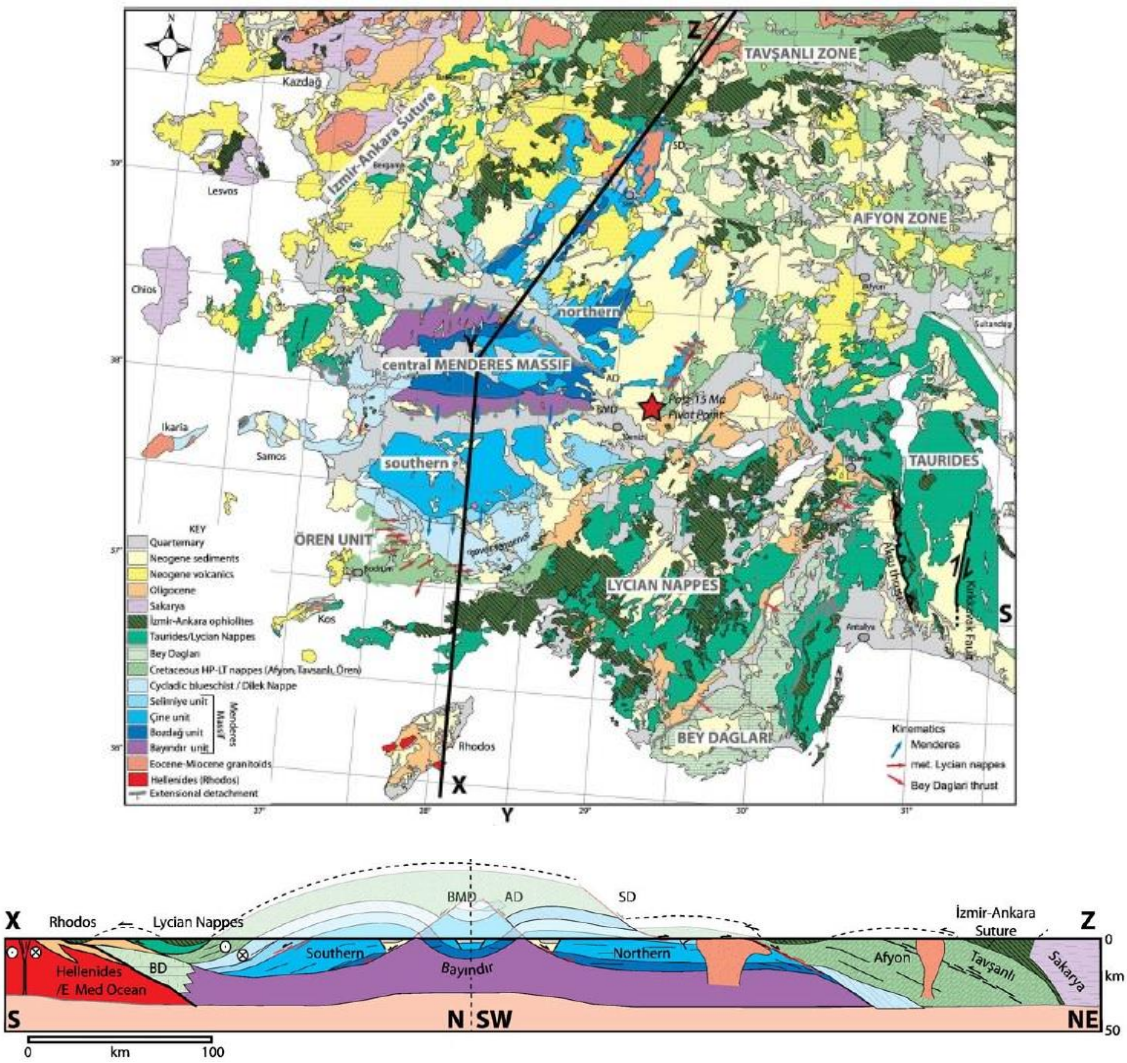


Figure 9. The layers of nappes and their strikes in the Menderes Massif region (van Hinsbergen et al., 2010)

The nappe geometry under the young cover in the Büyük Menderes Graben is stacked from bottom to top as Bayındır, Bozdağ, Çine, and Selimiye. The Selimiye, Çine, and Bozdağ nappes were lowered in the south during the graben formation. The marble located in the deeper Bayındır nappe is separated from the others by inclining towards the south and is represented by deeper marble successions (Siefert et al., 2021). These successions, suitable for developed geothermal systems in the study area and for which field studies were carried out, crop out in the Bayındır nappe.

The Aegean Region is very active based on tectonic movements to examine the Menderes Massif tectonically. In Western Anatolia, compression is dominant at first, and then a stretching occurs in the earth's crust with Cenozoic tectonics (Şengör, 1979). It is accepted that the Aegean region in the west of Anatolia also emerged as a result of crustal

expansions (Çemen et al., 2006). Different models have been put forward about how the expansion occurs in this region. These are; Tectonic Escape Model brought up by Dewey and Şengör, Back-arc Opening Model supported by Le Pichon and Angelier, and a two-stage Grabenization model put forward by Koçyiğit (1999). The common point of these different models is that the western Aegean region has expanding and seismically active tectonism (Dewey and Şengör., 1979). In neotectonics, the forces formed as a result of these expansions have caused shape changes in the western Aegean, and as a result, they have led to some east-west trending normal faults. All of these fault activities have formed the Büyük Menderes graben.

E-W trending grabens within the Aegean graben system such as the Büyük Menderes Graben system and their active normal faults limiting the basin are among the most distinctive neotectonic features of Western Anatolia. Fault directions in the Menderes graben are an essential indicator in determining the main stress directions. In the earlier phase, between Late Miocene and Early Pliocene, N-S extension occurred with the development of sub-slip-slip components of a conjugate NE- and NWN trending normal fault pair. This expansion in this region has created the episodic two-stage graben model proposed by Koçyiğit et al. (1999), which includes the following two stages. In this East-West and North-South direction, normal faults start from the east of Aydın and move towards Denizli. The main fault set mentioned above, which developed approximately in the E-W direction, developed to form steps in the Büyük Menderes Graben (Figure 10) Bozkurt 2001). It is stated that these faults are normal faults dipping south, and their formation ages start from the Late Miocene and continue until today (Sözbilir 2001).

As mentioned above, as a result of the information obtained from the compiled geological and tectonic studies, it is thought that the marbles in the Bayındır nappe at the bottom of the metamorphic nappes outcropping in the graben system in the south of the Menderes Massif are suitable for advanced geothermal systems. In this thesis, evaluations regarding the suitability of these units, especially in the study area, will be examined in detail. These E-W and N-S strike normal faults cause extensional regimes. Besides, it has been observed that these fault types and their orientations are normal faults with nearly vertical angles, which is an essential factor for the hydraulic fracture direction.

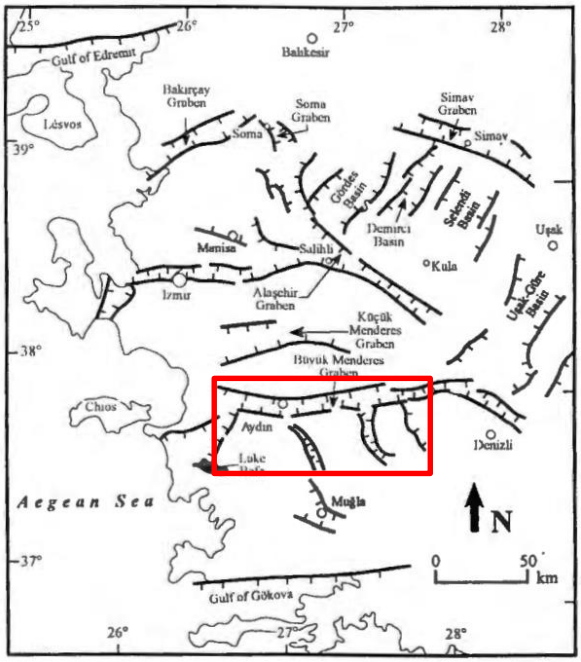


Figure 10: Simplified map showing major structural elements of Western Anatolia (Bozkurt, 2001). Heavy lines with hachures show normal fault: hachures indicate a down-thrown side.

Western Anatolia can be evaluated in the extensional area type class (Figure 11). Tectonically, this area shows an area type similar to the enhanced geothermal field of Soultz in France. Therefore, the studies conducted in Soultz are promising for the progress of the advanced geothermal studies to be carried out in the Aegean Region of Turkey.

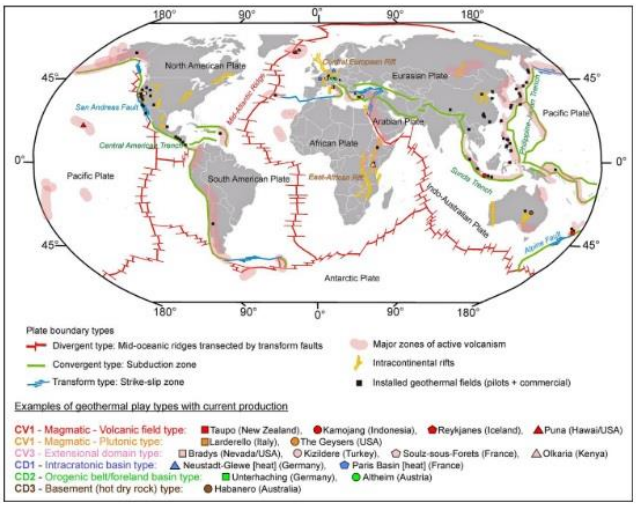


Figure 11: Geothermal systems according to tectonic classifications

Despite all these literature studies, the Aegean region's complex structure and variable characteristics require engineering geological and tectonic field studies, seismological studies, deep boring operations, and extensive geomechanical laboratory experiments to determine the seismotectonic mechanism in the targeted region in detail. Therefore, multi-disciplinary field reconnaissance surveys have been performed via assessment of fault kinematic measurements, scan-line surveys, rock mass characterization, along with geomechanical properties.

## 2.2 Paleo Stress Analysis

Paleostress is a word used in geology to describe mechanical stress that has impacted rock formations, particularly in structural geology and tectonics in the past. The situation has first developed the theory by Wallace (1953) and Bott (1959) regarding the mathematics of this method. Kinematic analysis methods using fault-slip data are divided into two groups. These are numerical analysis and graphical analysis. The basis of both methods is that the slip direction (fault scratches) and the stress systems causing the faulting are the same as the direction at which they are maximum on the fault plane. It is based on the principle that fault surfaces striations represent the maximum stress on the planes of weakness.

Carey & Brunier (1974) developed a method for determining the principal stress directions that cause faulting, based on fault scratches, using the paleo stress inversion method. Many paleo stress transformation methods have been developed in the following periods to consider different boundary conditions and variables (Angelier, 1990; Yin ve Ranalli, 1993). The basic logic of these improved methods is to use at least four or more fault-slip data from the same fault zone, which are thought to belong to the same deformation phase.

Paleo-stress inversion techniques, developed by Angelier (1988) that generally form the main mathematical framework of many paleo stress inversion software use reduced tensor logic. As a part of this research, Akgün (2021) has used the rotational optimization (RO) method, which is presented under the Win-Tensor program developed by Delvaux and Sperner (2003). There are nine variables, three of which result from fault geometry, three

from the direction of principal stresses, and three from the magnitude of stresses. Since the direction of the faults can be measured in the field, the number of variables can be reduced to six. It is possible to establish a geometric relationship between stress magnitudes according to the type of deformation. Then, it can be done by subtracting the minor stress magnitude ($\sigma_3$) from the other two stress magnitudes ($\sigma_1$ and $\sigma_2$) and revealing the magnitude relationship between the stresses using the geometry of the stress ellipsoid. This ratio is called the shape factor and is defined by the equation presented below:

$$R = (\frac{\sigma_2 - \sigma_3}{\sigma_1 - \sigma_3}) \quad (2.1)$$

### 2.3 Kinematic Data Collection from Fault Set

Paleo stress measurements are performed by measuring the inclination of the strike, dip, and fault-slip lines with the strike from the fault mirror. At the same time, the direction of movement of the fault should be determined by evaluating the kinematic on the fault mirror. In general, fault-slip data were collected from Quaternary units describing the current basin fill, the Plio-Miocene units describing the older basin fill, and schist-marble alternating unit forming the Menderes Massif. In some of the mesoscopic faults observed in the Quaternary and Plio-Miocene (Figure 12) aged sedimentary units, the fault plane and slip surface striations developed on it were observed. In addition, paleo-stress data were also collected from the schist-marble intercalated unit forming the Menderes Massif. While the directional relationship between the fault plane and the schistosity plane was taken into account during the collection of these data, attention was also paid to the existence of reference structures (different metamorphic units or vein formation, etc.) where the offsets can be tested in terms of reliability of the data.

Representative stress-tensors of paleo stress inversion solutions prepared by the Win-Tensor program are given in Figures 13. According to the results obtained based on these studies, it was observed that the maximum principal stress was in the vertical direction, and the dip angle was close to 90°. In addition, extensions observed in East-West and North-South directions prove the episodic two-stage graben model proposed by Koçyiğit et al. (1999).

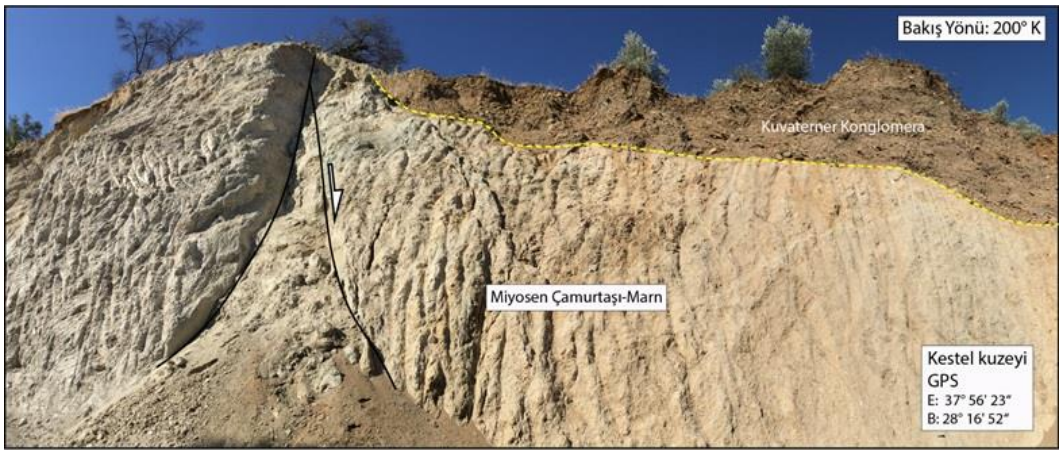


Figure 12. Measurement of the fault dip and azimuth directions at the Quaternary and Plio-Miocene Formation

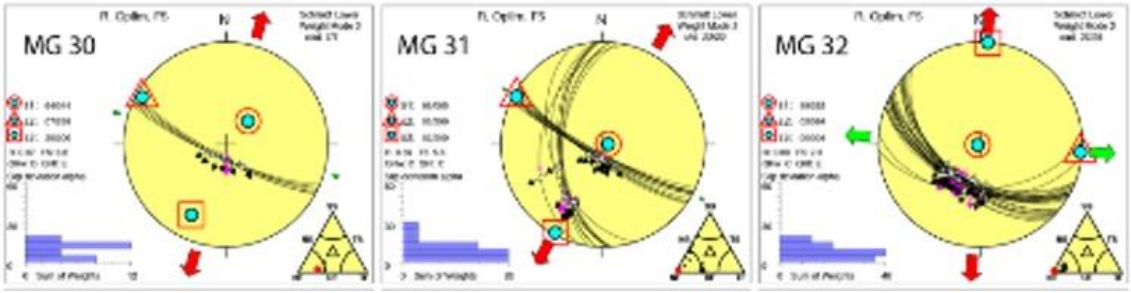


Figure 13. Paleo-Stress Directions

# 3. IN-SITU FIELD TESTING STUDIES

## 3.1 Deep Boring Studies

Identifying the in-situ stress parameters and the hydro-mechanical processes required in hydraulic fracturing applications to enhance the reservoir fracture network, deep boring studies have been performed in the southern flank of the Büyük Menderes Graben. In order to evaluate the in-situ mechanisms of the target reservoir throughout the depth, it is necessary to determine the direction and the relative magnitude of the current principal stresses along with performing fracture network characterization and determining the reservoir rock geomechanical properties in detail. Hence, deep boring studies are essential processes for enhanced geothermal systems. Deep in-situ boring data can ensure that the minimum criteria are required to meet EGS in the target region. In light of these data sets, the continuation of the operation would be decided upon, and various analyses and tests need to be performed to design hydraulic fracture procedures. In this research, geophysical in-situ testing of PT (Pressure-Temperature), FMI (Full-bore formation micro imager), Sonic and Caliper boring logs were assessed to determine thermal, in-situ stress conditions, rock mass characteristics, and geomechanical parameters.

In addition, to demonstrate that the marble succession at the selected region of the study area in the Bayındır nappe is suitable for hydraulic fracturing (sufficient heat capacity, reservoir area with high thermal conductivity), extensive deep in-situ boring information has been collected from this region. Considering the complex mechanism of hydraulic fracturing, the multitude of variables depends on the success rate in connecting the two crack mechanisms and considering the drilling depths for the deep hydraulic fracturing and drilling data that are most significant in aiding the position for modeling parameters. Raw FMI drilling data from an anonymous private organization was obtained and analyzed to satisfy and test these conditions. Before starting further engineering analysis, these eligibility criteria were analyzed and examined in regards to whether the mentioned standards could be met or not. Analyzed parameters were heating vs. depth and rock mass characteristics.

Temperature measurements were made with a multi-tool open well device starting with heat development. According to the temperature log for the shallow depths (0-2000 m), the average temperature increase was around 3 Celsius per 100 m. Although it may not seem sufficient at first glance (only a 90-degree rise can be achieved within 3000 meters), it has been observed that the geothermal gradient increases significantly at larger depths. The increase of the geothermal gradient is 5°C/100m up to 3000 m depth and approaches almost 6°C/100m for the 3900m depth, and it reaches 190°C in total from 29°C. This fact proved that the candidate geothermal site was promising from a thermal point of view hydraulic fracturing.

After checking the temperature status and deciding that this site was suitable for thermal conditions, other criteria to check were rock mass characteristics full bore imager that provides both lithology images and gamma-ray. The gamma-ray log provides a means of identifying changes in lithology in the siliciclastic environment. (Osarogiagbon et al., 2020) In reality, various rocks release varying quantities of gamma radiation, and the log allows for identifying lithological variations. Shale has high gamma radiation because clay minerals, which are common in fine-grained sedimentary rocks, contain all three of the most prevalent radioactive elements, potassium, uranium, and thorium, but quartz, the primary component of mature sandstone, contains none of these elements (Rider., 1990). In the deep boring log, a biotite schist series with a minor alteration zone representing the Bayındır formation has been encountered at the bottom of the boring between 3600 and 3650 m. A marble formation was observed between 3650 and 3725 meters, including a thin layer of biotite schist with an alteration. Between 3725 and 3900 meters, there is leucocratic orthogenesis with biotite schist and some alteration zones with gray gneiss, high chlorite, and calcite content. Although the highest temperature measurement was obtained at the deepest section of the borehole (3900 m), the rock mass type was not convenient for the enhanced geothermal systems due to the low thermal conductivity of the leucocratic orthogenesis and biotite schist.

Research shows that the heat conductivity of crystalline rocks can be around 2.5-3 to 6 W*m-1*K-1 (Durmuş & Görhan, 2009; Cáchová et al., 2016; Altay et al., 2001) while other studies have mentioned that the presence of crystalline, igneous rocks usually indicates heat exchangers (Tester et al., 2006). On the other hand, marble has substantial

high heat capacity and thermal conductivity. Rock formation and boring lithology log can be seen in Figure 14a and b.

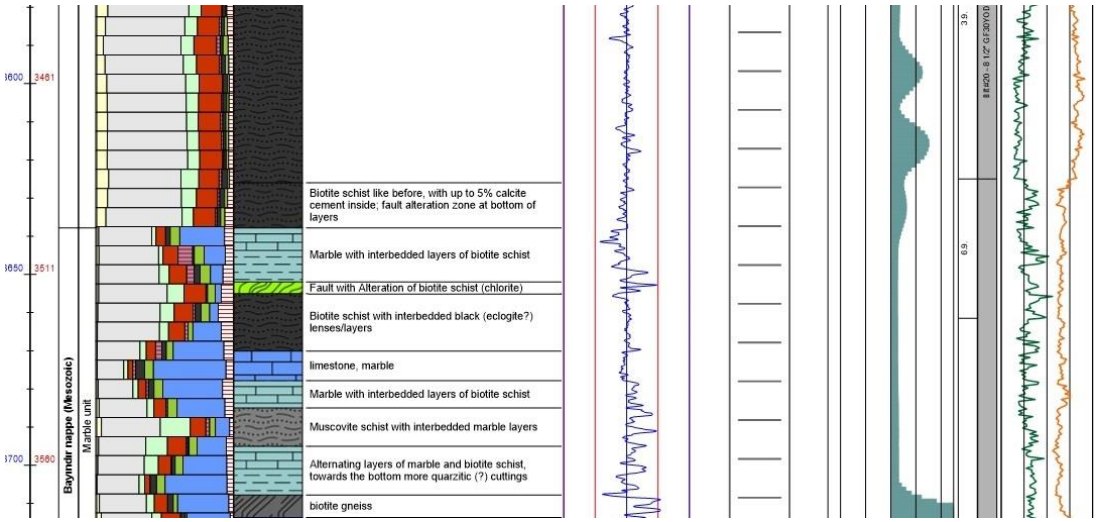


Figure 14a. First Part of the FMI boring log

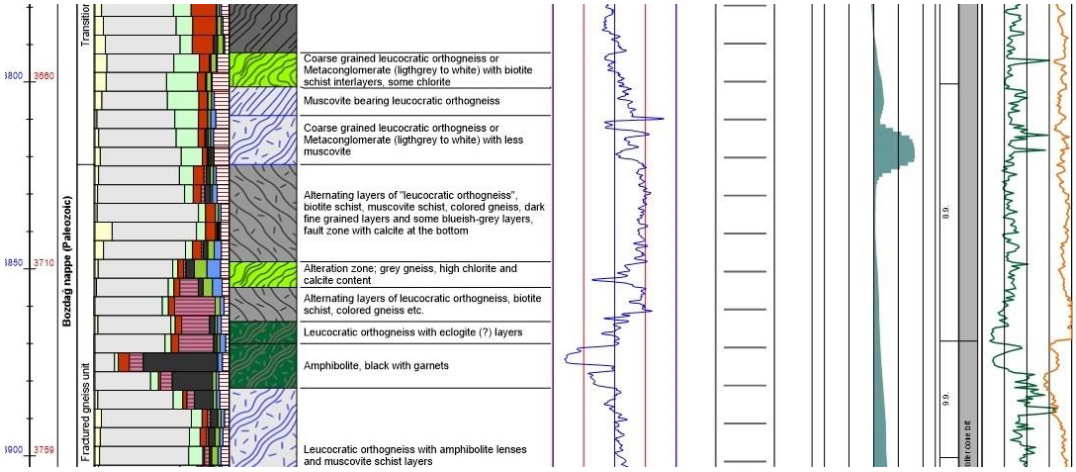


Figure 14b. Second Part of the FMI boring Log

First, the most valuable data it provides is in-situ stress conditions, which means the principal stress directions. Although principal stress directions are not the yield criteria to start hydraulic fracture, they are the essential parameters for hydraulic fracture propagation. In other words, hydraulic fractures tend to propagate along the path of least resistance and create width in a direction that requires minor force. This implies that the hydraulic fracture will propagate perpendicular to the minimum stress direction $\sigma_3$. Thus, the principal stress orientation and magnitude information are crucial for a full-bore

imager (Moska et al., 2021). Figure 15 shows the fracture propagation according to stress conditions. In other words, it will propagate parallel to maximum stress (Brudy & Zoback, 1999). Analyzing the geometry of fractures will increase the success rate and efficiency of the fractal matrix. Thus, as mentioned before, drilling data is more important than surface observations due to the complex tectonic structure of the Aegean region, and the drilling tool can provide this information by using FMI (Full-bore formation micro imager). Drilling logs that can provide a high-resolution map of the resistivity of the borehole wall help identify the exact direction, depth, type, and density of the natural cracks. (Khoshbakht et al., 2009; Rajabi et al., 2010).

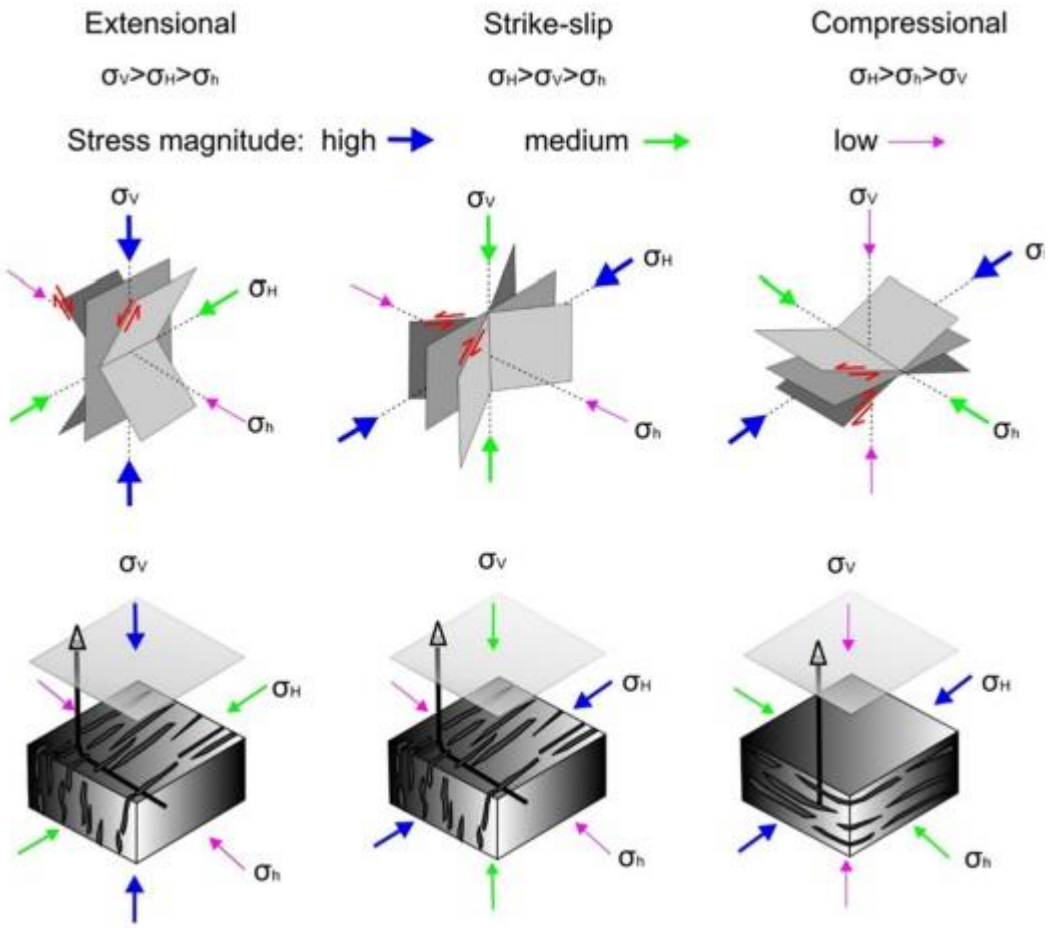


Figure 15. Fracture propagation directions according to the stress conditions (Zimmermann et al., 2010)

According to the FMI log, the North-South oriented cracks are dominant in between 2000 and 2100 meters. These cracks are also observed through the detachment fault at 2630 m. However, the target zone's crack formation is different from the upper layers of the

drilling hole. The dominant crack direction between 3600 and 3900 meters is West-East oriented with some N-S cracks (Figure 16). It implies that the two stress conditions are pretty close regarding the magnitude of stress. Since crack angles cannot be obtained with these data sets, it is difficult to determine which stress components they belong to. These data have been assessed with the other research studies (i.e., scan line surveys, paleo stress analyses) carried out in the field to correlate those results.

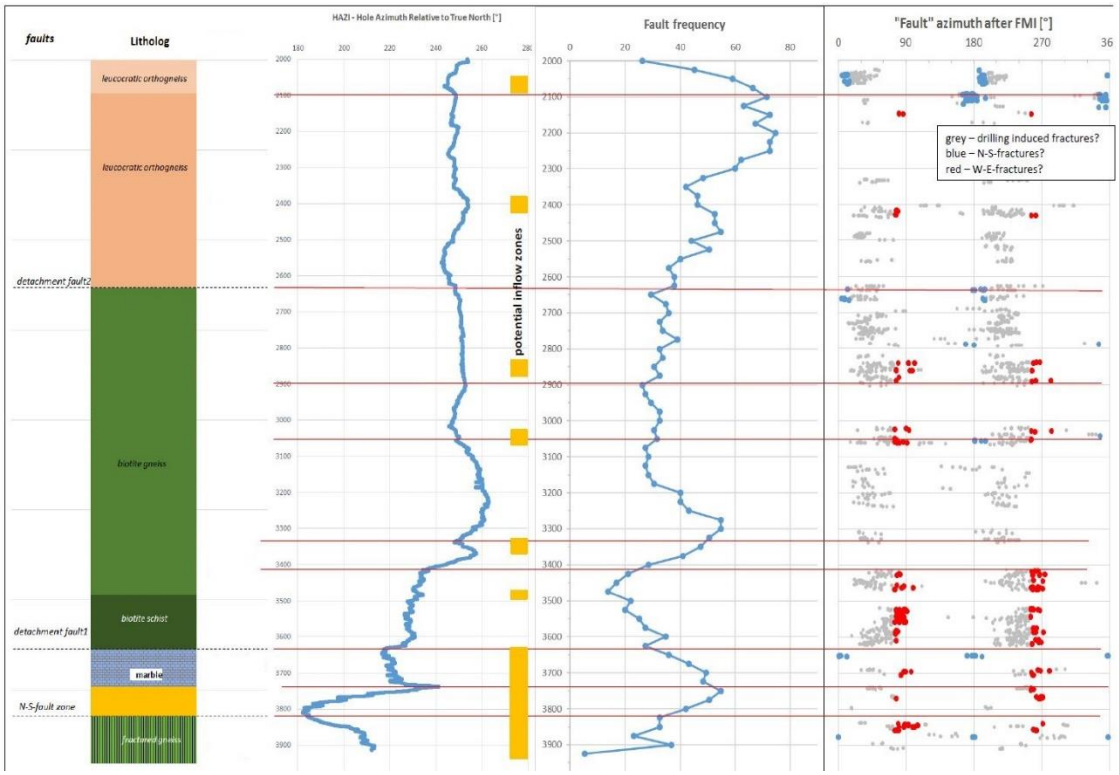


Figure 16. The FMI results are based on fault and crack orientation output throughout the depth

FMI log also gives sonic data besides stress and crack directions with its multi-tool. The estimations are derived from log measurements of the compressional or P wave travel time, calculated by running sonic geophysical logs in boreholes (Oyler et al., 2010). The difference in arrival times of the sonic waves obtained by other detectors is then used to calculate the travel time of the initial arrival of the compressional (or P) wave, which is the fastest component of the sound (Oyler et al., 2010). From the perspective of the literature, S wave calculations can be obtained from these results (Maleki et al., 2014).

Another borehole measurement was the caliper log that gives information about the borehole diameter concerning the drilling depth. With this information, the volumetric capacity of the borehole can be calculated that has to be cased (Parsons, 1943). Although

the caliper provides this data, its most important contribution is the diameter changes regarding the depth. Of course, it does not make sense in one-way measurements, but multi-arm caliper drillings provide apparent information about the shape of the boring well. In this research, a caliper log having 6-arm was used, and three different borehole diameters were obtained. The drill width (i.e., bit size) of the caliper log was 8.5 inches (21.59 cm). To analyze these three diameters, two have a significant change in diameter, and the other is nearly the same as 21.59 cm when the washout expansions are ignored.

Nevertheless, between these two caliper diameters, not much difference was observed. This situation can be interpreted as follows; there is not too much difference in magnitude between the two stresses in the horizontal plane. Bit size and Caliper measurement results can be seen in Figure 17.

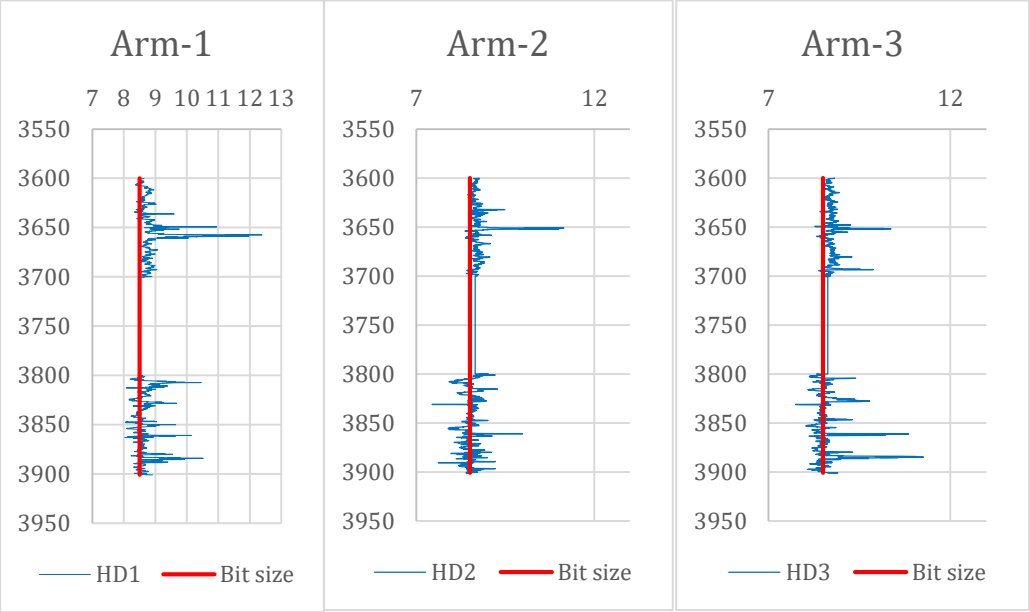


Figure 17. The results of the Caliper Log with depth

As shown in Figure 17, deep boring data provides valuable information for the lithological and engineering geological parameters of the site. It aims to complete the missing parameters and better understand the field conditions with the data obtained in-situ, along with the experiments performed on the collected samples.

Considering the depth at which the deep boring operation is performed increases the importance of drilling studies since it is not easy to obtain quantitative measurement results at these reservoir depths. Hence, these in-situ testing results from the different testing methods shall are expected to form a basis for assessing the natural fracture

characteristics and fracture network parameters of these marble units in Bayındır formation and shall be used to allow the hydro-mechanical modeling of this reservoir unit.

### 3.2 Field Studies

An extensive literature review was conducted to assess the geology and seismotectonic characteristics of the Menderes Graben. In addition to this, deep boring studies were previously performed in the field. These studies formed the basis of the field studies within the scope of geological and geophysical studies in the region. As a result of this extensive field deep boring studies, the rock mass characteristic and in-situ stress conditions of the marbles throughout the depth of the Bayındır formation have been determined. Then, engineering geological field studies were conducted, and scan-line surveys were performed in the study area to characterize the discontinuity characteristics of the fracture network of the marble lithologies of the Bayındır formation.

Furthermore, rock mechanics laboratory experiments were performed on samples collected from the marble outcrops within the study area to identify the geomechanical parameters (i.e., fracture toughness, stiffness, and strength). The orientation and magnitudes of the principal stress have been approximately determined by comparing these data obtained from the field surface studies with the boring data obtained from the deep drilling performed in the study area. As a result, in-situ stress conditions have been evaluated in a controlled manner as a consequence of the results obtained from the surface and the reservoir depths.

The engineering geological field studies were utilized to evaluate the engineering geological units, structure and discontinuity characteristics, and their fracture network in the marble lithologies of Bayındır formation that acts as the reservoir rock in the region. Specifically, a scan-line survey was carried out to determine the rock mass characteristics (i.e., discontinuity characteristics) of the marble units.

A discontinuity is a structurally discontinuous plane of weakness that runs through the rock masses. The majority of the rock lithologies contain discontinuities a few hundred

meters below the surface that highly affect the mechanical behavior of rock masses and provide information about paleo-stress conditions. Several types of discontinuities encountered were; faults, joints, fractures, and bedding planes briefly mentioned here.

### 3.2.1 Faults

Faults are visible discontinuities where shear displacement has occurred. Failure occurs in the plane where the shear to normal stress ratio reaches the fracture zone. As a result, the local stress field determines the location of the newly created fault. The relative displacement of the rock mass on different sides of the fault plane can be used to identify them. The magnitude of this displacement is frequently used to categorize faults. The lengths of the faults can range from a few meters to kilometers. Like fault lengths, fault thicknesses can also vary from meters to several kilometers. Figure 18 shows the fault types and their principal stress orientations. A normal fault is a dip-slip fault in which the hanging wall block has moved down relative to the footwall block (Figure 18). Normal faults are produced by extensional stresses in which the maximum principal stress (rock overburden) is vertical and normal faults cause extension at surface geometry.

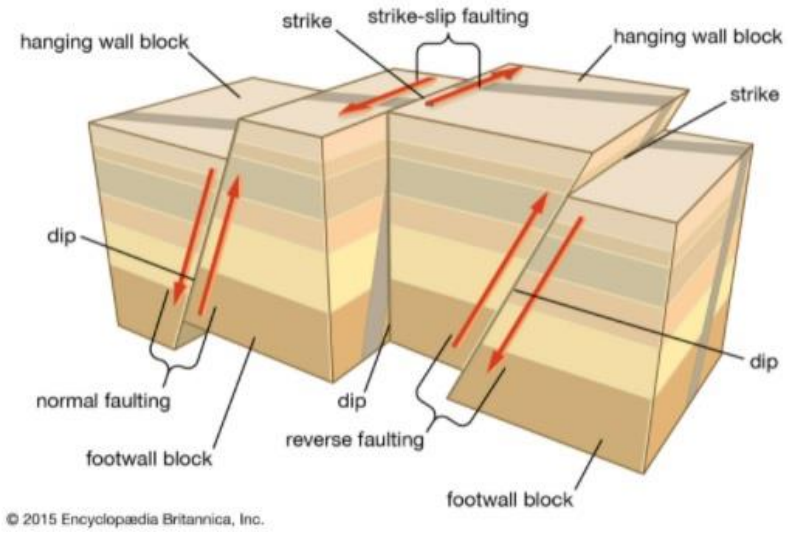


Figure 18. Fault Types (ThoughtCo, 2017)

A normal fault mechanism might occur when the lithostatic pressure exceeds rock strength. In contrast, the behavior of reverse faulting is entirely opposite. Reverse faults arise from compressive stresses where the maximum principal stress is horizontal and the minimum is vertical. Also, reverse faults cause shortening in the direction of maximum principal stress (Figure 19). Apart from these, the fault system that occurs when the

maximum and minimum principal stresses are in a horizontal position and the fault line moves horizontally is called a strike-slip fault (Figure 19).

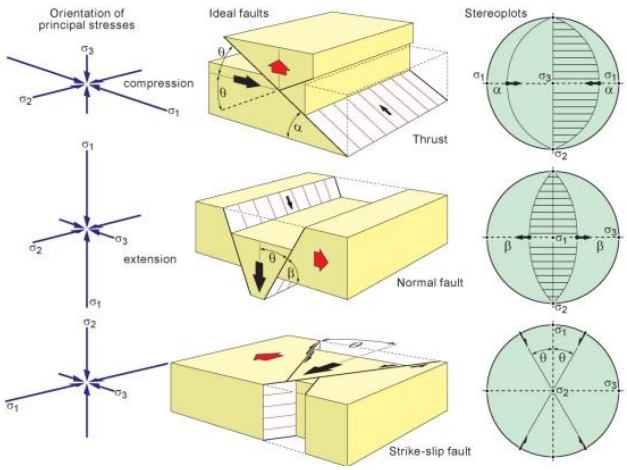


Figure 19. Fault stress orientations (Burg, J.P. 2013)

### 3.2.2 Bedding Plane

The surface separating each successive layer of a bedded rock from the previous one is named a bedding plane. They represent interruptions in the deposition process of the rock mass (Zhang, 2017). Bedding planes are usually persistent features, although sediments rapidly disturbed by wind or water may contain crossed or incongruent layers (Zhang, 2017). They are used to determine the relative order and age of the deposited sediments forming the beds. At the same time, the weathered or altered planes can indicate their origin and depositional environment. Alteration on the surface can be interpreted as the bedrock being formerly exposed to high temperature or chemical water. Also, the orientation (i.e., dip direction and dip angle) of the plane can be used to estimate the in-situ stress orientations in the field since bedding planes are directly affected by stress directions.

### 3.2.3 Joints

Joints are brittle fractures in the rock, and they are the most common and important types of discontinuities of the rock mass. Joints can form due to tectonic activities such as the compressive stresses in front of a mountain belt, folding, faulting, or internal stress release during uplift or cooling. They often form under high fluid pressure (i.e., low effective stress), perpendicular to the minor principal stress. Most joints in many tectonic

environments, particularly platforms, are vertical or steeply inclined and consist of sets of extension or hybrid fractures, suggesting that the maximum-minimum stress during a failure is usually tensile and that stress variations are typically minimal. Figure 20 shows the tensile cracks formed by folding. Many joint platforms have different orientations because of the far-field stresses induced by plate motion and basin subsidence, uplift, and inversion. Thus, even only one joint set can yield different stress directions.

Furthermore, as mentioned before, joint sets are the best evidence for a region's paleo and current stress state (i.e., Engelder & Geiser 1980, Engelder 1982a, b, Hancock & Kadhi 1978). The orientations of the principal stresses can be determined in the light of knowledge that extensional fracture is initiated perpendicular to principal stress. Therefore, joint analysis is crucial for field studies to determine principal stress conditions.

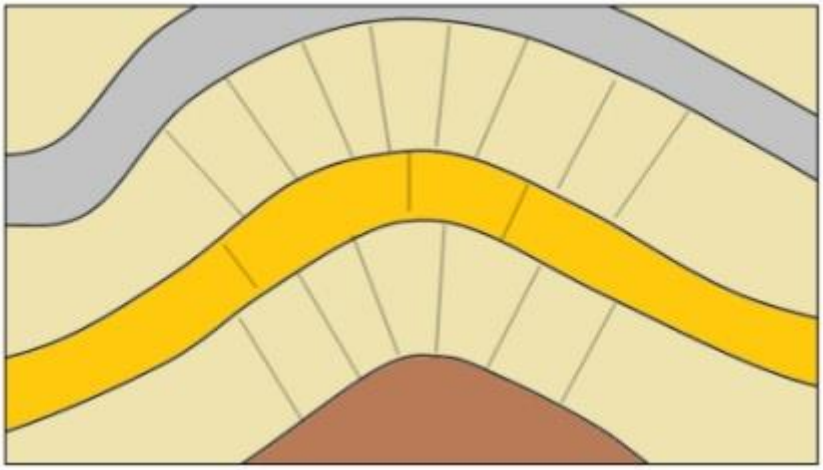

Figure 20. Folding Cracks (Earle 2015)

The discontinuity analyses were performed according to the standards recommended in ISRM (2014). According to ISRM (1978), ten parameters need to be defined to characterize a discontinuity set (Figure 21). These rock mass characterization parameters are listed and defined below;

1. Orientation: Directions of discontinuities in the rock mass. It is described by the dip direction (azimuth) and dip angle of the line of steepest declination in the discontinuity plane.
2. Spacing: Perpendicular distance between two contiguous discontinuities.

3. Persistence: This is the trace length of the discontinuities observed in the study area. The termination of the rock or discontinuity reduces the persistence.
4. Roughness: Natural surface roughness and waviness relative to the mean plane of a discontinuity. Roughness and waviness increase the shear strength.
5. Wall strength: Equivalent compressive strength of adjacent rock walls of a discontinuity.
6. Aperture: Size of a discontinuity. In other words, the distance between two adjacent rock walls of a discontinuity.
7. Infilling: Materials that fill in discontinuity walls within years are called infilling. It can be both organic and inorganic. If the filling has minerals such as quartz and calcite, discontinuities can be observed as healed.
8. Seepage: Moisture and water content of the discontinuity.
9. Sets: Number of the joint sets within the system.
10. Block Size: Size of a block that is bounded by discontinuities.

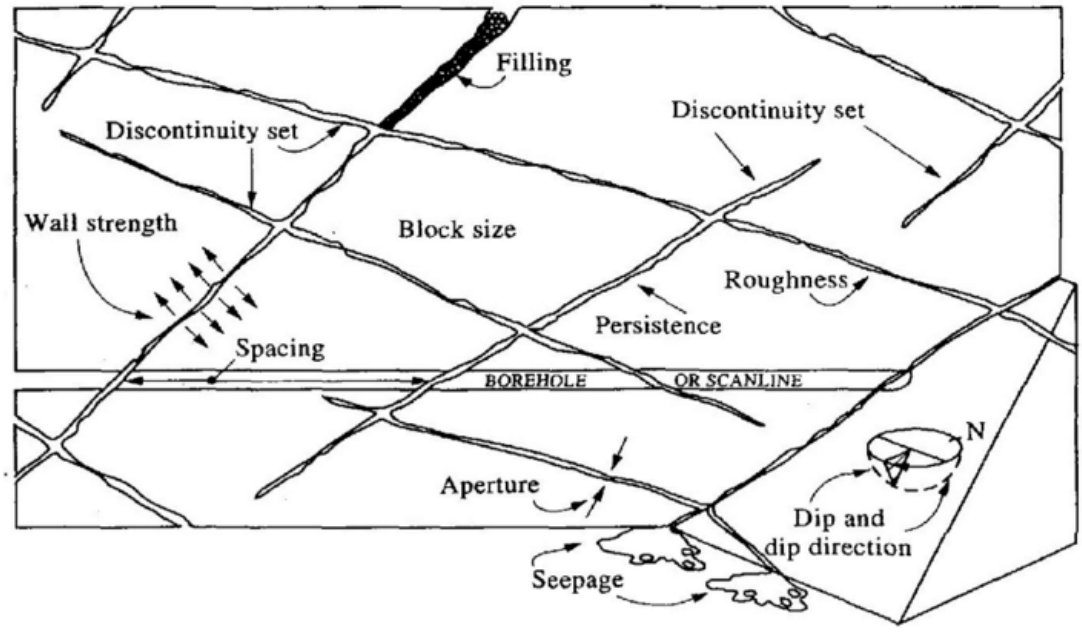


Figure 21. Discontinuity Parameters (Hudson, 1989).

In this context, a field scan-line survey was carried out to determine the discontinuity characteristics of the rock mass and the associated joint system on the marbles of the Bayındır formation. The dip directions and dip angles of the discontinuities were determined by utilizing a compass and clinometer method (ISRM, 2014) in the field.

These data were then compared with the principal stress results of other studies (i.e., deep boring data and paleo stress analyses results). Discontinuity analyses in the field are based on the characterization of discontinuities such as faults, joints, of rock masses. This process determines the number of discontinuity sets, discontinuity orientations, spacing, persistence, roughness, aperture, and infilling. In this research, the discontinuity orientations measured by the scan-line survey studies were interpreted by using stereographic projection with the Dips software (Rocscience, 2021). As a result, the number of discontinuity sets and their orientations was determined by considering the distribution and density measurements.

This information was accompanied by a scan-line survey in an area close to the deep drilling locations. The research studies were carried out in two different marble quarries in the Bayındır formation that were close to each other and located in the southern flank of the Menderes Massif.

The field studies were started with the general observation of the area to decide if the selected sites were suitable for a scan-line survey. In addition, the rock masses in the selected sites were checked and compared with the rock mass characteristics that have been identified in the deep drilling. After the region was determined as suitable, the first quarry was examined (Figure 22), and a scan-line survey was conducted. Although the bedding plane and some of the joint sets were clearly identifiable in this quarry, surfaces that were thought to be fresh were also determined. Furthermore, it was observed that small pieces of rock were broken and detached from the main rock mass in the quarry region. These observations led to a conclusion that the surface of the quarry was disturbed owing to man-made actions on it, such as excavation (Figure 22). Although these conditions caused scan-line studies to be challenging to complete, the observations on the outcrop provided information about the general characteristics of the rock mass and the discontinuities.

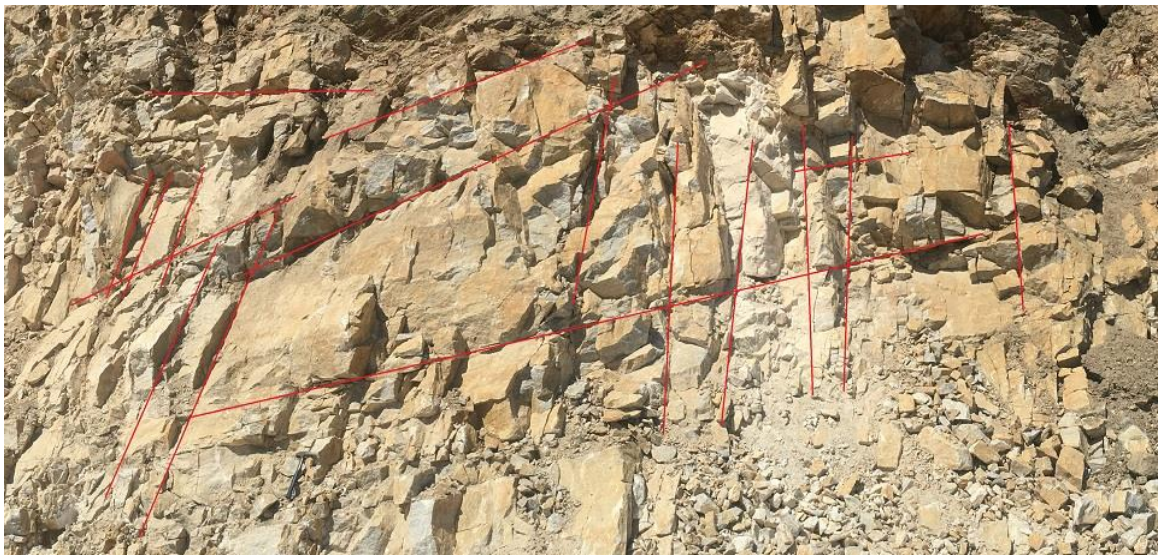

Figure 22. The general appearance of the rock mass in the first quarry

The condition of the second quarry was better than the first one. The rock mass in this location was light gray colored marbles having a bedding plane and two joint sets. The three discontinuity sets were visible (Figure 22). The outcrop surfaces were slightly weathered and altered. The discontinuity spacing varied from 40 mm to 1.5 m and was classified as wide spacing according to ISRM (2014). Discontinuities generally had medium persistence. The discontinuity apertures that were observed to vary between 1 and 30 mm were classified as moderately wide according to ISRM (2014). Sheet-like calcite infilling was observed along with the apertures. The roughness of the discontinuity surfaces was identified as undulating smooth to undulating rough.

Figure 23. Panoramic view of the marble unit of Bayındır Formation in the first quarry

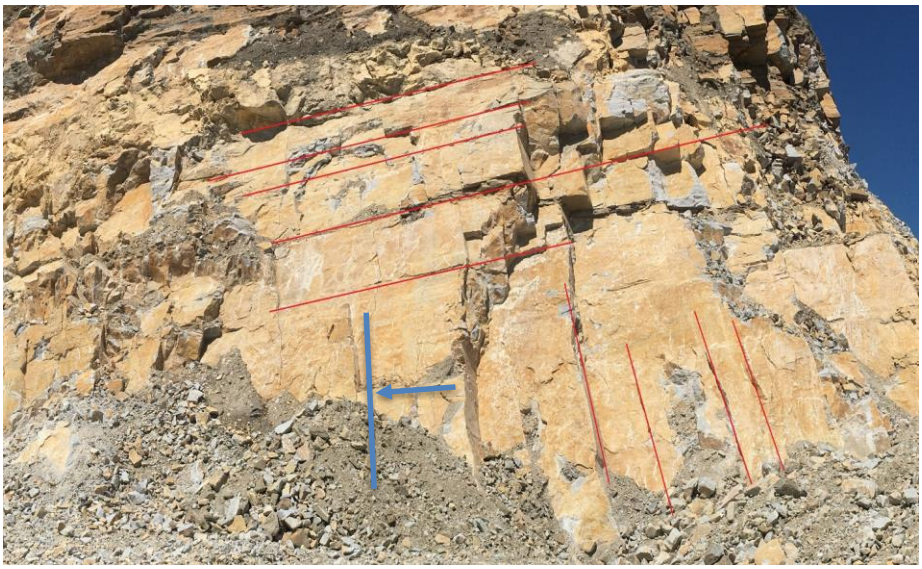

Figure 24. The general appearance of the marble unit of Bayındır formation in the second quarry

Figure 25. The photos taken during the scan-line survey studies

The distributions of the major discontinuities and the discontinuity set orientations identified as a result of the stereographic analyses of the pole plots conducted by the Dips software (Rocscience, 2021) are given in Figure 26 and Table 2. The first two pole plots represent the scan-line survey of both quarries separately, and the third one is the combined version of all these data. According to these results obtained from the pole

plots, it can be inferred that the E-W and N-S extensions may affect the discontinuity characteristics of the marble rock units cropping out on the region and show similar orientations depending on the extensional regime. These results confirm and support the previously mentioned FMI results obtained from deep boring geophysical studies.

Table 2: Summary of the discontinuity sets of the marble lithologies and the orientation of each set

| Location | Set | Orientation (Dips Software) | |
|---|---|---|---|
| | | Dip | Dip Angle |
| Quarry | BP | 79 | 355 |
| | J1 | 31 | 253 |
| | J2 | 61 | 79 |

Besides the discontinuity characteristics of the marble lithologies, the detailed results of the discontinuity characteristics where the scan-line surveys were carried out during the field studies are given in Appendix A. These processes include assessing the discontinuity features and their orientation, spacing, aperture, persistence, wall roughness and infilling material, etc., along the discontinuity planes measured in the field. Based on these survey results carried out along the outcrops of the marble units in the study area, quantitative information such as the orientation, spacing, aperture, and persistence of the cracks and topological information such as intersection (X), divergence (Y), and termination (I) of the crack nodes were combined to determine the geometrical, spatial and geomechanical characteristics. Hence, the general characteristics and density information were obtained by using the surface data of the crack network. These results have been used in the fracture network analyses for the Bayındır formation marble lithologies to evaluate the in situ stress conditions at the reservoir depths. The histograms representing the distribution and the frequency of each parameter based on ISRM (2014) are also given in Figure 27. A summary of the scan line survey and collected data is presented in Appendix A.

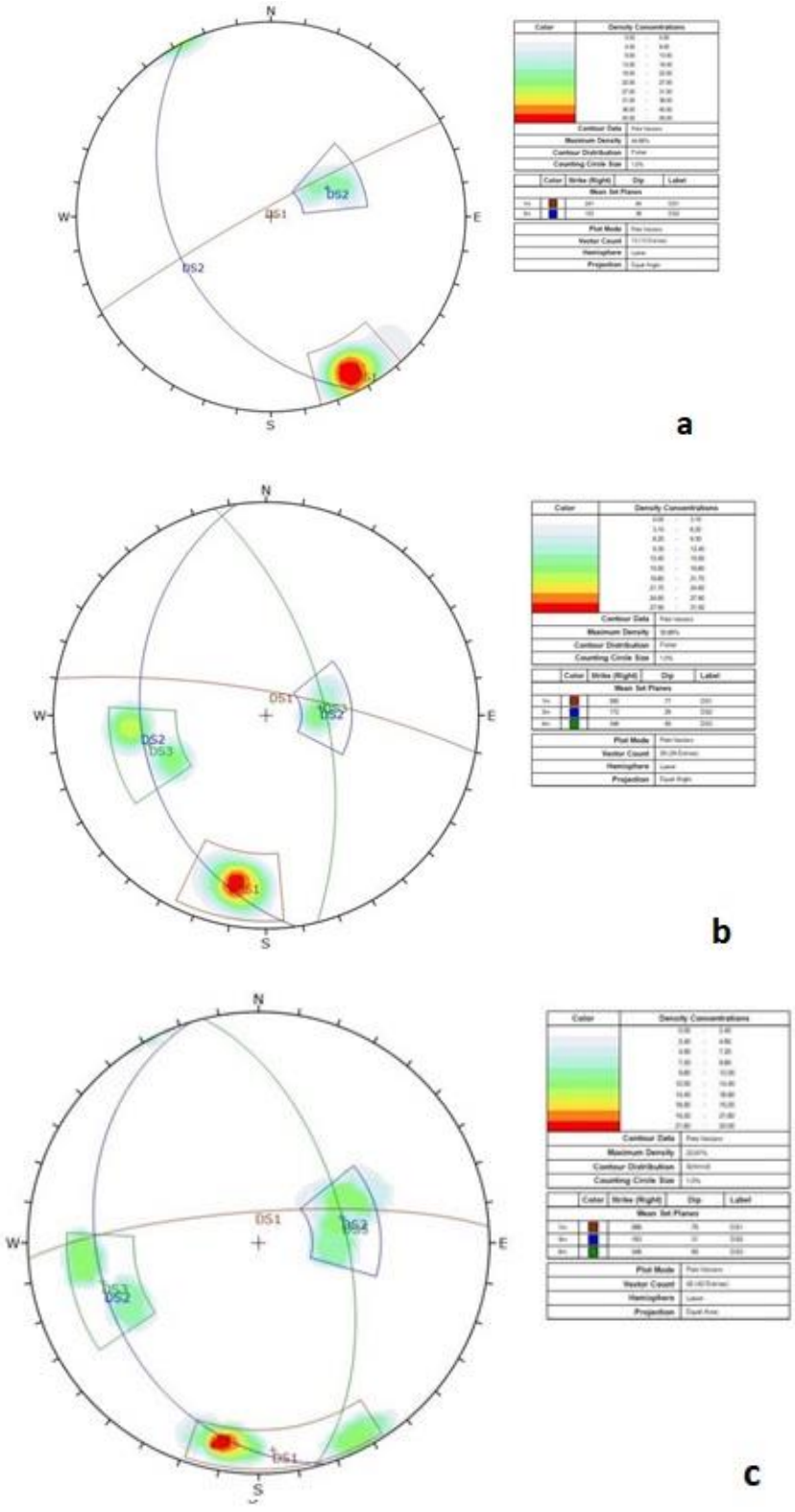


Figure 26. Stereographic pole plots display the discontinuity orientations obtained by the Dips software (Rocscience, 2021). a) First quarry discontinuity orientation, b) Second quarry discontinuity orientation, c) Combined discontinuity orientation.

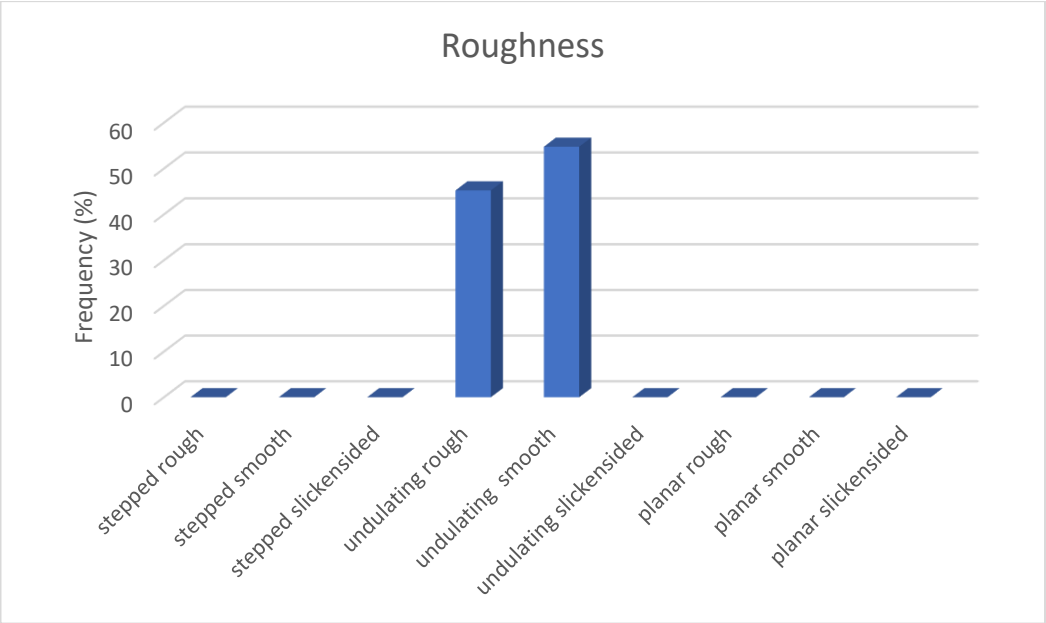
Roughness
Frequency (%)
60
50
40
30
20
10
0
stepped rough
stepped smooth
stepped slickensided
undulating rough
undulating smooth
undulating slickensided
planar rough
planar smooth
planar slickensided

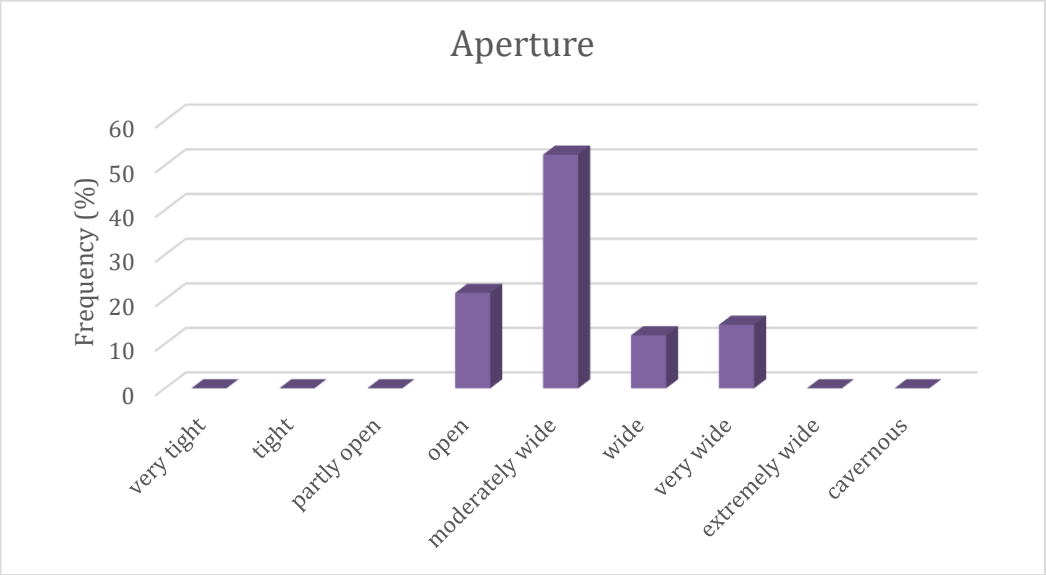
Aperture
Frequency (%)
60
50
40
30
20
10
0
very tight
tight
partly open
open
moderately wide
wide
very wide
extremely wide
cavernous

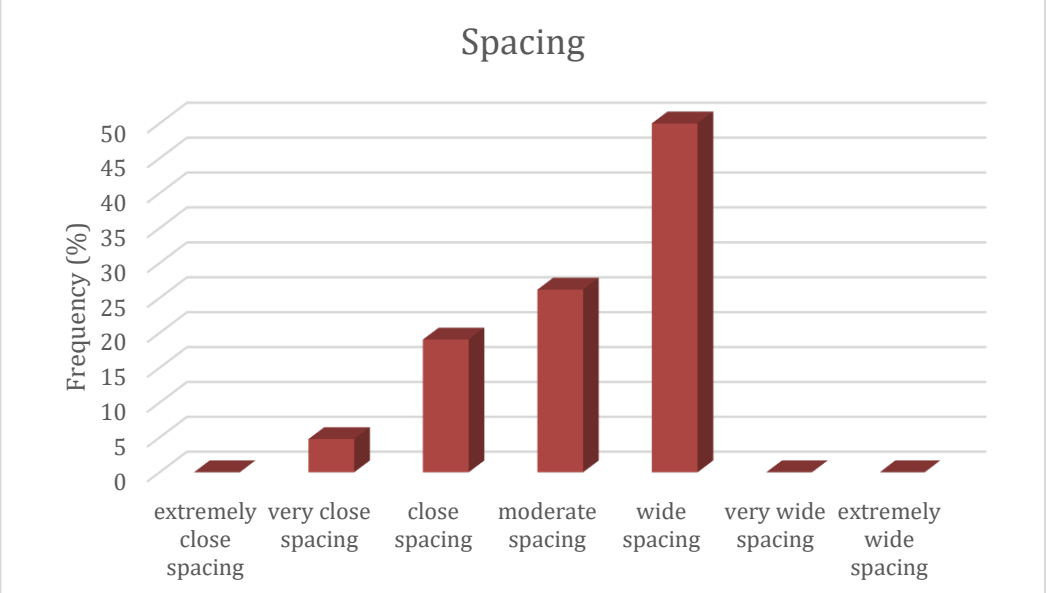
Spacing
Frequency (%)
50
45
40
35
30
25
20
15
10
5
0
extremely close spacing
very close spacing
close spacing
moderate spacing
wide spacing
very wide spacing
extremely wide spacing

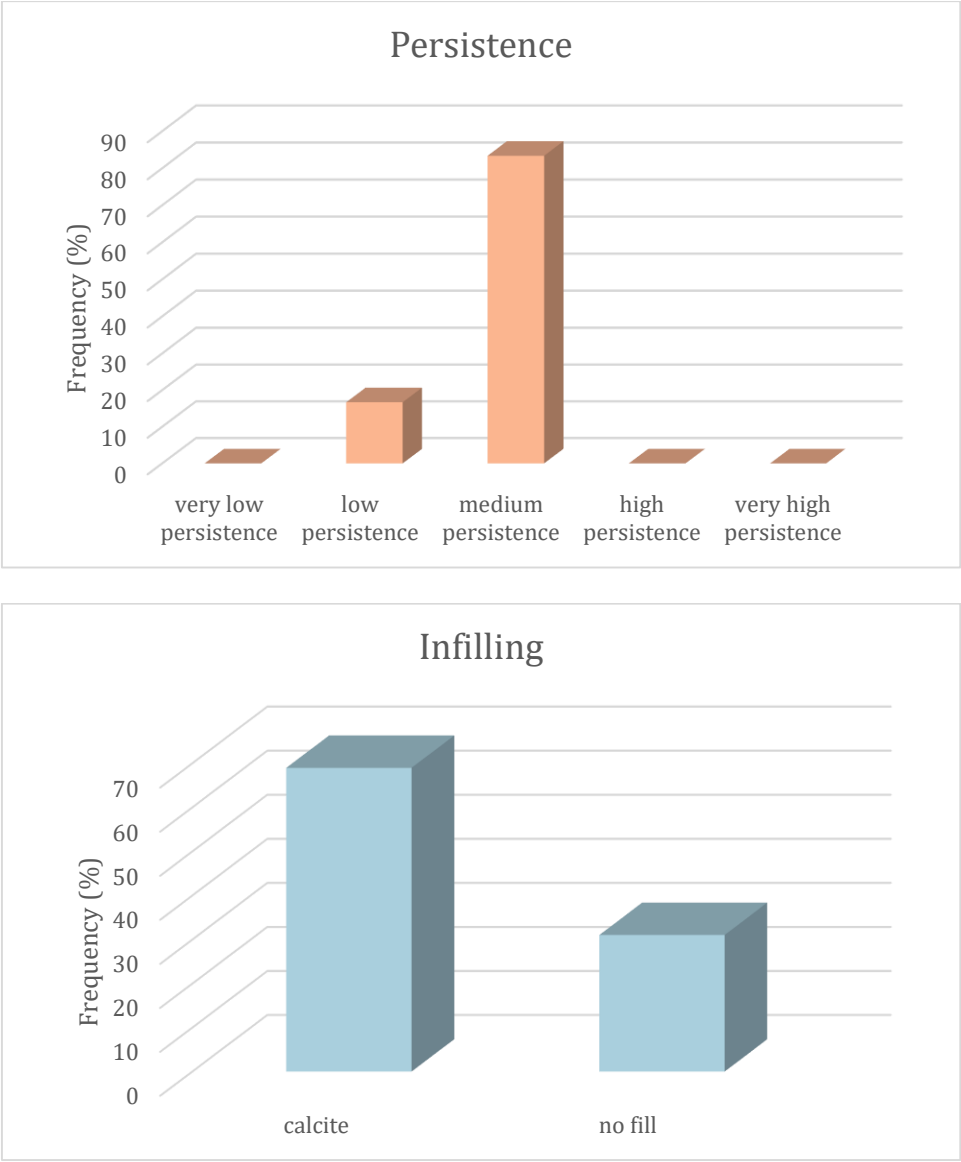


Figure 27. The histograms represent the distribution and the frequency of each different discontinuity characteristic based on the scan-line surveys performed by ISRM (2014)

# 4. LABORATORY STUDIES OF ROCK MECHANICS TESTING

## 4.1 Laboratory Studies Preparation

Apart from the scan line survey, field studies were also carried out to obtain representative block samples from locations where the marbles of Bayındır formations, considered as geothermal reservoir rocks' (Akgün, 2021). Rock mechanics testing such as uniaxial compressive strength, triaxial compression, static deformability, and point loading tests were carried out on the block samples taken from the marble units of the Bayındır Formation and the determination of the geomechanical characteristics of the rock masses have been performed. In this context, the samples obtained from the field (Figure 28) were used to perform strength and point load tests in the rock mechanics laboratory. Static deformability, Uniaxial Compressive Strength (UCS), and Triaxial Compressive Strength (TCS) laboratory tests were performed in the Rock Mechanics Laboratory according to the standards recommended by the International Society for Rock Mechanics (ISRM, 2007). While the point loading test was carried out in the ODTU Geological Engineering Department, Engineering Geology Laboratory, the other experiments were performed in the ODTU Mining Engineering Department, Rock Mechanics Laboratory.

## 4.2 Uniaxial Compressive Strength (UCS) Test

The UCS was conducted to determine the failure loading conditions beforehand, especially before the TCS tests. This test was performed to determine the strength characteristics and rock mass classification of cylindrical intact rock samples and the UCS, which is widely used in the design. For the test, samples are prepared with a length-to-diameter (L/D) ratio of 2.5 to 3.0. The dimensions of the sample subjected to the test are as follows, 119.93 mm length and 52.87 mm diameters. The UCS value decreases as the sample length/diameter ratio increases.

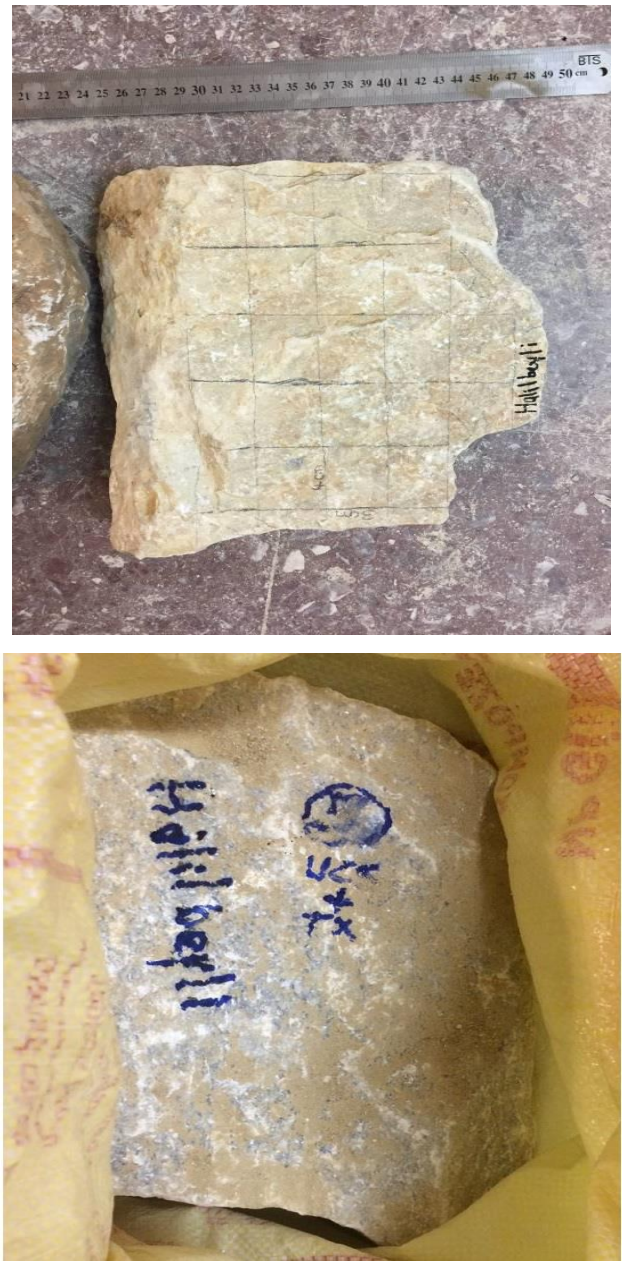

Figure 28. The block samples obtained from the field reconnaissance in Bayındır formation

Before the experiment, the cylindrical intact rock sample is placed between hydraulic press tables. In order to ensure that the load is homogeneously distributed through the sample, steel discs having the same diameter as the sample are placed at the top and bottom of the rock sample (Figure 29). The axial load that will cause the intact sample to fail between 5 and 10 minutes loading rate is applied to the sample. This test is called the uniaxial compression test since the sample is only applied from one axis, and the sample is compressed in this axis direction throughout the test. A rapid or gradual decrease in load is observed when the sample fails since the specimen cannot carry more load than

its maximum capacity. The value at which the load decrease starts gives the maximum strength load of the sample. The uniaxial compressive strength value is obtained by dividing this maximum load (F) by the sample area (A). According to the UCS test result obtained from the core sample of marble units, the compression strength of the intact sample was estimated as 89.88 MPa. The core sample photos after the test are given in Figure 31. By the aid of the UCS results, both the uniaxial compressive strength of the rock mass was determined, and the estimated lateral pressures (Hoek's cell pressure) to be applied in the TCS tests were predetermined. Then, TCS testing was carried out by taking these lateral pressure values into account.

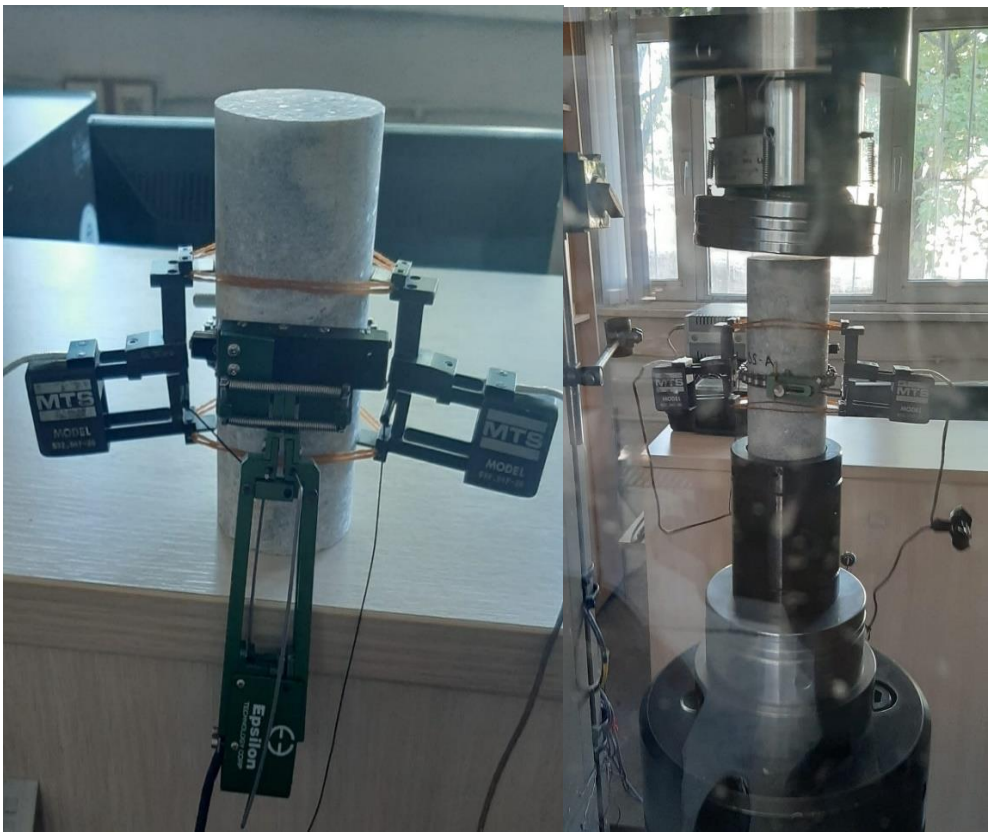


Figure 29. The view of the intact core sample during the UCS test performed

### 4.3 Triaxial Compression Test

After the UCS test, the marble samples with block sizes taken from the project area were drilled using appropriate cylindrical core dimensions for the TCS tests. Three core samples (Figure 30) were used for the TCS test. As a result of the testing carried out,

shear strength parameters of the intact rock samples were obtained depending on the triaxial compressive strength of the marble units.

The TCS test applies a loading along the vertical axis while applying a constant cell pressure to the cylindrical specimen. The sample is placed in a membrane before the experiment and placed in Hoek's cell. In order to obtain cell pressure ($\sigma_3$), oil is pumped into the cell so that no air remains inside the cell. In this way, the lateral pressure chamber is prepared for the testing. In this test, cylindrical specimens with an aspect ratio of 2.0-3.0 are used. Also, a Hoek's cell and a latex membrane suitable for the specimen diameter are used. The test sample is placed in Hoek's cell with equal space between the top and bottom parts. The cylindrical metal piece on which the screw is placed on the cell floor keeps the sample placed inside the cell. The place of the test sample in the cell is fixed by tightening the screws. This part also ensures that the cell is kept at a certain height during the experiment.


Figure 30. The view of the TCS test core samples having marble lithology

The spherical heads of the frame are placed on top of the sample, and the axial load cell is placed on it from above. Lateral and axial loading is applied to the sample simultaneously at the same loading rate until a determined fixed lateral pressure value is reached. When the desired lateral pressure value is reached ($\sigma_3$), it stops, and axial loading

continues until the sample fails. The axial loading rate is chosen such that the sample will fail in 5–15 minutes. In this way, an equal load from both sides and increasing from above is applied to the test specimen. As in the UCS test, the axial load value gives the maximum capacity for this determined chamber pressure at the moment of failure. The axial stress of $\sigma_1$ is obtained by dividing this value by the sample area.


Figure 31. The view of the TCS test core samples after the testing

Shear failure along the material occurs that develops inclined to the direction of the maximum principal stress ($\sigma_1$) applied to the sample. Shear failure occurs when the shear stress exceeds the material's shear strength. Mohr circles are used to find the stresses that initiate shear failure. The vertical axis shows the shear stresses, while the horizontal axis shows the principal stresses. The difference between the principal stresses is the diameter of the Mohr circle. The normal stress and shear stress values that caused failure are determined by using the angle of inclination of the failure plane on the Mohr circle (Figure 32).

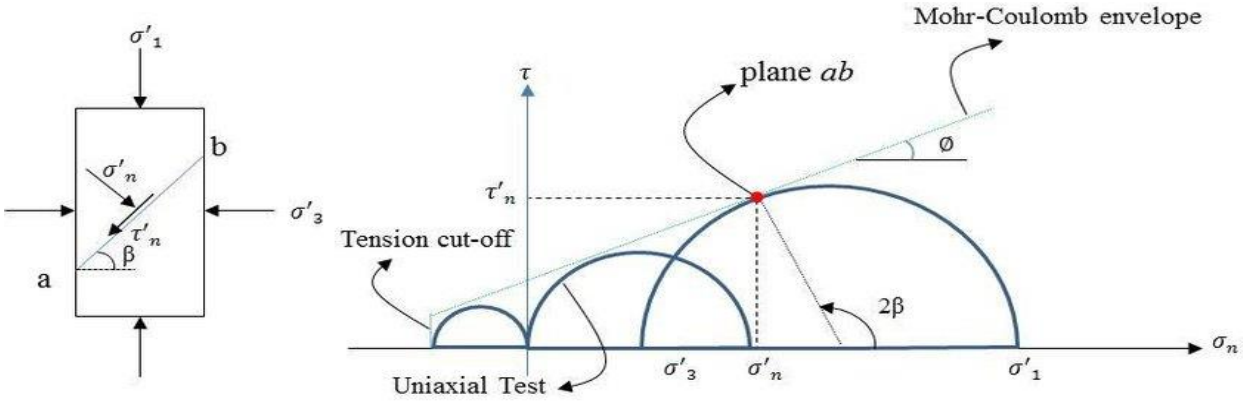


Figure 32. Mohr-Coulomb failure criterion

Multiple tests (with at least three samples) must be performed to find the failure envelope under different cell pressures. As a result of these calculations, the findings of the three samples tested for triaxial compression are given in Table 3. According to the tests performed, Mohr's circles are given in the figure below (Figure 33). The tangent angle drawn to these circles with the horizontal axis gives the internal friction angle, while the point where it cuts the vertical axis gives the cohesion value.

Table 3. The TCS test results of the marble specimens

| Length (mm) | Diameter (mm) | $\sigma_3$ (MPa) | Failure Load (kg) | kg/cm2 | $\sigma_1$ (Mpa) | Cohession (MPa) | Internal Friction Angle |
|---|---|---|---|---|---|---|---|
| 121.58 | 52.56 | 2.5 | 19481 | 897.86 | 88.08 | 8.82 | 57.08 |
| 121.56 | 52.5 | 5 | 25947 | 1198.61 | 117.58 | | |
| 121.44 | 52.31 | 7.5 | 31848 | 1481.91 | 145.38 | | |

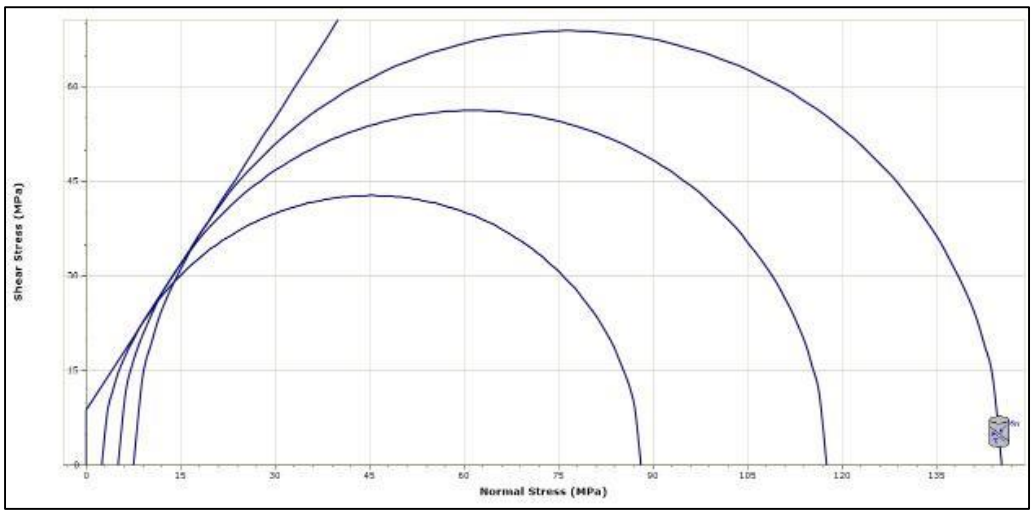


Figure 33. Mohr Circles and Failure Envelope for the marble specimens

Deformability tests were also carried out using cylindrical core specimens, apart from the UCS and TCS testing studies. The view of the test setup is given in Figure 35. It has the same setup as the UCS test mentioned above. Similarly, the loading duration has to be 5-10 minutes until failure, and the specimen size is prepared with a length-to-diameter (L/D) ratio of 2.5-3.0. A circumferential measurement system of a ring extensometer is placed around the sample to measure the diametrical enlargement during loading. The Poisson's ratio is calculated according to the increase in diametral strains in compression samples, which varies based on the shortening ratio in length. In other words, the axial unit and radial unit deformations are calculated with the aid of a ring extensometer in the testing device.


Figure 34. The view of the test setup of deformability test. The red rectangular area shows the ring extensometer

For the axial deformation ($\varepsilon_a$);

$$\varepsilon_a = \Delta l / l_0 \qquad (4.1)$$

Δl: Indicates length variation of the sample in the axial direction (In compression tests, the length change is in the negative direction and is defined as positive.)

$l_0$: The original size of the sample before the experiment.

For the radial deformation ($\varepsilon_d$);

$$\varepsilon_d = \Delta D / D_0 \qquad (4.2)$$

ΔD: Indicates a diametrical change in the sample. (pressure tests show an increase in diameter, which is defined as negative.)

$D_0$: The original size of the sample before the experiment.

To determine the axial stress, the applied load is divided by the initial area of the sample.

$$\sigma = P / A_0 \qquad (1.3)$$

σ: Axial stress

P: Load

$A_0$: Sample initial area

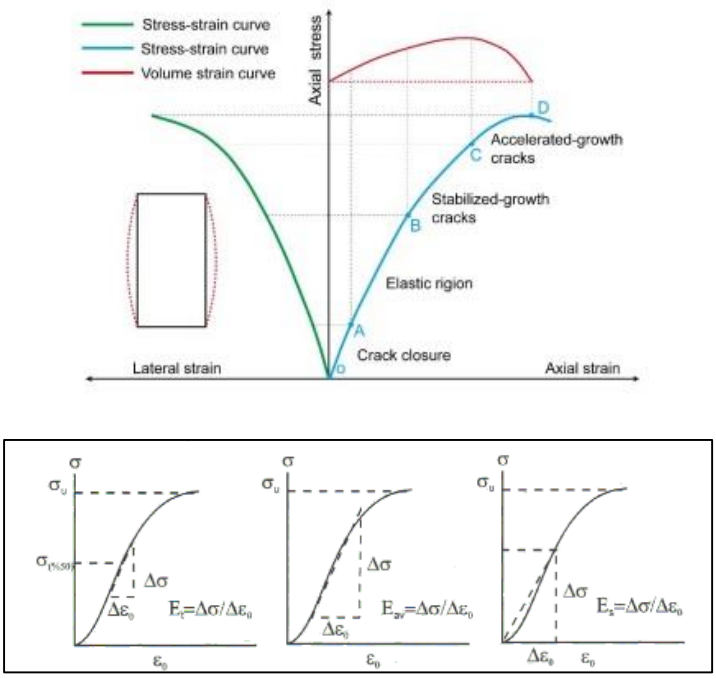


Figure 35. The deformability test graphs represent the stress vs. strain curve (ISRM 2007)

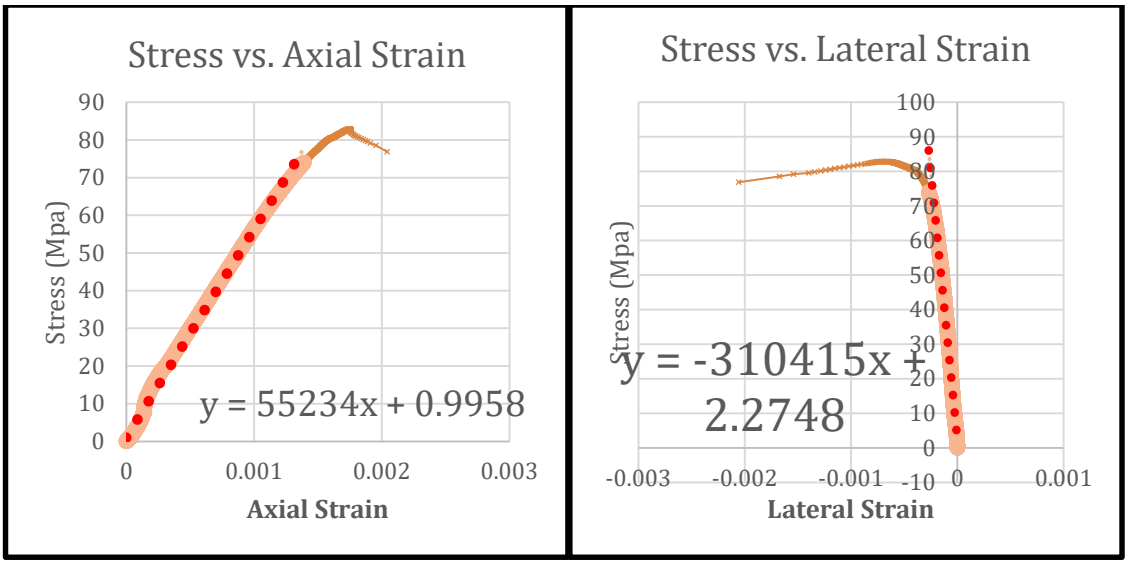


Figure 36. Stress-Strain curves of the marble specimen

The obtained deformability results of the marble sample based on the calculations performed in light of this information are given in Table 4.

Table 4. The strength deformability test results of the marble specimens

| Avg UCS (MPa) | Young's Modulus (MPa) | Avg Young's Modulus (MPa) | Avg Poisson's Ratio (MPa) |
|---|---|---|---|
| 90.35 | 55.23 | 57.16 | 0.14 |

### 4.4 Point Load Test

Finally, the point load tests have been carried out to determine the $I_{s(50)}$ parameters and uniaxial compressive strengths (UCS) results by using the block (or box) samples obtained from the marble blocks taken from the field. Point load tests were performed according to the International Society for Rock Mechanics (ISRM, 2016). The view of the test setup is given in Figure 37. Within the scope of these experiments, block samples of marbles obtained from the field survey locations were cut and trimmed (Figure 38). Then, based on the dimensions of the samples, loading measurements of the point load testing results at failure were recorded.


Figure 37. A view of the test setup of the point load test.


Figure 38. A view of the point load box samples prepared from the marble blocks

This test is carried out to determine the point load strength index which is used to classify rocks according to their strength. The point load strength index is used as the strength parameter of the rock material for the indirect determination of other strength parameters such as uniaxial compression, tensile strength, and the determination of fracture toughness. It is also utilized as the strength parameter of the rock material in some rock mass classification systems. In addition to block samples, cylindrical core and irregularly shaped samples can also be used for this experiment. Within the scope of this study, appropriate scale box samples were tested (Figure 39). For this testing procedure, block samples with a W/D ratio of 0.3 and 1.0 were prepared according to ISRM standards. The block sample has been placed between the conical loading heads perpendicular or parallel to the block axis. The sample was loaded in 10-60 seconds, and the results were obtained from the load at failure (P), which is the load indicator.

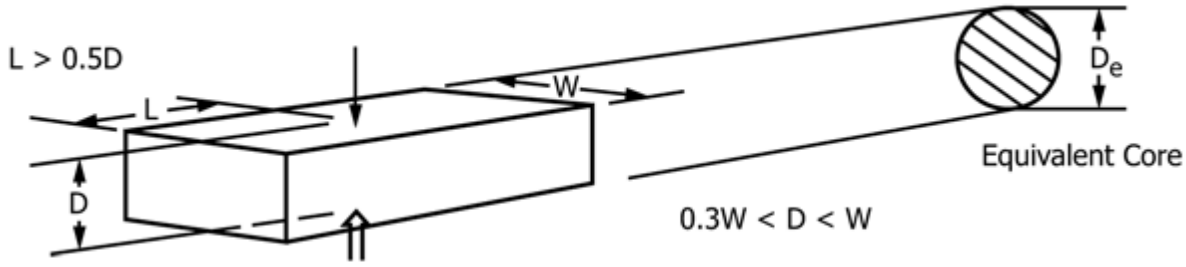


Figure 39. Box sample standards for point load (ISRM 2007)

Figure 40. The view of the valid block obtained after performing the point load (ISRM 2007)

In this test, the uncorrected point load strength index is calculated.

$$l_s = P/D_e^2 \qquad (4.4)$$

P: Load value at the time of failure.

$D_e$: Equivalent core diameter.

$D_e^2$: Test sample area. $D^2$ for core samples and $4A/\pi$ for axial, blocks, and irregular samples.

A: WD = minimum cross-sectional area of a plane through the platen contact points (See Figure 4039 above)

In this approach, the adjusted point load strength index, ls (D), is defined as the value of Is that would have been determined by a diametral test with D = 50 mm and given the symbol Is (50). Since that dimension is related to rock quality designations (RQD) and most NX core samples, 50 mm has been the recommended diameter. However, it is not

always practical to obtain a 50 mm sample. Therefore, the ls value must be corrected for a standard core diameter (D=50 mm). The equation to be used in size correction is:

$$l_{s(50)} = F/l_s \tag{4.5}$$

Where F is the size correction factor;

$$F = (D_e/50)^{0.45} \tag{4.6}$$

The point loading tests performed are shown in Table 5 below.

Table 5. The point load UCS results of the marble specimens

| Avg Failure Load (kgf) | Avg Failure Load (kgf) | Avg Axial $I_{s(50)}$ (MPa) | Stdev Axial Is(50) (MPa) |
|---|---|---|---|
| 708.143 | 269.91 | 4.31 | 1.5 |

Detailed calculations of the experiment are given in Appendix B.

# 5. HYDRAULIC FRACTURING

## 5.1 Brief History of Fracturing Operations

Although hydraulic fracturing started to be used for enhanced geothermal systems in the early 1970s, fracturing history dates back to the 1900s, and the first applications were performed without any fluid. The first cracking attempts were made with explosives to improve permeability in the petroleum industry. Gunpowder was used at first, and then liquid nitroglycerin was used later (Testa, 2017). Both materials were hazardous and unstable. The use of gunpowder-loaded explosives developed in 1866 and called torpedos (Roberts 1866) was applied in wells could cause the cracks in the well to become larger or the cracks in the well to collapse. Therefore, there were problems with both installation and operation. Thus, this method was not accepted as practical, and acid fracturing methods were used until 1947.

The first hydraulic fracturing experiment was conducted in 1947 in the Hugoton gas field in Kansas (Testa, 2017). Although this experiment was insufficient to increase production, it is accepted as the birth of hydraulic fracturing, and since that day, over 2.5 million fracture operations have been performed (Montgomery et al., 2010). In 1957 Hubbert proposed a theory for fracture direction determination based on an impermeable, isotropic, and linear elastic medium. This theory states that hydraulic fracturing directions are perpendicular to the minimum principal stresses, and even there are natural fractures, the propagation regime will try to be in this direction (Figure 41). With this theory, hydraulic fracturing ceased to be a spontaneous crack propagation and became a more understandable phenomenon and led this method to enter the geothermal field.

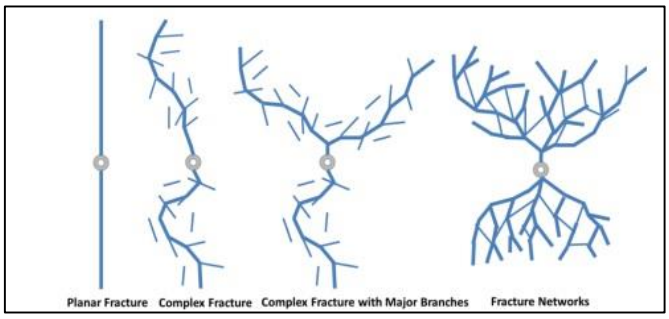


Figure 41. Hydraulic fracture propagation regime (Wang, 2019)

## 5.2 Hydraulic Fracture Modelling Parameters

The factors to be considered when designing hydraulic fracturing are as follows;

1. Rock properties
2. Field conditions
3. Fluid Rheology
4. Leak-offs
5. Proppants

### 5.2.1 Rock Properties

#### 5.2.1.1 Young's Modulus

Young's modulus will be the most important property for the rock in the reservoir where hydraulic fracturing will be operated. It is expected that the value of Young's modulus tends to increase as the formation becomes deeper and tighter (Boyun et al., 2017). The equation of elastic modulus is given below, and this equation is valid when the linear elasticity relationship holds.

$$E = \frac{\varepsilon_l}{\sigma_l} \tag{5.1}$$

However, Besides the elastic modulus known in cracking processes, there is also plane strain modulus. This modulus depends on both the elastic modulus and the Poisson's ratio.

$$E' = \frac{E}{1 - \nu^2} \tag{5.2}$$

However, this value is expected to be close to the elastic modulus value since reservoir rock's Poisson ratio ranges between 0.15 and 0.25.

#### 5.2.1.2 Fracture Toughness

Fracture toughness is a phrase that refers to a measure of a material's resistance to fracture expansion (Yew, 1997). This parameter is responsible for fracture initiation and needs to be overcome to lengthen the fractured matrix (Forbes Inskip et al., 2018). This parameter is denoted as Kıc, called tensile (Mode I) fracture toughness (Figure 42).

Mode I (opening fracture) is caused by tensile stress that is normal to the crack plane.

Mode II (shear fracture) is caused by shear stress acting perpendicular to the fracture and parallel to the crack plane.

Mode III (tearing) is caused by shear stress again, but the shear direction is parallel to the plane and fractures.

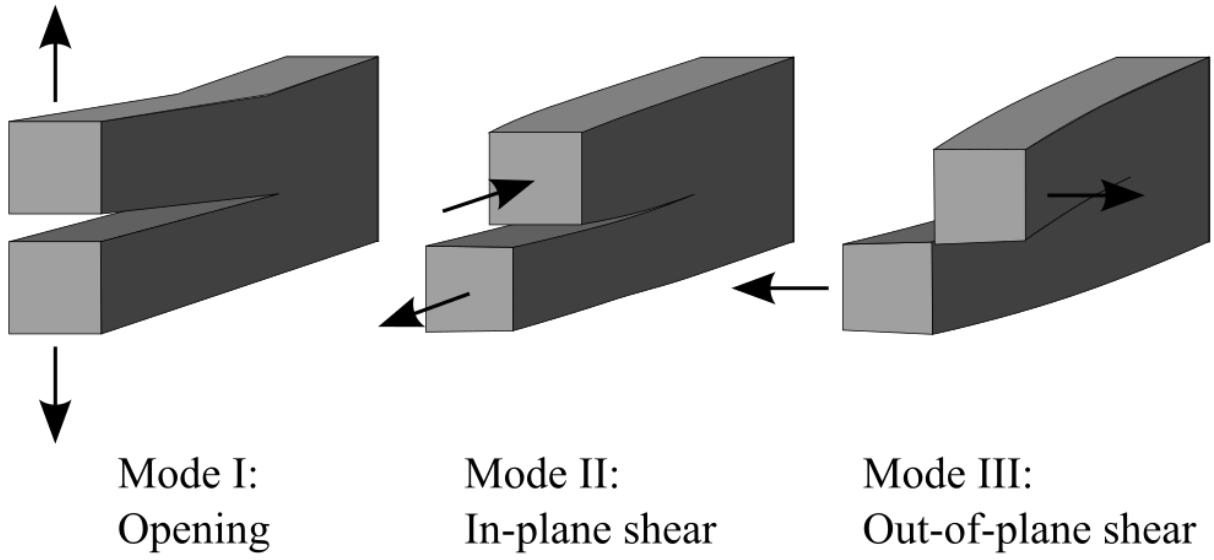


Figure 42. Types of fracture modes (Rountree et al., 2002)

Fractures formed during hydraulic fracturing are generally considered Mode I. This model is explained with a linear elastic fracture mechanism (LEFM). LEFM theory was developed by Griffith (1921) and improved by Irwing in 1957. The theory accepts that deformation at the fracture surface will be linearly elastic. Stress intensity can be shown as:

$$K_\iota = \sigma\sqrt{\gamma * H_\xi} \quad (2)$$

And for the failure condition;

$$\sigma_c = \frac{K_{IC}}{\sqrt{\gamma * H_\xi}} \quad (5.4)$$

Where $\gamma$ is represent geometric coefficient and $H_\xi$ represent the fracture dimensions.

Fracture starts when the stress intensity factor (K1) reaches the critical value (K1c). K1c is an essential parameter since propagation initiation depends on it. Since $K_{1c}$ is a material property, it must be calculated experimentally (Boyun et al., 2017). Although fracture toughness does not affect crack orientations, it could be used to determine the amount of energy to initiate cracking since it is a failure criterion.

Mode I cracking toughness can be found by many test methods. Some of them are;

- Chevron Notched Short Rod
- Chevron Notch Round Bar in Bending (CB)
- Brazilian Disk in Diametral Compression

Despite ISRM 2014 suggesting these tests for standardization purposes, other rock material characterization tests are still used for fracture toughness determination due to difficulty in preparing the sample and finding the appropriate sample for these tests (Bearmann, 1999). Point load experiments are discussed in the Point Load Section.

Several studies have examined the relationship between the point load test and fracture toughness. The relation found as a result of the studies of Gunsallus and Kulhawy is given below as:

$$K_{\iota c} = (0.09951 l_{s(50)}) + 1.11 \quad (5.5)$$

However, the correlation coefficient of this study was not above the 0.7 R-value. Later, Bearman (1998) came up with the new equation for fracture toughness, and its correction factor was above 0.94 R. This equation was:

$$K_{ıc} = 0.209 l_{s(50)} \tag{5.63}$$

$$K_{ıc} = 0.209 * (\frac{D}{50})^{0.45} * \frac{P}{D^2} \tag{5.7}$$

For diametrical cores:

$$K_{ıc} = \frac{29.84 * P}{D^{\frac{3}{2}}} \tag{4}$$

For axial tested samples:

$$K_{ıc} = \frac{26.56 * P}{(W * D)^{\frac{3}{4}}} \tag{5.9}$$

$K_{ıc}$ is Mode I fracture toughness ($MN/m^{3/2}$)

P is the force at failure (kN)

D is the distance between point load platens (mm)

W is the minimum width of the test piece (mm)

According to Berman's equation, the average fracture toughness was estimated as 0.9 $MPa*m^{1/2}$.

### 5.2.2 Principal Stresses

Zoback and Haimson (1981) stated that hydraulic fracture propagates perpendicular to minimum principal stress. In addition, this theory that has been proven in laboratory settings (Mao et al., 2017) is because fracture propagation will move forward with minimum energy requirement against minimum principal stress. Because the least amount of energy is necessary to rupture a rock, a hydraulic fracture propagates typically perpendicular to the direction of the minor primary stress (Boyun et al., 2017). In addition, laboratory tests support this theory.

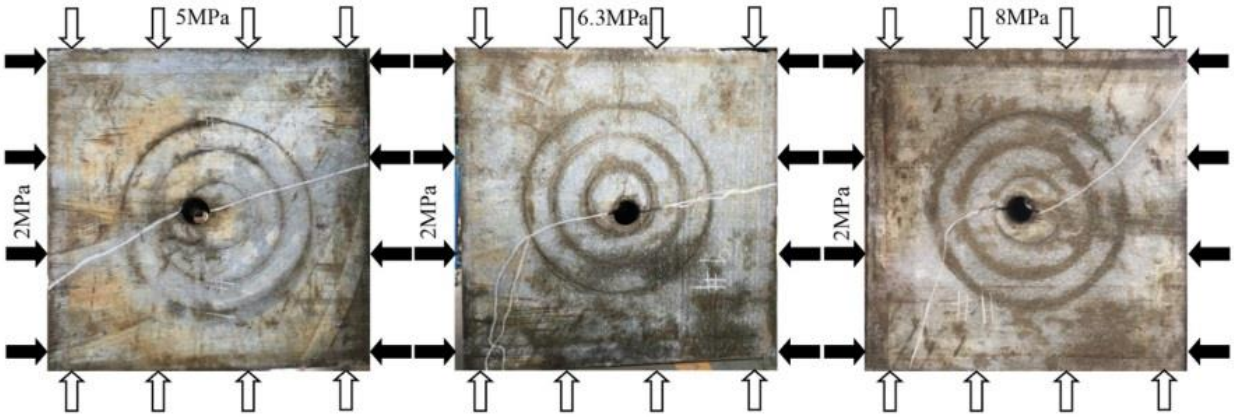


Figure 43. Fracture propagation directions according to stress directions (Mao et al., 2017)

In geothermal reservoirs, the maximum principal stress is generally vertical due to the overburden stress. In this case, the intermediate and minimum stresses are horizontal. It is expected that the fractures will be in the vertical directions in these stress conditions. However, vertical stress cannot always be in a state of maximum stress. The overburden pressure might be less than the horizontal stress for shallow depths. Also, field tectonism affects the stress condition of the region. Anderson (1951) shows stress direction regarding fault type in the field. According to this study, in the case of normal faulting, the major principle stress will be vertical, whereas it will be horizontal for reverse faults. In strike-slip faults, both the maximum and minimum stresses are horizontal.

### 5.2.3 Fluid Rheology

The properties of the fracturing fluid, which is one of the main elements of hydraulic fracturing, directly affect the fracture mechanism. The fracture fluid is responsible for three major problems; the ability to start and continue fracture propagation, proppant transporting capacity, and leak-off into the reservoir (Economides & Nolte., 2000). Fluid rheology is heavily influenced by its content. Therefore, many laboratory experiments are carried out on fracturing fluids to determine their viscosity under shear stresses. For the Newtonian fluids, flow behavior will be:

$$\tau = \mu * \gamma \tag{5.105}$$

Where:

$\tau$ is the shear stress,

$\mu$ is the viscosity of the fluid,

$\gamma$ is the shear rate.

However, Newtonian fluids are not preferred much in fracturing processes (Roustaei et al., 2016). Instead, non-Newtonian fluids are used. Non-Newtonian fluids can have different viscosities according to their stress, which implies that the shear stress on the fluid can become thinner or thicker (Figure 44). During fracture operation, fluid is exposed to shear stresses due to pumping. After fracture starts pumping, the shear stress decreases but the temperature increases (Boyun et al., 2017)

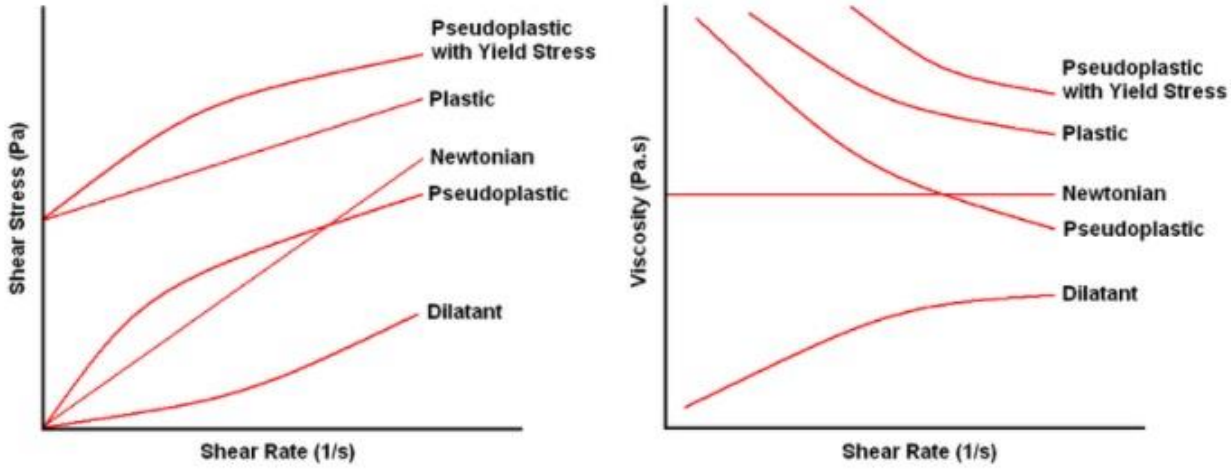


Figure 44. Flow behavior concerning shear conditions

As the figure shows, dilatant fluids become thicker when exposed to a shear load. This behavior can be accepted (i.e., shale gas operations) due to wider fractures being effective for more oil/gas production. However, dilatant behavior can be problematic in hot-dry rock operations. Dilatant fluids can cause the cracks to grow too wide and the fracture length shorter than desired since enhanced geothermal energy is about conductivity and heating. These wide cracks can cause insufficient heat exchange surface and short circuits. Also, smaller fracture lengths imply a shorter reservoir lifespan. Silica and polyethylene glycol suspension can be an example of shear thickening fluids; however, since pseudoplastic fluids show shear thinning behavior, their apparent viscosity gets smaller with shear stress. Hence, this implies that the liquid becomes more viscous, and its resistance to flow decreases and allows the fluid to flow more easily while fracturing

under shear stresses. Also, low viscosity allows fluid to flow back without any damage to the fractal matrix. Flow behavior of shear-thinning of fluid is illustrated in the study of Prud'homme et al. (1989) (Figure 45). The power law is used when calculating non-Newtonian fluids.

$$\tau = K * \gamma^n \tag{5.11}$$

Where K is the consistency index in kPa*s$^n$

n is the flow behavior index (dimensionless)

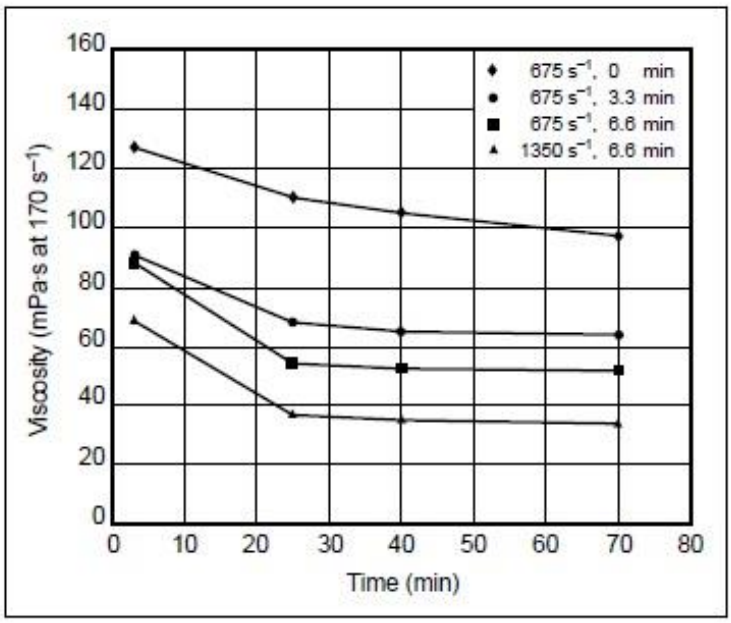


Figure 45. Apparent viscosity concerning time during the fracture operation (Prud'homme et al., 1989)

### 5.2.4 Leak-off

During hydraulic fracturing, the fluid pressure inside the fracture rises to higher levels than the minimum stress and pore pressure. Due to this pressure difference, the fluid goes out of the reservoir, and some fluid loss occurs. This phenomenon is called leak-off. Carter introduced the first primary leak-off equation in 1957. Leak-off has been analyzed in 3 different sections (Figure 46).

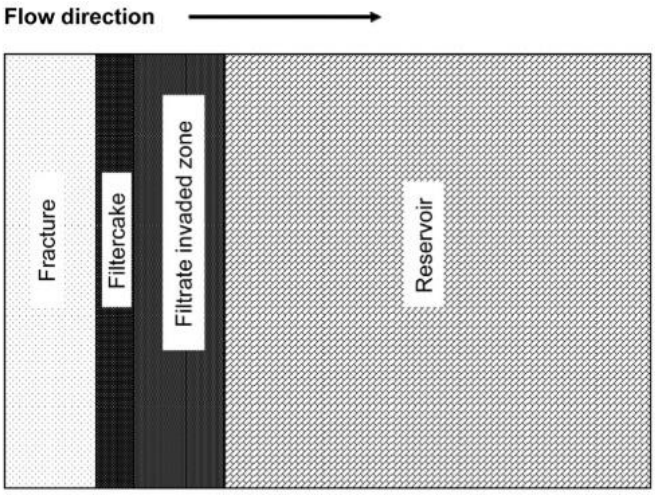


Figure 46. Leak-off regions

### 5.2.4.1 Filtercake Formation

A drilling mud intended features include minimizing fluid loss from the wellbore into the surrounding permeable rock (Sheerwood & Meeten, 1997). Particles that cannot pass through the pores during hydraulic fracturing accumulate outside the formation. First, relatively small particles fill the pre-existing reservoir cracks, and then large particles accumulate and form a low permeable layer on the reservoir.

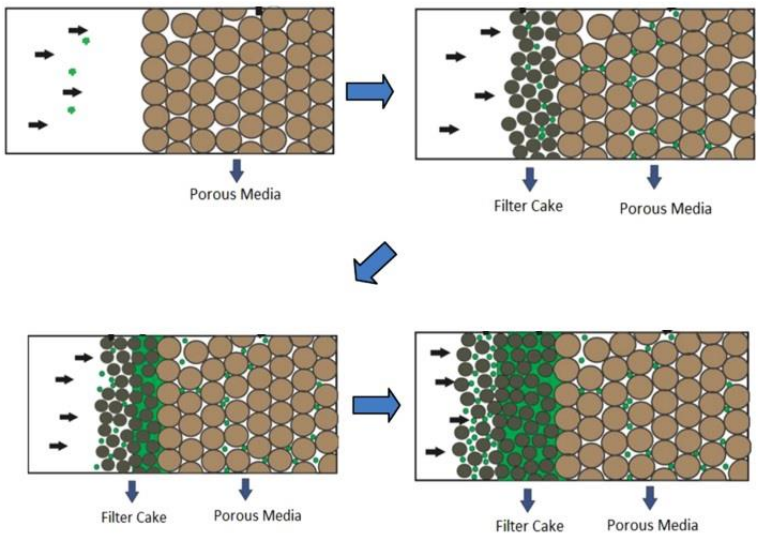


Figure 47. Filter cake formation (Sacramento et al., 2015)

Through filter cake, mass balance and Darcy's law govern the fluid leak-off process. Despite filter cake being considered a low permeable layer, there will be some fluid loss

until the filter cake formation is occurred. The name of the initial fluid loss is spurt loss. The volume of the leak-off through filter cake is:

$$L_c = \frac{V_c}{\alpha} \tag{5.12}$$

$$\alpha = \frac{C}{(1-\phi_c) * \rho} \tag{5.136}$$

$L_c$ is the filter cake thickness,

$V_L$ is the volume of the fluid loss,

C is mass concentration,

$\Phi_c$ is the filter cake porosity,

ρ is the density of the fluid.

α is Biot's poroelastic constant.

For the leak-off velocity calculation, according to Darcy's Law,

$$u_L = \frac{k_c}{\mu_f} \frac{\alpha \Delta p_c}{V_L} \tag{5.14}$$

$u_L$ is leak-off velocity,

$k_c$ is the filter cake permeability,

$\mu_f$ is filter cake viscosity, and

$\Delta p_c$ is a pressure difference.

This differential equation above is only applicable after the initial surge loss when a filter cake develops. With this condition, the volume of fluid loss will be equal to the volume of spurt (initial) loss.

$$V_L = 2 * C_w(\sqrt{t - t_{sp}}) + V_{sp} \tag{5.15}$$

$$C_w = \sqrt{\frac{k_c}{\mu_f}\frac{\alpha \Delta p_c}{2}} \tag{5.16}$$

$C_w$ is the leak-off coefficient of the filter cake.

$t_{sp}$ is the time of the spurt loss

$V_{sp}$ is the spurt loss time.

The value of the filter cake leak-off and initial loss parameters are calculated with laboratory experiments.

#### 5.2.4.2 Infiltrated zone

Darcy's laws are still valid for this situation too. The only assumption that has to be made is filter cake and reservoir, and fracturing fluid is incompressible.

$$u_L = \frac{k_f}{\mu_f}\frac{\Delta p_v * \phi}{V_L} \tag{5.17}$$

$k_f$ is the permeability of the zone,

$\Delta p_v$ is a pressure difference,

Φ is reservoir porosity.

İntegrating this equation yields:

$$V_L = 2 * C_v\sqrt{t} \tag{5.18}$$

$C_v$ is the leak-off coefficient of the filtrate zone.

$$C_w = \sqrt{\frac{k_c}{\mu_f}\frac{\phi \Delta p_v}{2}} \tag{5.19}$$

### 5.2.4.3 Reservoir Leak-off

Even though the uninvaded reservoir lacks fracturing fluid, pressure is necessary to push the reservoir fluid away from the fracture face (Economides & Nolte., 2000). Assumptions; compressive flow, slow movement, and infinite reservoir area. For the calculations of the leak-off coefficient of the reservoir region, Collins (1961) had used the equation below;

$$u_L = \frac{C_c}{\sqrt{t}} \tag{5.20}$$

$$C_c = \sqrt{\frac{k * c_t * \phi}{\pi * \mu}} * \Delta p_c \tag{5.21}$$

$C_c$ leak-off coefficient of the reservoir,

K is the permeability of the reservoir,

$c_t$ is the compressibility of the reservoir,

μ is the viscosity, and

$\Delta p_c$ is a pressure difference.

### 5.2.4.3 Combined Leak-off

In genuine cases, all of these leak-off mechanisms develop simultaneously. It implies that the velocity of the leak-offs must be the same. Also, the summation of the pressure drops of leak-offs equals the total pressure change. Williams et al. (1979) found that combined leak-off coefficient with ignoring spurt time is very short compared to other leakage times. The total leak-off coefficient formula become;

$$C_L = \frac{2 * C_c C_v C_w}{C_v C_w + \sqrt{C_c^2 C_w^2 + 4C_c^2 * (C_v^2 + C_w^2)}} \tag{5.22}$$

$C_L$ is the total leak-off coefficient.

Carter (1957) is widely credited for developing the fluid leak-off techniques addressed in this section.

### 5.2.5 Proppants

A proppant is a solid substance, usually sand or man-made ceramic materials. It is used to maintain the openness of an induced hydraulic fracture during or after fracturing (Figure 48).

Figure 48. Proppant types (OPF Enterprises, LLC)

As the figure shows, proppants can be natural sand, resin-coated sand, or ceramic. Considering the depths at which the fracture is developed, the overburden stress will be very high, and fractures tend to close due to this stress. The primary purpose of proppants is to keep these cracks open (Figure 49). Proppant has to be strong enough to carry compression stress, and at the same time, it must not disturb the fluid flow by increasing its viscosity or decreasing reservoir conductivity. The features to consider when examining proppants are; compressive strength, grain size, roundness.

Proppant compressive strength is the most critical proppant parameter since the other parameters are valid when the fractures standstill. Thus, proppant has to overcome the overburden stress applied to it.

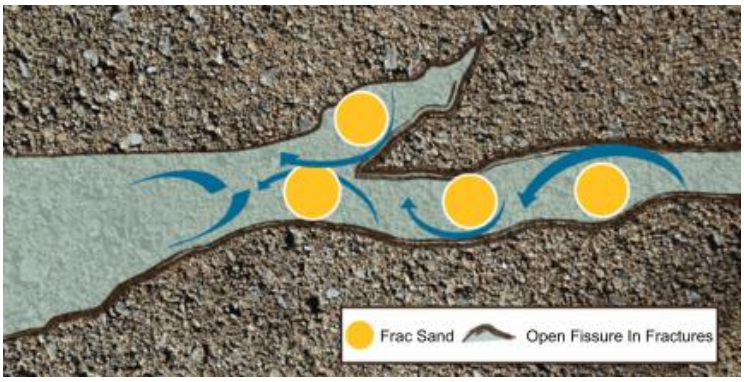


Figure 49. Proppants at the fractured media

Natural sand is the roughest, weakest, but cheapest option. Natural sands should be used at shallow fracturing operations that do not require compressive strength. When its low strength and angular structure are combined with high overburden pressure, it can create an impermeable structure as it is likely to be crushed under this stress. Resin-coated proppants tend to be more durable since their compressive strength is higher than natural sands, and their shape is rounder. This roundness ensures good conductivity by preventing the interlocking of the particles. Ceramic proppants (i.e., artificial) are the best option for engineering parameters since they have the highest compressive strength, possess uniform and round particles, and are lightweight. These parameters make the hydraulic fracture processes easier. However, these pleasant engineering parameters come with a downside. The downside is the cost of the ceramic proppants. According to Parker (2018), the cost of ceramic proppant can be up to 14 times the price of sand and 2-3 times the price of resin-coated sand. Figures 50 and 51 give the cost and properties of the proppants.

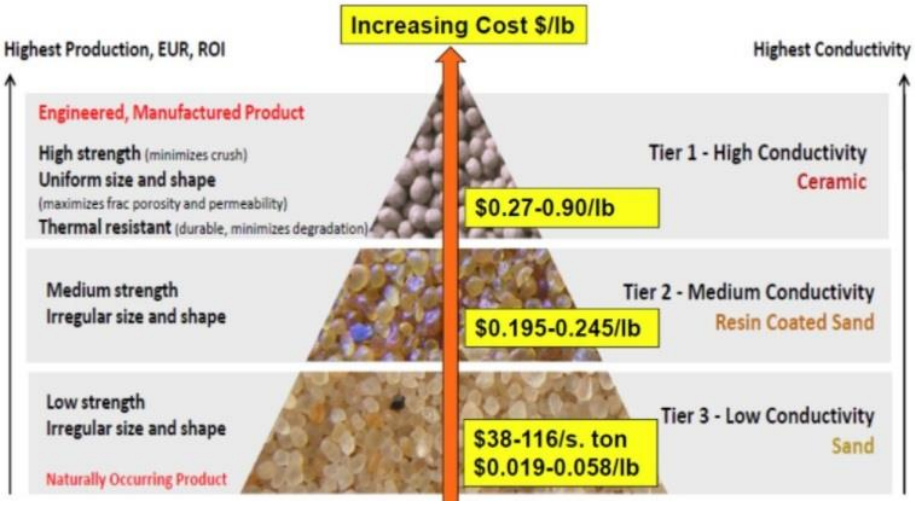


Figure 50. Proppant costs concerning their types (Parker, 2018)

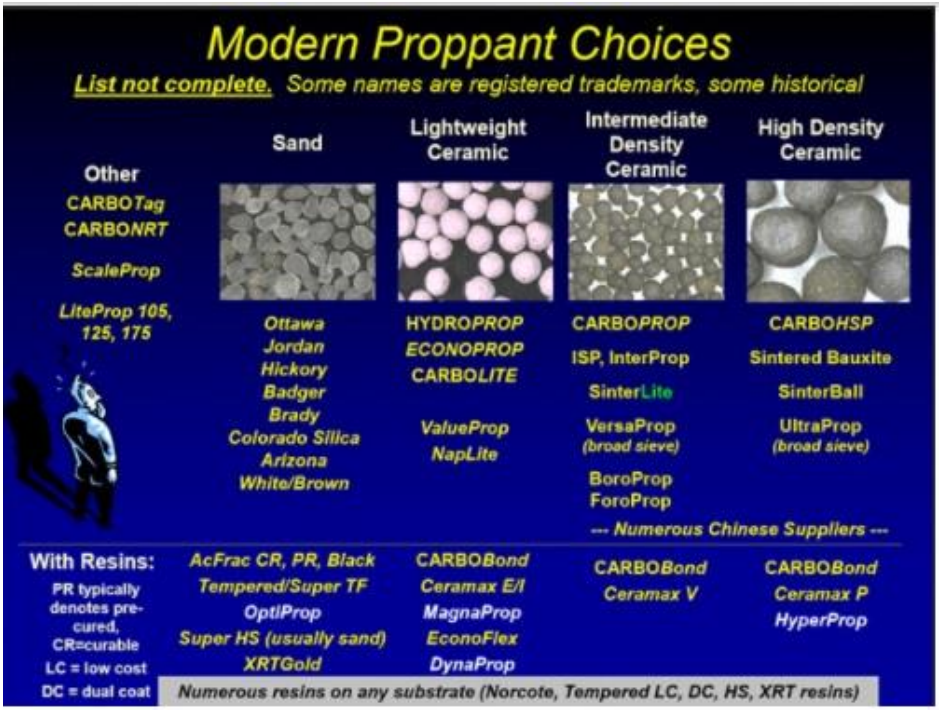


Figure 51. Proppant properties

### 5.3. Hydraulic Fracture Modelling

In 2D hydraulic fracture modeling, there are three types of model approaches. These are radial, PKN, and KGD models. Sneddon and Elliot (1946) developed the radial modeling approach that assumes penny-shaped fracture properties (width and length of the fracture). Perkins-Kern-Nordgren developed another hydraulic fracture modeling solution in 1972 (Nguyen et al., 2020). Another 2D pseudo modeling is the Khristianovich and Zheltov (1955) model. The KGD and PKN models forecast fracture width and extent by assuming a fixed fracture height (Boyun et al., 2017). They made some assumptions to solve hydraulic fracture propagation problems. These assumptions are that the reservoir exposed to fracturing is homogeneous and isotropic, fracture propagation has linear elastic stress-strain relations, fluid flow is laminar, and the gravity effect is ignored.

### 5.3.1 Radial Modelling

In 1946, Sneddon and Elliot established a solution for the pressurized cracks. The shape of the fracture propagation is circular (Penny-shaped). The equation for the penny-shaped fracture is:

$$w = \frac{8p_n R(1-\nu^2)}{\pi E}\sqrt{(1-(\frac{r}{R})^2} \tag{5.23}$$

w is the width of the fracture,

R is the radius of the total fracture area.

For the volume of the fracture;

$$V = \frac{16(1-\nu^2)R^3}{3E}p_{net} \tag{5.24}$$

Where $p_{net}$ is the net pressure,

ν is the Poisson's ratio,

E is Young's Modulus.

### 5.3.2 PKN Model

Perkins and Kern developed this model in 1961 without considering fluid loss. Their assumption was fixed fracture height and elliptical fracture shape.

The fracture width formula was developed by combining a planar strain elasticity equation with a viscous fluid flow equation. The fracture width formulation is:

$$w_{max} = 3\left[\frac{(1-\nu^2)\mu q_i(x_f - x)}{E}\right]^{0.25} \tag{5.25}$$

$x_f$ is the fracture half-length.

$W_{max}$ is the maximum fracture width.

$p_{net}$ is the net pressure,

$h_f$ is the fixed fracture height,

$q_i$ is the flow rate.

To create the desired amount of crack width, the pressure formula will be:

$$p_{max} = \frac{3(\mu q_i x_f)^{0.25}[E/(1-\nu^2)]^{0.75}}{2h_f} \tag{5.26}$$

In 1972 Nordgren modified the Perkins and Kern model, now known as the PKN model, to include fluid loss and storage, and came up with a new set of solutions. The equation indicates that when the elastic modulus is high for the reservoir, the pressure to initiate fracture will be higher, and the fracture width will be smaller.

### 5.3.4 KGD Model

Published by Khristianovich and Zheltov (1955), the model assumes that the fracture shape is rectangular with constant height. The model takes into account the fracture tips for the fracture mechanics. In order to achieve a solution, the problem has been simplified assumptions have been made about constant flow rate and pressure in the fractured matrix. Later, Geertsma and de Klerk (1969) solved that approach and developed a boundary condition. If this condition is met, the normal stress at the tip will be finite and equal to the rock's tensile strength. Furthermore, the tensile strength can be considered minimal (Boyun et al., 2017). According to the KGD model, the relationships between fracture width and reservoir parameters can be presented by the equation below:

$$w_w = \left[\frac{84(1-\nu^2)\mu q_i L^2}{E\pi h_f}\right]^{0.25} \tag{5.27}$$

Figure 52 shows the geometrical properties of the fractures according to different 2D pseudo models. Figures 53 and 54 represent the views of the 2D model approaches.

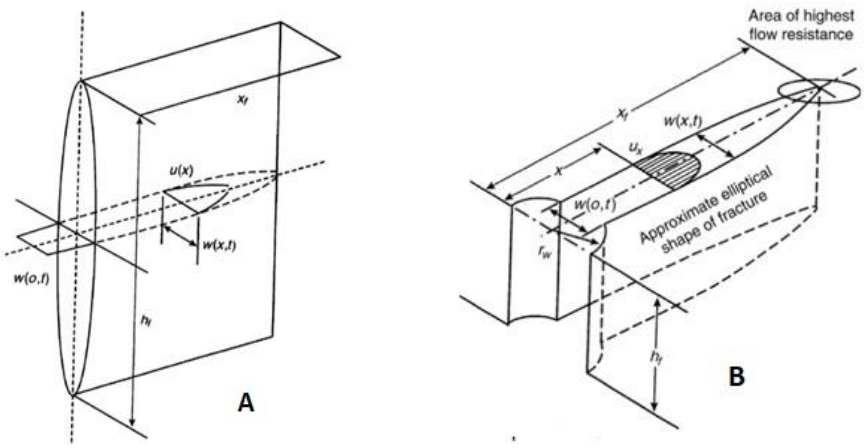


Figure 52. A) represents the PKN Model and B) represents the KGD Model

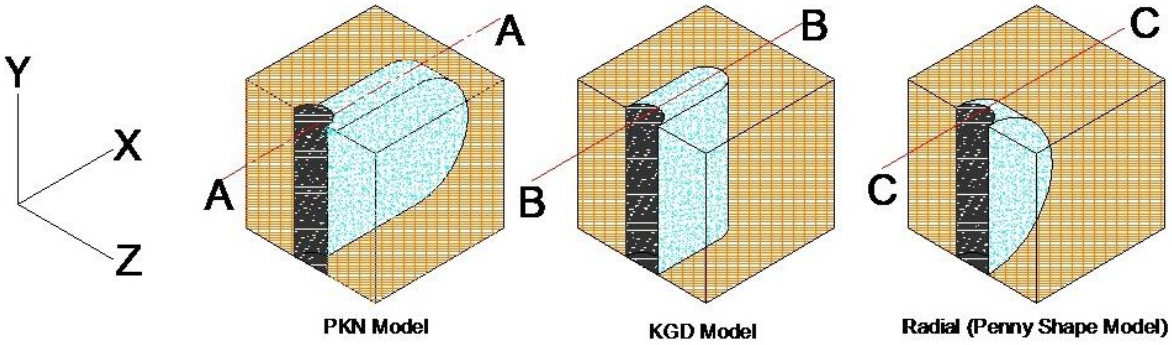


Figure 53. Isometric view of the fracture geometry concerning the modeling approach

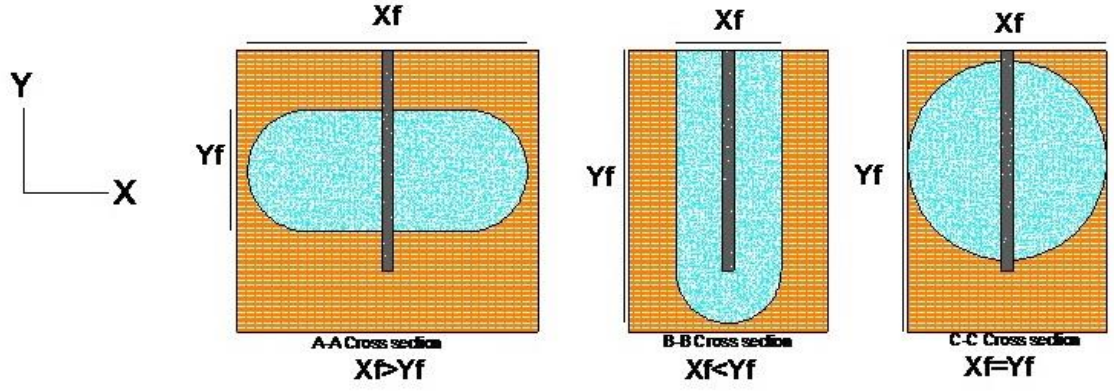


Figure 54. Cross-section of the fracture geometry for modeling approach

### 5.4 Hydraulic Fracture Modelling by using Mfast Software

MFast is a two-dimensional hydraulic fracturing software developed by Baker Hughes company, allowing building 2D fractures analytically. The software allows the comparison between three different 2D pseudo models. The simulator highlights the relevance of numerous factors while also providing a quick first-order approximation to fracture design, net pressure, fracture efficiency, and treatment design. The software provides first-order estimation based on the fracture geometry.

Input parameters for Mfast Software;

1. Young's Modulus
2. Fracture Toughness
3. Poisson's Ratio
4. Total Payzone Height
5. Total Fracture Height
6. Ellipsoidal Aspect Ratio
7. Injection Rate
8. Flow Behavior Index
9. Consistency Index
10. Total Leak-off Coefficient
11. Spurt Loss Coefficient
12. Total Volume Injected
13. Max Proppant Concentration

Before modeling hydraulic fracture for an enhanced geothermal system, the material properties (E, $K_{ıc}$, ν) should be reconsidered. While there is no problem in using them in projects made to extract shale gas, geothermal projects should consider the temperature since rock temperatures in enhanced geothermal system reservoirs are 100-300 °C (Zhang et al., 2020) state that the uniaxial compressive strength of the rock material will decrease slightly between 20 °C and 200 °C. Between 300 and 500 degrees, this decline accelerates. Due to thermal effects, material parameters will be reduced. The reduction amount is determined in the light of Zhang et al. (2020). According to this study strength of the rock decreased 10%, 20%, and 30% at 200 °C, 300 °C and 500 °C, respectively. Therefore, previously found values have been updated as follows. Young's modulus

reduced to 50 GPa from 55 GPa, and fracture toughness reduced to 0.81 from 0.91 $MPa.m^{0.5}$.

### 5.4.1 Sensitivity Analyses

As mentioned before, Mfast software is used for preliminary analysis to understand fracture geometry, and it demands 13 different parameters that cannot be obtained without extensional research. Therefore, sensitivity analyzes were performed to find the most appropriate situation. As a result of the evaluations developed, it was decided that the KGD model was more suitable because vertical cracks would be more dominant.

#### 5.4.1.1 Young's Modulus

Even though Young's modulus is a rock material parameter and was determined with the laboratory testing studies of the marble samples mentioned before, sensitivity analyses were also performed based on this parameter to understand it better. Young's modulus analyses examined modulus results between 40 and 60 GPa. Table 6 and Figure 55 show the relationships between Young's modulus and fracture length-width.

Table 6. The tabulated results between Mod and fracture dimensions

| E (Mpa) | 42000 | 44000 | 46000 | 48000 | 50000 | 52000 | 54000 | 56000 | 58000 | 60000 |
|---|---|---|---|---|---|---|---|---|---|---|
| Length (m) | 701.05 | 707.88 | 714.46 | 720.81 | 726.94 | 732.88 | 738.64 | 744.22 | 749.64 | 754.91 |
| Width (cm) | 1.1887 | 1.1772 | 1.1664 | 1.1561 | 1.1464 | 1.1371 | 1.1282 | 1.1197 | 1.1116 | 1.1039 |

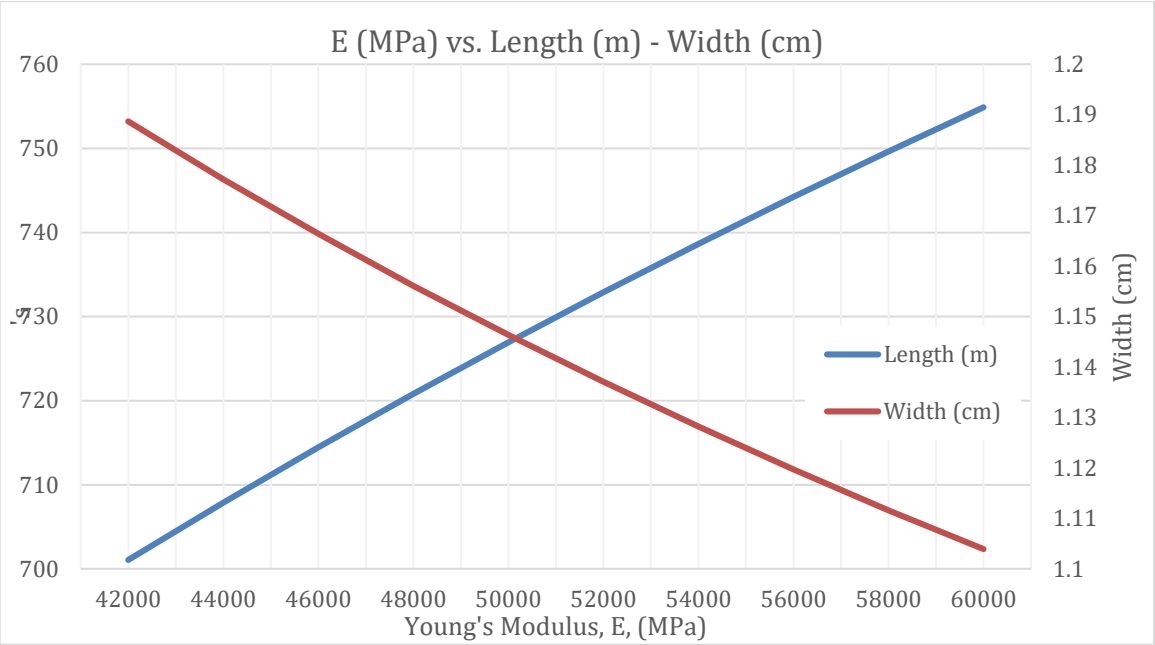


Figure 55. The relationships between Young's Modulus and fracture dimensions

### 5.4.1.2 Poisson's Ratio

Similar to Young's modulus, sensitivity analyses were performed, although Poisson's ratio was determined from the rock mechanics laboratory tests to analyze its effects on the fractal geometry. Table 7 and Figure 56 show the relationships between the fractal geometry and Poisson's ratio.

Table 7. The tabulated results between Poisson's Ratio and fracture dimensions

| Poissons ratio | 0.1 | 0.12 | 0.14 | 0.16 | 0.18 | 0.2 | 0.22 | 0.24 | 0.26 | 0.28 | 0.3 |
|---|---|---|---|---|---|---|---|---|---|---|---|
| Length (m) | 725.47 | 726.15 | 726.94 | 727.87 | 728.93 | 730.12 | 731.45 | 732.93 | 734.55 | 736.33 | 738.26 |
| Width (cm) | 1.1487 | 1.1476 | 1.1464 | 1.1449 | 1.1432 | 1.1414 | 1.1393 | 1.137 | 1.1345 | 1.1317 | 1.1288 |

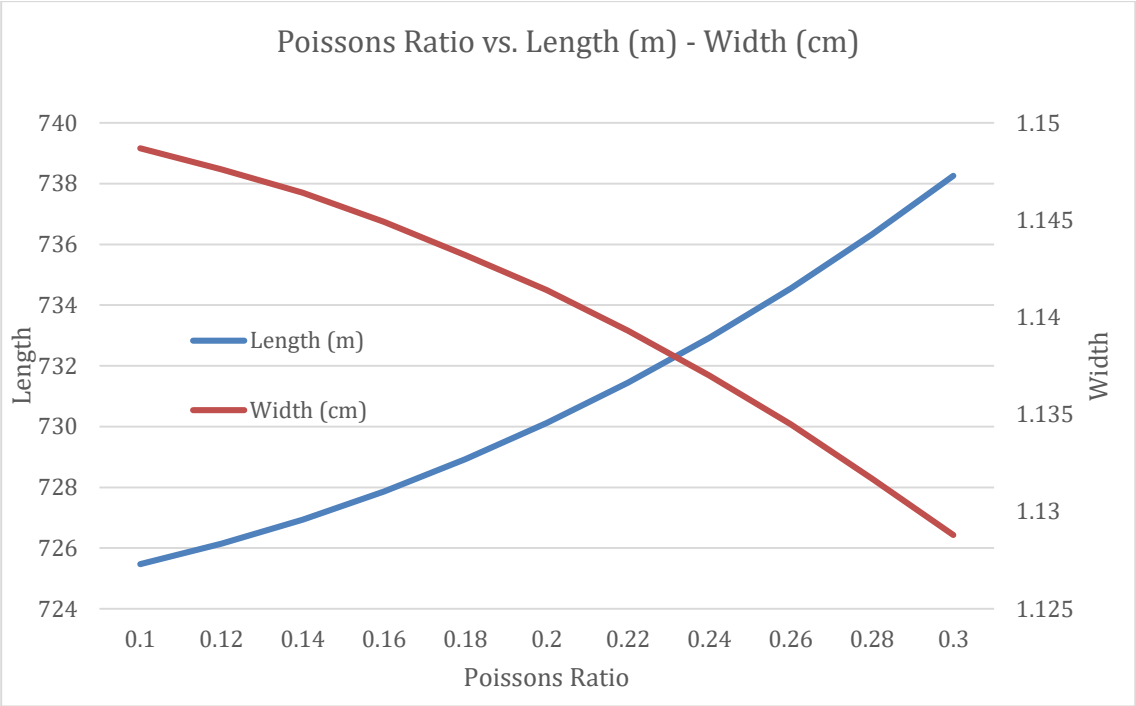


Figure 56. The relationships between Poisson's Ratio and fracture dimensions

Although the analyses showed a linear relationship between Young's modulus and cracking geometry, it was observed that there was an exponential relationship between Poisson's ratio and geometry. However, the Poisson's ratio increased three times, the fracture length was less than 2.5%, and the fracture width was almost the same. According to these results, Poisson's ratio does not affect the fracture geometry. In cases where Poisson's ratio cannot be determined, there is no harm in estimating it. Most rocks have a Poisson ratio in the range of 0.15 to 0.35 (Boyun et al., 2017).

#### 5.4.1.3 Fracture Toughness

Fracture toughness is a material attribute that characterizes the ability of the material to withstand fracture when subjected to a crack. In light of this definition, it has been observed that fracture toughness is more of a failure criterion and does not significantly affect the crack geometry. In addition to the crack geometry, a net pressure analysis was also performed. Tables and graphs of these analyses are given here.

Table 8. The results between fracture toughness and fracture dimensions along with the net pressure

| Fracture Toughness (Mpa*m$^{3/2}$) | 0.1 | 0.2 | 0.3 | 0.4 | 0.5 | 0.6 | 0.7 | 0.8 | 0.9 |
|---|---|---|---|---|---|---|---|---|---|
| Length (m) | 761.16 | 760.28 | 759.4 | 758.52 | 757.65 | 756.77 | 755.88 | 755 | 754.12 |
| Width (cm) | 1.0948 | 1.0961 | 1.0974 | 1.0986 | 1.0999 | 1.1012 | 1.1025 | 1.1037 | 1.105 |
| Net Pressure kPa | 356.94 | 357.77 | 358.59 | 359.42 | 360.26 | 361.1 | 361.94 | 362.79 | 363.64 |

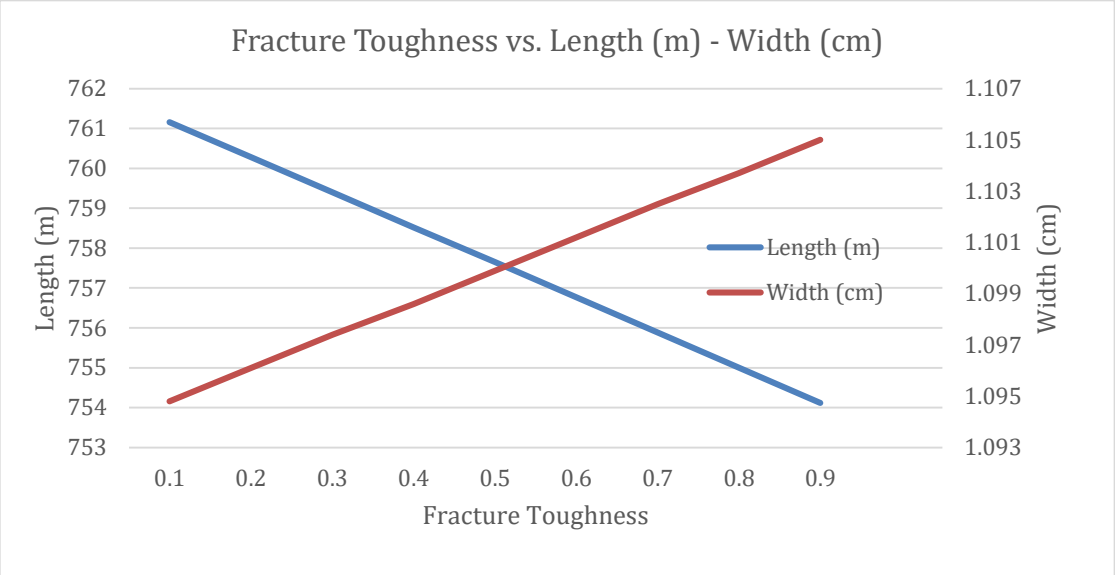


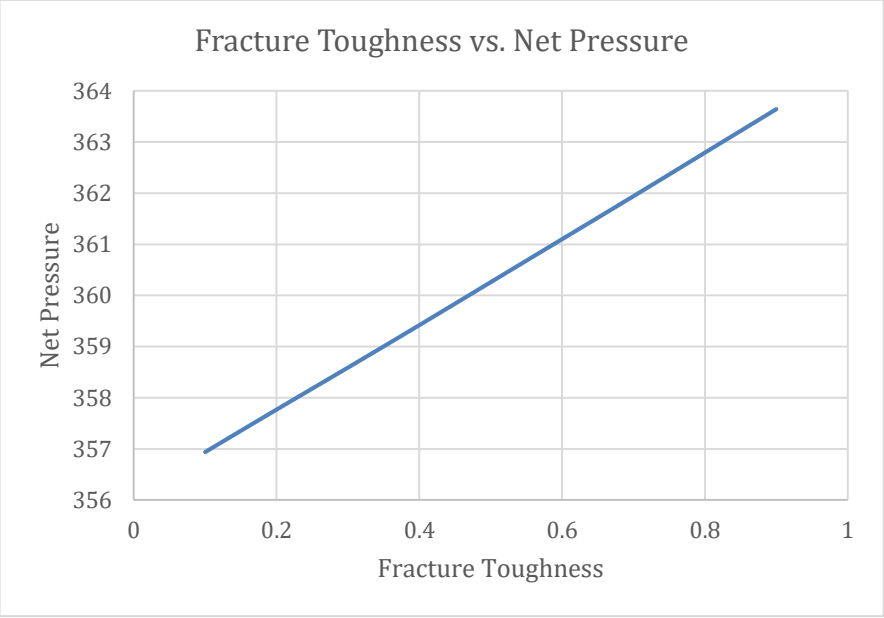


Figure 57. Effects of the fracture toughness on fracture geometry and required pressures

### 5.4.1.4 Flow Behavior Index

As discussed before, the flow behavior index determines the fluid behavior under shear stresses. Flow rate is the parameter responsible for the shear stresses during cracking. If

the flow rate is slow enough, it may not show the expected properties even if the fluid is pseudoplastic since it will not be exposed to high shear stresses. The pseudoplastic fluids flow behavior index <1 shows shear thinning behavior.

Table 9. Flow behavior index and its relation to the injection rate

| **Injection Rate $m^3$/min** | **10** | | |
|---|---|---|---|
| Flow behavior index | 0.4 | 0.5 | 0.6 |
| Lenght (m) | 447.22 | 461.13 | 477.18 |
| Width (cm) | 1.8634 | 1.8071 | 1.7464 |
| | | | |
| **Injection Rate $m^3$/min** | **5** | | |
| Flow behavior index | 0.4 | 0.5 | 0.6 |
| Lenght (m) | 484.15 | 493.94 | 505.29 |
| Width (cm) | 1.7212 | 1.6871 | 1.6492 |
| | | | |
| **Injection Rate $m^3$/min** | **1** | | |
| Flow behavior index | 0.4 | 0.5 | 0.6 |
| Lenght (m) | 581.91 | 579.25 | 576.99 |
| Width (cm) | 1.4321 | 1.4386 | 1.4443 |
| | | | |
| Total İnjected Volume $m^3$ | 2500 | | |

As the table shows, as the pumping speed increases, the shear load on the liquid increases, so pseudoplastic fluids can show shear-thinning and open longer cracks while, in return, this decreasing the fracture width.

#### 5.4.1.5 Consistency Index

The non-Newtonian properties of the flow are described using power-law rheology, in which the fluid consistency coefficient and flow behavior index are dependent on the nanoparticle volume percentage (Niu et al., 2012). Table 10 shows the relationships between the consistency index and fracture dimensions.

Table 10. The results of the consistency Index vs. fracture dimensions relation

| K value | 0.004788 | 0.009576 | 0.014364 | 0.019152 | 0.02394 | 0.028728 | 0.033516 | 0.038304 | 0.043092 | 0.04788 |
|---|---|---|---|---|---|---|---|---|---|---|
| Lenght (m) | 726.94 | 634.12 | 585.31 | 552.94 | 529.05 | 510.28 | 494.93 | 482 | 470.87 | 461.13 |
| Width (cm) | 1.1464 | 1.3142 | 1.4237 | 1.5071 | 1.5752 | 1.6331 | 1.6837 | 1.7289 | 1.7698 | 1.8071 |


Figure 58. The relationships between consistency index and dimensions of the fracture

### 5.4.1.6 Pumping Time

The formation of fractures that are larger than necessary in hydraulic fracturing processes leads to irreversible problems. Cracks opened larger than necessary will be insufficient in heat transfer, and this can cause the inability to produce energy. Therefore, fractures should be opened in a controlled manner and by observing. Therefore, an analysis of the pumping rate was developed, and the results are given in Table 11 and Figure 59.

Table 11. The pumping time analysis results

| Pumping Time | 3125 | 3571.4 | 4166.7 | 5000 | 6250 | 8333.3 | 12500 | 25000 |
|---|---|---|---|---|---|---|---|---|
| Length (m) | 592.17 | 600.03 | 609.24 | 620.31 | 634.12 | 652.38 | 678.98 | 726.94 |
| Width (cm) | 1.4073 | 1.3888 | 1.3678 | 1.3434 | 1.3142 | 1.2774 | 1.2273 | 1.1464 |
| Net Pressure | 491.45 | 478.65 | 464.29 | 447.87 | 428.57 | 404.92 | 373.81 | 236.11 |
| Injected Volum | 2500 | | | | | | | |

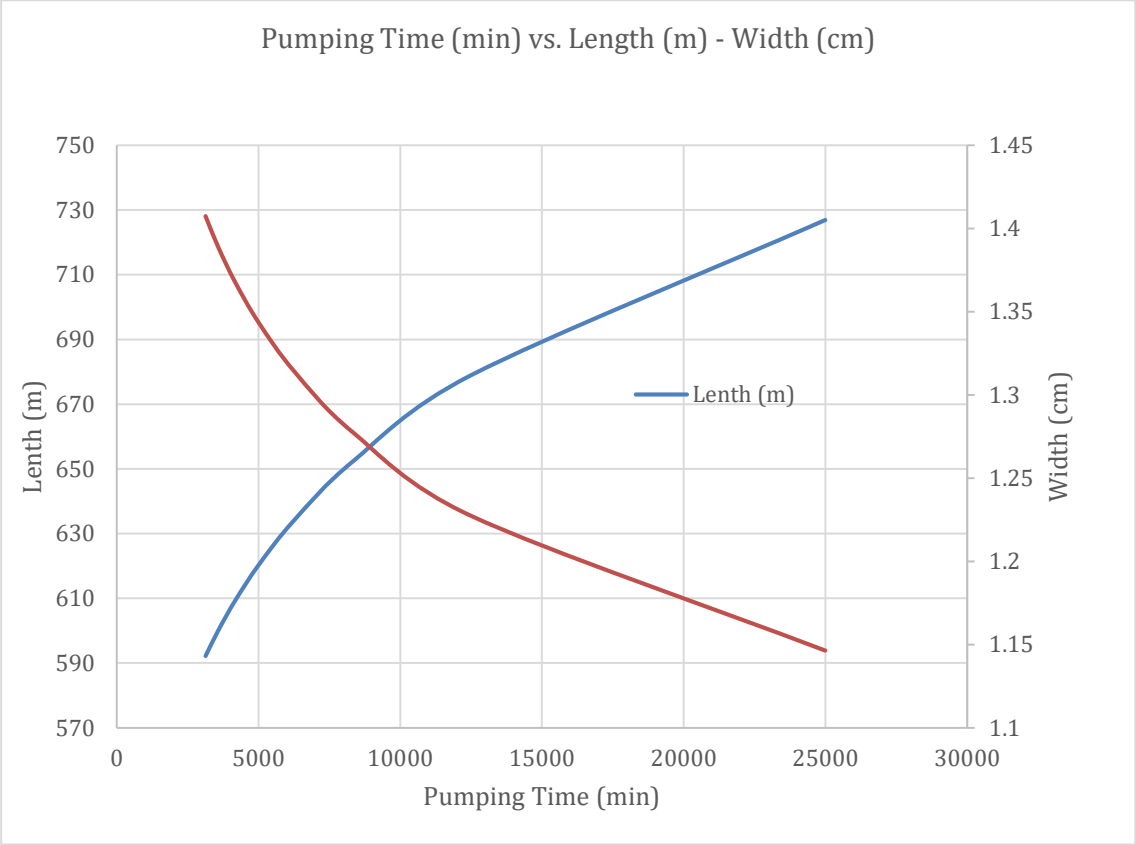


Figure 59. The relationships between pumping time and dimensions of the fracture

### 5.4.1.7 Proppant Type

Proppants are the most critical material for the continuity of the project. The use of sand as a proppant may cause problems in deep drilling due to overburden pressure. This situation has been explained in previous sections, and it has been stated that ceramic proppants are more suitable for enhanced geothermal systems. The percentage of fracture volume created that will remain supported after closure must also be analyzed. The proppant analyses are given in Table 12 and Figure 60.

Table 12. The results of proppant type and percent propped

| Proppant Type | Jordan Sand | IPP Interprop | Hickory Sand | Carbo-Lite | Bauxite Sint | AcFrac Proppant |
|---|---|---|---|---|---|---|
| Percent Propped | 106.15 | 97.979 | 106.15 | 99.186 | 75.806 | 110.68 |
| Max Proppant Concentration 100 kg/m³ | 17 | | | | | |

Despite sand proppants showing the maximum value of the percent propped for the reasons explained above, it is recommended to prefer ceramic proppants.

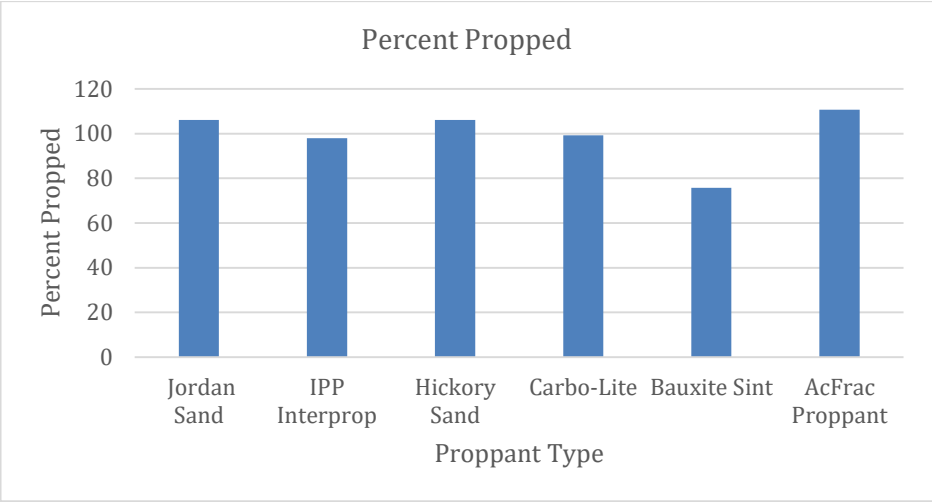


Figure 60. Proppant type and Percent Propped

### 5.5 Final Hydraulic Fracturing Model

The parameters were determined according to the results obtained from the literature studies, in-situ deep boring testing data, field reconnaissance studies, rock mechanics laboratory experiments, and sensitivity analysis. In the light of these results, the final modeling studies were developed. The modeling parameters are given in Table 13 below.

Table 13. Input parameters for the hydraulic fracturing operations

| Proppant Type: Carbo-Lite | | |
|---|---|---|
| Young's Modulus | 50000 | MPa |
| Fracture Toughness | 0.81 | MPa·m^½ |
| Poisson's Ratio | 0.14 | fraction |
| Total Pay Zone Height | 0.03048 | m |
| Total Fracture Height | 150 | m |
| Ellipsoidal Aspect Ratio | 1 | |
| Injection Rate (2-wings) | 0.1 | m³/min |
| Flow Behavior Index - n' | 0.5 | |
| Consistency Index - K' | 0.00479 | kPa·s^n' |
| Total Leak-off Coefficient | 0 | cm/min^½ |
| Spurt Loss Coefficient | 0 | cm |
| Total Volume Injected | 2500 | m³ |
| Max Proppant Concentration | 17 | 100 kg/m³ |

Based on the input parameters, the two-dimensional hydraulic fracturing model considering all data representing the reservoir in the marble unit of Bayırdır formation has been computed using MFast software, providing a quick first-order approximation to fracture design, net pressure, fracture efficiency, and treatment design. The output of the MFast modeling is given in Table 14.

Table 14. MFast software output based on the modeling parameters

| ***Output Solution*** | | |
|---|---|---|
| Parameters | GDK | |
| Length | 726.94 | m |
| Height (wellbore) | 150 | m |
| Max. Well Width | 1.4596 | cm |
| Average Well Width | 1.4596 | cm |
| Average Fracture Width | 1.1464 | cm |
| Net Pressure | 326.11 | kPa |
| Efficiency | 1 | fraction |
| Pumping Time | 25000 | min |
| Volume | 2500 | $m^3$ |
| Proppant Mass | 4.25E+06 | kg |
| Percent Propped | 99.186 | % |

Hence, the results based on the reservoir formation are presented considering fracture length vs. time and injected volume, fracture width vs. time and injected volume, pressure vs. time, and injected Volume from Figures 61 to 66, respectively.

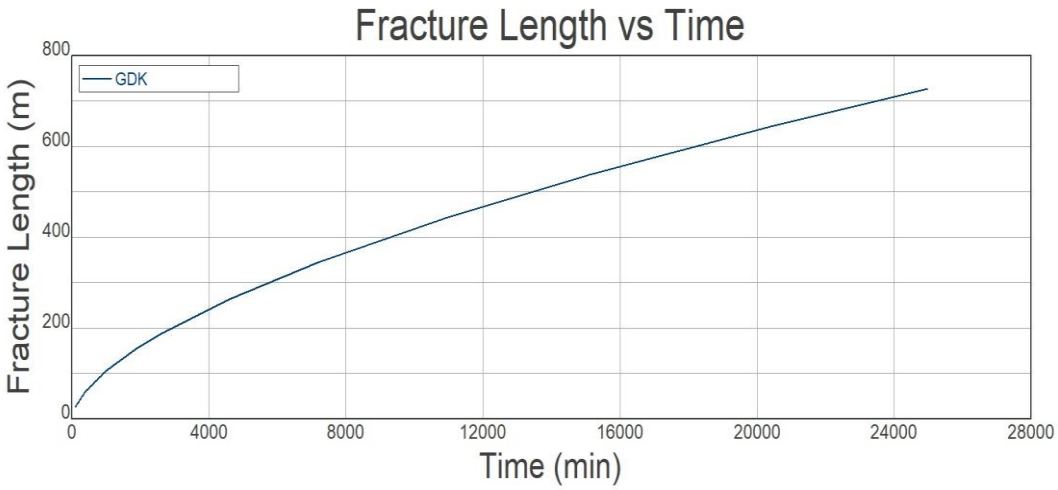


Figure 61. Fracture Length vs. Time Graph

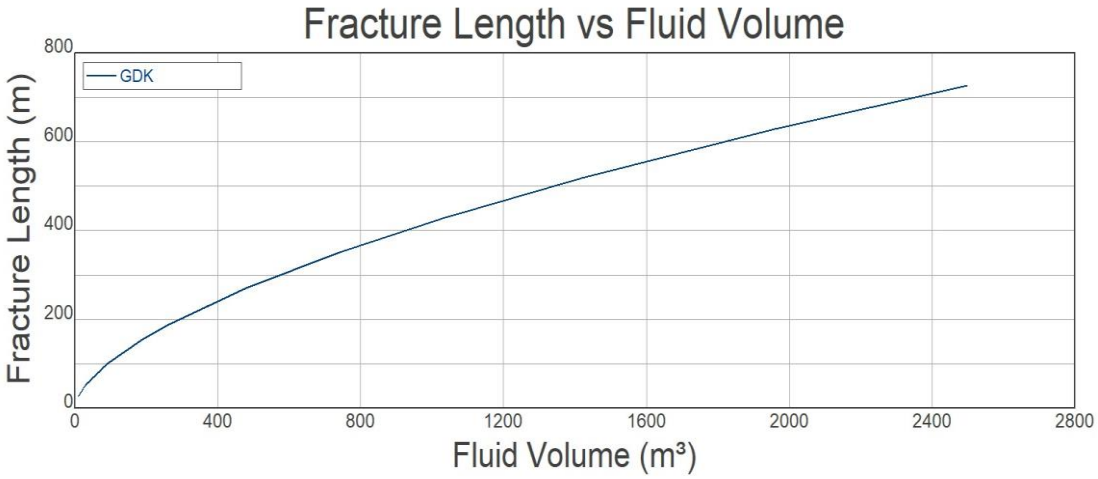


Figure 62. Fracture Length vs. Injected Volume

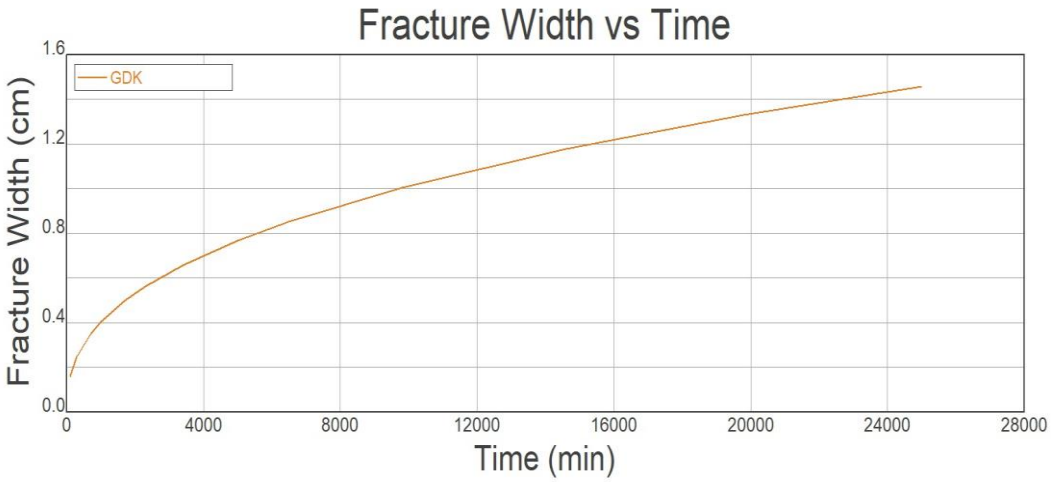


Figure 63. Fracture Width vs. Time Graph

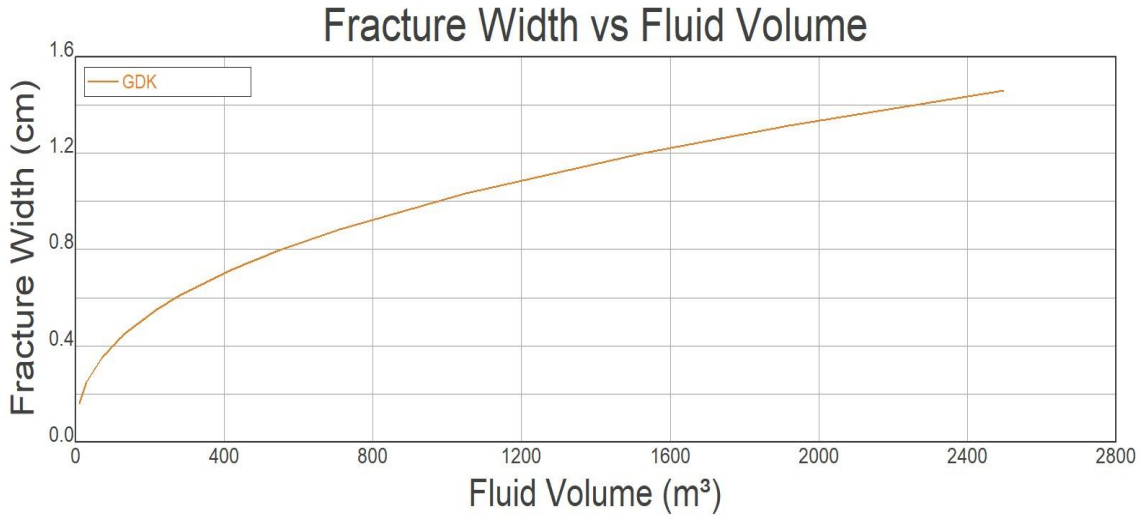


Figure 64. Fracture Width vs. Injected Volume

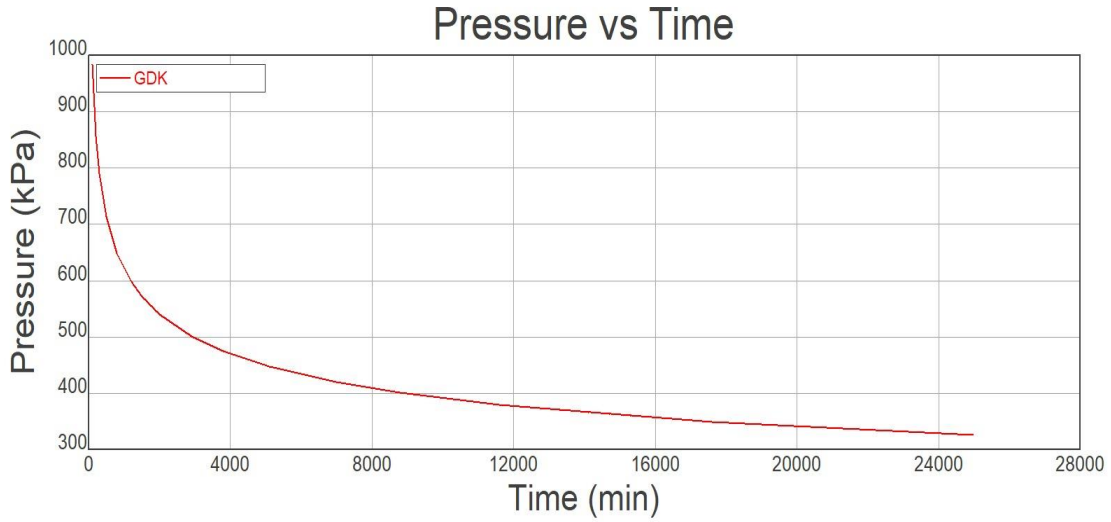


Figure 65. Pressure vs. Time

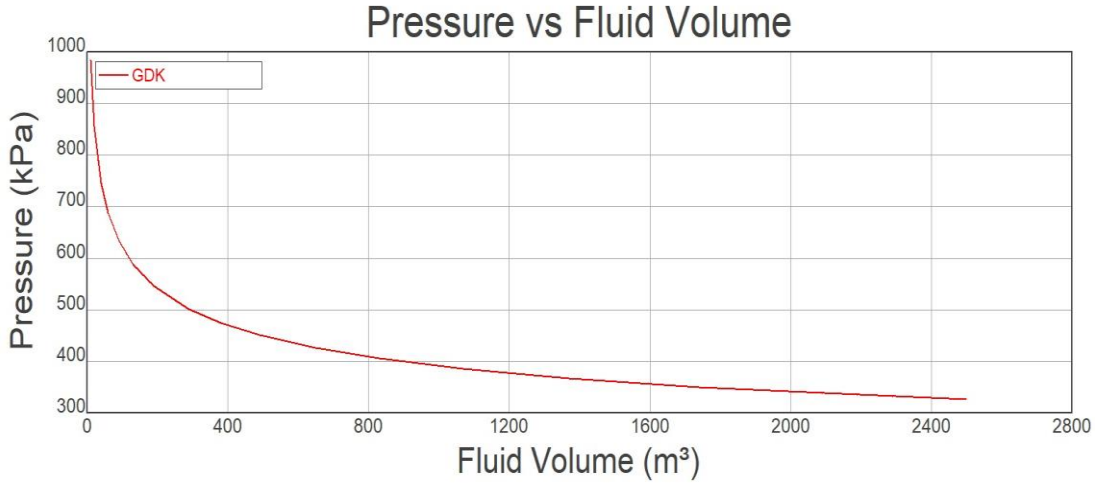


Figure 66. Pressure vs. Injected Volume

# 6. CONCLUSION AND RECOMMENDATIONS

## 6.1 Conclusion

This thesis has revealed that the energy need in our developing world increases day by day. It has been stated that there is a need for renewable energy sources to meet this increasing demand.

Enhanced geothermal systems are one of the technologies that are increasing in popularity among these renewable energy sources. Previous studies have proved the potential of this new geothermal energy. In addition, it was observed in the same studies that very comprehensive and multi-disciplinary research studies should be done for this technology to be successful due to complex designing parameters. It has been observed that irreversible problems were encountered in previous projects that were not studied in this way. For this aim, the potential enhanced geothermal reservoir on the southern flank of the Menderes Graben was investigated comprehensively and multi-disciplinary approach. The assessments have been carried out in three stages, the first of which was the literature research for the region. According to the literature study, it has been determined that the metamorphic rocks required for advanced geothermal systems are located in the studied region due to high tectonism. In addition, considering that tectonism is a factor that directly affects the underground temperature, it has been estimated that this region contains both suitable reservoir rock types and sufficient heat that are essential for an enhanced geothermal system. After the literature study, deep drilling data in the southern region were examined. According to the boring data, the metamorphic rocks (i.e., marble successions for this reservoir) required for advanced geothermal systems were observed between a depth of 3600-3750 meters. In addition, the temperature of the rock at these depths was measured at approximately 180 degrees. In the light of this literature and deep boring data, it was decided that this region is a suitable potential field for the enhanced geothermal system.

During the field studies, discontinuity and paleo-stress analyses were performed at the southern flank of the Menderes Massif. These analyses are essential for fracture direction prediction since hydraulic fracturing essentially acts according to its stress state. The dip

and dip directions were determined according to the discontinuity analysis based on scan-line survey studies. These results showed that two different pole plot orientations presenting the fault crack propagation mechanisms were observed along the East-West and North-South direction, consistent with the FMI deep borehole log data. In addition, paleo-stress studies confirm these two different extensional regimes in the region. Both East-West and North-South expansions were clearly observed in the field. As a result of field these investigations, it was inferred that the maximum principal stress was in the vertical direction, and the other two stresses were in the horizontal direction while their magnitude is close to each other. Apart from these field studies, the block samples were obtained from the marble units for rock mechanics laboratory testing to determine the mechanical properties of the representative rock samples. Static deformability, UCS, TCS, and Point load tests have been performed, and the required geomechanical parameters for hydraulic fracturing modeling were determined.

In the light of this information gathered, two-dimensional hydraulic fracturing analyzes were made with the Mfast software. Sensitivity analyses were done for undetermined parameters (i.e., proppant, pumping time). Stress aspects that directly affect the direction of hydraulic fracturing were determined based on these studies. All of the paleo-stress, scan-line survey and deep boring in-situ testing studies prove that maximum principal stress is at the vertical direction for the selected region. Also, intermediate and minimum stress magnitudes are very close. In this case, it has been identified that the artificially created cracks will be in the vertical direction. Thus, it is expected that the length of the crack in the vertical direction will be longer. According to 2D modeling and sensitivity results, one of the most critical parameters is the pumping time. It highly affects fracture length and width. Since fractures should open slowly due to short-circuit concerns, the fracture opening time was kept long in this study. Thus, fracture widths were kept around 1 cm. While doing this, a sufficient reservoir area has been reached at 726 m instead of 529 m. Although ceramic proppants are more expensive than others, they are preferred over sand proppants due to sustainability issues. Despite their high cost, ceramic proppants have been preferred considering the reservoir depth and the demand for conductivity in developed geothermal systems. Thus, it was considered that the life of the system's facility would be longer.

As a result of these characterization and modeling studies, it has been seen that the Aegean region is suitable for enhanced geothermal systems due to its tectonics and geological structure. Tectonism-wise, it is observed that the Aegean region has a relatively thin crust with an active faulting system. Fault systems were generally normal faulting, and extensional movement was observed in the Aegean region. These extensions were determined by paleo-stress and discontinuity studies and both N-S and E-W extensions observed at the field. Considering the depths and normal faulting mechanisms, it has been determined that the fracture directions will be vertical. Geological-wise, four different nappes were determined, and they contain primarily metamorphic rocks (marble, schist, gnays lithologies). It has been observed that the temperature value at the depths of these formations was 180-200 degrees Celsius which is sufficient for enhanced geothermal systems. All these data proved that the Aegean region is suitable for developed geothermal systems.

In addition to reservoir characterization, 2D pseudo modeling and sensitivity analyses were performed, and obtained results are stated below:

1. Although the Young's Modulus was determined as 50 GPa, sensitivity analysis was carried out to determine its effect on geometry. As a result of this analysis, the modulus of elasticity directly affects the fracture geometry. As Young's Modulus increases, fracture length will increase along with required net pressure while width decreases.
2. Poisson's ratio analysis shows that its effect is minimal on fractal matrix geometry.
3. Fracture toughness also has minimal effects on fracture geometry. However, since fracture toughness is a yield criterion, it is essential to determine its value.
4. For the fluid rheology-wise, it is observed that fluid parameters significantly affect the fracture geometry. Flow behavior index analyses were performed between 0.1 and 1. It is observed that shear thinning and thickening behavior is vital for fracture width and length. Since the fluidity of shear thickening fluids decreases with the shear effect. Thickened fluids affect the extension direction negatively while increasing the width of the fractures and can lead to short-circuiting; it has been observed that such fluids should be avoided due to decreasing reservoir volume.

As a result of all these characterizations and models, the study area was identified to be suitable for developed geothermal systems.

In the final modeling made in the light of the parameters obtained from the sensitivity analyses, laboratory studies, and field surveys, it was calculated that a reservoir with a length of 726 meters and a thickness of 1 cm dominated by vertical fractures would be formed.

### 6.2 Recommendations

Studies have shown that hydraulic fracturing can enhance conventional geothermal systems and help generate energy from hot dry rocks. While conventional geothermal systems require fluid, temperature, and permeability, advanced geothermal systems only require high temperature and a connected fractal matrix. However, extensive research is required for this procedure to determine reservoir characteristics and predict the propagation direction of the fractures. Requirements for reservoir characterization and crack direction determination for hydraulic fracturing are given below.

1. Deep drilling and imaging logs are essential for the geological assessment of the reservoir.
2. These imaging tools should determine Paleo-stresses and fracture directions since hydraulic fracture propagates perpendicular to minimum principal stress.
3. The rocks in the designated reservoir should have high heat conduction and heat capacity.
4. Microseismic devices should be used for fracture direction determination during the hydraulic fracturing process.
5. Production wells should be drilled according to microseismic measurements and flow backtests. It has been seen in previous studies that there may be problems in the connections of pre-drilled production wells.
6. Hydraulic fracturing is an irreversible operation. Therefore, the cracking process should be carried out in a controlled manner. Cracks that are larger than necessary affect the heat exchange negatively.
7. In addition, the probability of short circuit increases in high-speed cracking. Thus, fracturing operations must be done slow and steadily.
8. On the other hand, minor fractures can cause connectivity problems.
9. Sensitivity analyses should be made in the laboratory to use the cracking fluid.

10. Proppant selection should be performed carefully. Although the fracturing process is successful, the life of the production depends on the proppant type and its geometry.

Although this study can meet most of the above clauses, it might have shortcomings. Future studies need to be done for more precise modeling. First, fracturing fluids are materials whose properties can be determined in the laboratory environment. Determining the character of the fracture fluid will give more precise results for the crack geometry. Also, since leakage coefficients of the reservoir will directly affect the efficiency of the cracking operation, flow-back tests are required to obtain these coefficients. In addition to the studies carried out, mini fracture treatments need to calibrate the fracture model input data and redesign the treatment if necessary. With these studies, it will be possible to switch from 2D pseudo models to 3D models.

# REFERENCES


Abdel Hafeez, T., Abdelwahhab, M., & Elmahdy, M. (2019). Geothermal application of spectral gamma-ray logging in the South Kansas Subsurface, USA. Applied Radiation and Isotopes, 154(July), 108904. https://doi.org/10.1016/j.apradiso.2019.108904

Akgün, H. (2021). Investigation of the Fracture Network Enhancement Mechanism and the Parameters Through Hydro-Mechanical Modelling with the Incorporation of the Geomechanical Properties of the Menderes Massif Marble unit and the In-Situ Principal Stresses, 1st Progress Report, TUBİTAK 1001 Project No:119Y535, Ankara, 37p

Altay, F., Çalapkulul, F., Tavman, İ.H. (2001). Bazı Türk Doğal Taşlarının Isı İletim Katsayıları. *4. Endüstriyel Hammaddeler Sempozyumu*, DEÜ, İzmir, 18-19 Ekim, 308-315.

Anderson, E.M. (1951). The Dynamics of Faulting and Dyke Formation with Application to Britain. 2nd ed. Oliver and Boyd, Edinburgh.

Angelier, J. (1990). Inversion of field data in fault tectonics to obtain the regional stress—III. A new rapid direct inversion method by analytical means. Geophysical Journal International, 103(2), 363-376.

Angelier, J. (2007). Inversion of field data in fault tectonics to obtain the regional stress - III. A new rapid direct inversion method by analytical means. Geophysical Journal International. 103. 363 - 376. 10.1111/j.1365-246X.1990.tb01777.x

Basel, E.D.K., Serpen, U. And Satman, A. (2009). Assessment of Turkey Geothermal Resources. 34th Workshop on Geothermal Reservoir Engineering, Standford, California

Bearman, R. A. (1999). The use of the point load test for the rapid estimation of Mode I fracture toughness. *International Journal of Rock Mechanics and Mining Sciences*, *36*(2), 257–263. https://doi.org/10.1016/S0148-9062(99)00015-7

Béatrice, A. L., Hébert, R. L. (2012). The Soultz-sous-Forêts' Enhanced Geothermal System: A Granitic Basement Used as a Heat Exchanger to Produce Electricity. Heat

Exchangers - Basics Design Applications. doi:10.5772/34276

Bott, M. H. P. (1959). The mechanics of oblique-slip faulting. Geological Magazine, 96(2), 109-117

Boyun, G., Xinghui, L., Xuehao, T. (2017). *Petroleum Production Engineering*. https://doi.org/10.1016/B978-0-12-809374-0.00014-3

Bozkurt, E., Park, R.G. (1994). Southern Menderes Massif: an incipient metamorphic core complex in western Anatolia, Turkey. J. Geol. Soc. Lond. 151, 213–216.

Bozkurt E, Oberhänsli, R. (2001). Menderes Massif (Western Turkey). Structural, metamorphic and magmatic evolution - a synthesis. International Journal of Earth Sciences 89: 679-708. doi: 10.1007/s005310000173

Brudy, M., & Zoback, M. (1999). Drilling-induced tensile wall-fractures: implications for determination of in-situ stress orientation and magnitude. *International Journal of Rock Mechanics and Mining Sciences*, *36*(2), 191–215. https://doi.org/10.1016/S0148-9062(98)00182-X

Burg, J.P. (2013). Structural Geology: Tectonic Systems. ETH Zurich and the University of Zurich.

Cáchová, M., Koňáková, D., Vejmelková, E., Keppert, M., & Cerný, R. (2016). Mechanical and thermal properties of the Czech marbles. *AIP Conference Proceedings*, *1738*(June 2016). https://doi.org/10.1063/1.4952070

Carey, E., ve Brunier, B. (1974). Analyse théorique et numérique d'un modéle mécanique élémentaire Paleostress fields in the Tokai district'141 appliqué a l'étude d'une population de failles. C. r. Acad. Sci, Paris, Ser. D, 279(8917894), 51-65

Coates G R, Denoo S.A. (1981). Mechanical properties program using borehole analysis and Mohr's circle. In: Proceedings of the SPWLA 22nd Annual Logging Symposium. Houston: SPWLA, 1981.

Cremer et al. (1980). G.M. Cremer, M.C. Duffield, M.G. Smith Hot Dry rock geothermal energy development program Annual Report, Fiscal Year 1979, LA-8280-HDR, Los Alamos National Laboratory, Los Alamos, NM, USA.

Delvaux, D., ve Sperner, B. (2003). New aspects of tectonic stress inversion with reference to the TENSOR program. Geological Society, London, Special Publications, 212(1), 75-100.

Dewey, J. F., & ŞengörR, A. M. Cel. (1979). Aegean and surrounding regions: Complex multiplate and continuum tectonics in a convergent zone. GSA Bulletin, 90(1), 84–92. https://doi.org/10.1130/0016-7606

Do You Know the Different Types of Faults? (2020, January 17). ThoughtCo. https://www.thoughtco.com/fault-types-with-diagrams-3879102

Durmuş, G., Görhan, G. (2009). Doğal taş plakalarin isil iletkenlik bakimdan termografik görüntülerinin incelenmesi. Selçuk Teknik Degisi, 8 (1), 48-57.

Economides, M. J., & Nolte, K. G. (2000). *Reservoir Stimulation, 3rd Edition* (3rd ed.). Wiley.

Engelder, T., and Geiser, P. (1980). On the use of regional joint sets as trajectories of paleo-stress fields during the development of the Appalachian Plateau, New York, *J. Geophys. Res.*, 85( B11), 6319– 6341, doi:10.1029/JB085iB11p06319.

Engelder, T. (1985). Loading paths to joint propagation during a tectonic cycle: an example from the Appalachian Plateau, U.S.A. *Journal of Structural Geology*, *7*(3–4), 459–476. https://doi.org/10.1016/0191-8141(85)90049-5

EPDK, 2012. Elektrik piyasası raporu, 55p.

Forbes Inskip, N. D., Meredith, P. G., Chandler, M. R., & Gudmundsson, A. (2018). Fracture properties of Nash Point shale as a function of orientation to bedding. Journal of Geophysical. Research: Solid Earth, 123, 8428–8444. https://doi.org/10.1029/2018JB015943

Gautier, P., Brun, J.-P., Moriceau, R., Sokoutis, D., Martinod, J., Jolivet, L. (1999). Timing, kinematics and cause of Aegean extension: a scenario based on a comparison with simple analogue experiments. Tectonophysics 315, 31–72

Genter, A., Goerke, X., Graff, J.-J., Cuenot, N., Krall, G., Schindler, M., & Ravier, G. (2010). Current Status of the EGS Soultz Geothermal Project (France). *World Geothermal Congress 2010*, *April*, 6.

Gérard, A., Genter, A., Kohl, T., Lutz, P., Rose, P., & Rummel, F. (2006). The deep EGS (Enhanced Geothermal System) project at Soultz-sous-Forêts (Alsace, France). *Geothermics*, *35*(5–6), 473–483. https://doi.org/10.1016/j.geothermics.2006.12.001

Gessner, K., Piazolo, S., Güngör, T., Ring, U., Kröner, A., Passchier, C.W. (2001a). Tectonic significance of deformation patterns in granitoid rocks of the Menderes nappes, Anatolide belt, southwest Turkey. International Journal of Earth Sciences

89: 766-780. doi: 10.1007/s005310000106

Gessner, K., Ring, U., Passchier, C.W., and Güngör, T. (2001b). How to resist subduction: Evidence for largescale out-of-sequence thrusting during Eocene collision in western Turkey: Journal of the Geological Society, London, 158, 769–784. doi:10.1144/jgs.158.5.769

Ghasemi, A., & Alexis, D. A. (2010). Feasibility and Design of Engineered Geothermal Systems using Dry Holes as a Prospective Location. *Ppt*, *May*, 45.

Griffith, A.A. (1921). The phenomena of rupture and flow in solids. Phil. Trans. Roy. Soc. 221, 163-198.

Griffith, A.A. (1924). The theory of rupture. In: Proceeding of the 1st International Congress for Applied Mechanics, Delft, Netherlands, pp. 55-63

Gunsallus, K.L., Kulhawy, F.H. (1984). A comparative evaluation of rock strength measures. Int J Rock Mech Min Sci and Geomech Abstr. 24(5), 233-248.

Gürer ÖF, Sarica-Filoreau N, Özburan M, Sangu E, Dogan, B. (2009). Progressive development of the Büyük Menderes Graben is based on new data, western Turkey. Geological Magazine 146: 652-673. doi: 10.1017/S0016756809006359

Hancock, P., Al-Khatieb, S., & Al-Kadhi, A. (1981). Structural and photogeological evidence for the boundaries to an East Arabian block. *Geological Magazine*, *118*(5), 533-538. doi:10.1017/S0016756800032891

Healy, J. H., & Zoback, M. D. (1988). Hydraulic fracturing in situ stress measurements to 2.1 km depth at Cajon Pass, California. *Geophysical Research Letters*, *15*(9), 1005–1008. https://doi.org/10.1029/gl015i009p01005

Holm, A., Blodgett, L., Jennejohn, D., Gawell, K. (2010). Geothermal Energy: International Market Update. Washington, DC: Geothermal Energy Association. Accessed: http://www.geoenergy.org/pdf/reports/gea_international_market_report_final_may_2010.pdf

Hori, Y., Kitano, K., Kaieda, H., & Kiho, K. (1999). Present status of the Ogachi HDR project, Japan, and future plans. *Geothermics*, *28* (4–5), 637–645. https://doi.org/10.1016/S0375-6505(99)00034-6

Hubbert, M.K. and Willis, D.G. (1957). Mechanics of Hydraulic Fracturing. Transactions of Society of Petroleum Engineers of AIME, 210, 153-163

Hudson, J.A., Harrison, J.P. (1997). Engineering Rock Mechanics. An Introduction to the Principles. Pergamon, Oxford, 444 p

IEA (2011). Technology Roadmap: Geothermal Heat and Power. In: Agency, I.E. (Ed.). International Energy Agency, Paris, France, 52pp.

Irwin, G. (1957). Analysis of stresses and strains near the end of a crack traversing a plate. J. Appl. Mech. 24, 361?364.

ISRM Testing Commission (Ouchterlony, F. Co-ordinator) (1988): Suggested methods for determining the fracture toughness of rock. Int. J. Rock Mech. Min. Sci. Geomech. Abstr. 25, 71–96.

Jeotermal Enerji Kurumu. (2017). Geothermal: International market overview report, Washington D.C., USA, 26p

Jolivet, L., Brun, J.-P. (2010). Cenozoic geodynamic evolution of the Aegean. Int. J. Earth Sci. 99, 109–138

Kaygusuz, K., Kaygusuz, A. (2004). Geothermal energy in Turkey: The Sustainable future. Renewable and Sustainable Energy Reviews, 8: 545- 563.

Khoshbakht, F., Memarian, H., & Mohammadnia, M. (2009). Comparison of Asmari, Pabdeh and Gurpi formation's fractures, derived from image log. *Journal of Petroleum Science and Engineering*, *67*(1–2), 65–74. https://doi.org/10.1016/j.petrol.2009.02.011

Lally, M. (2011). U.S. Companies See Growth Potential in Turkey. Retrieved August 29, 2016, from http://www.renewableenergyworld.com/articles/2011/08/u-s-companies-see-growthpotential-in-turkey.html.

Lei, Z., Zhang, Y., Zhang, S., Fu, L., Hu, Z., Yu, Z., Li, L., & Zhou, J. (2020). Electricity generation from a three-horizontal-well enhanced geothermal system in the Qiabuqia geothermal field, China: Slickwater fracturing treatments for different reservoir scenarios. *Renewable Energy*, *145*, 65–83. https://doi.org/10.1016/j.renene.2019.06.024

Macdonald, P., Stedman, A., Symons, G., & Ora, O. O. X. (1992). The UK Geothermal Hot Dry Rock R & D Programme. *17th Workshop on Geothermal Reservoir Engineering*, 5–11.

Maleki, S., Moradzadeh, A., Riabi, R. G., Gholami, R., & Sadeghzadeh, F. (2014). Prediction of shear wave velocity using empirical correlations and artificial

intelligence methods. *NRIAG Journal of Astronomy and Geophysics*, *3*(1), 70–81. https://doi.org/10.1016/j.nrjag.2014.05.001

Matsunaga, I., Niitsuma, H., & Oikawa, Y. (2005). Review of the HDR Development at Hijiori Site, Japan. *Proceedings of the World Geothermal Congress 2005, April*, 1–5. http://www.geothermal-energy.org/pdf/IGAstandard/WGC/2005/1635.pdf5

Mao, R., Feng, Z., Liu, Z., & Zhao, Y. (2017). Laboratory hydraulic fracturing test on large-scale pre-cracked granite specimens. *Journal of Natural Gas Science and Engineering*, *44*, 278–286. https://doi.org/10.1016/j.jngse.2017.03.037

Montgomery C.T., Smith M.B., Technologies N.S.I., Fracturing H., Cooke C.E., Dollarhide F.E., Elbel J.L., Fast C.R., Hannah R., Harrington L.J., Perkins T.K., Prats M., Van Poollen H.K. (2010). Hydraulic fracturing, history of an enduring technology, J. Pet. Technol, 26–41.

Moska, R., Labus, K., & Kasza, P. (2021). Hydraulic Fracturing in Enhanced Geothermal Systems—Field, Tectonic and Rock Mechanics Conditions—A Review. *Energies*, *14*(18), 5725. https://doi.org/10.3390/en14185725

Norbeck, J. H., McClure, M. W., & Horne, R. N. (2018). Field observations at the Fenton Hill enhanced geothermal system test site support mixed-mechanism stimulation. *Geothermics*, *74* (December 2017), 135–149. https://doi.org/10.1016/j.geothermics.2018.03.003

Nordgren, R. (1972). Propagation of a Vertical Hydraulic Fracture. *Society of Petroleum Engineers Journal*, *12*(04), 306–314. https://doi.org/10.2118/3009-pa

Nguyen, H. T., Lee, J. H., & Elraies, K. A. (2020). A review of PKN-type modeling of hydraulic fractures. *Journal of Petroleum Science and Engineering*, *195*, 107607. https://doi.org/10.1016/j.petrol.2020.107607

Niu, J., Fu, C., & Tan, W. (2012). Slip-Flow and Heat Transfer of a Non-Newtonian Nanofluid in a Microtube. *PLoS ONE*, *7*(5), e37274. https://doi.org/10.1371/journal.pone.0037274

Osarogiagbon, A. U., Oloruntobi, O., Khan, F., Venkatesan, R., & Butt, S. (2020). Gamma-ray log generation from drilling parameters using deep learning. *Journal of Petroleum Science and Engineering*, *195*(September), 107906. https://doi.org/10.1016/j.petrol.2020.107906

Oyler, D. C., Mark, C., & Molinda, G. M. (2010). In situ estimation of roof rock strength

using sonic logging. *International Journal of Coal Geology*, *83*(4), 484–490. https://doi.org/10.1016/j.coal.2010.07.002

Özer, S., Sözbilir, H. (2003). Presence and tectonic significance of Cretaceous rudist species in the so-called Permo-Carboniferous Göktepe Formation, central Menderes metamorphic Massif, western Turkey. International Journal of Earth Sciences 92: 397- 404. doi: 10.1007/s00531-003-0333-z

Paleo-"Stress" Analysis From Fault Data. (2017). Paleostress calculation, 155-175. https://www.files.ethz.ch/structuralgeology/jpb/files/english/5paleostress.pdf

Parsons, C.P. (1943). Caliper Logging. *Transactions of the AIME*, *151*(01), 35–47. https://doi.org/10.2118/943035-G

Potter, R. M., Smith, M. C., and Robinson, E.S. (1974). "Method of extracting heat from dry geothermal reservoirs," U. S. patent No. 3,786,858.

Qiu K., Chen M., Jin Y. (2011). Stability model of borehole wall during the well test after acidizing treatment of sandstone reservoirs. Petroleum Exploration and Development, 38(5): 589–593.

Rajabi, M., Sherkati, S., Bohloli, B., & Tingay, M. (2010). Subsurface fracture analysis and determination of in-situ stress direction using FMI logs: An example from the Santonian carbonates (Ilam Formation) in the Abadan Plain, Iran. *Tectonophysics*, *492*(1–4), 192–200. https://doi.org/10.1016/j.tecto.2010.06.014

Régnier, J. L., Ring, U., Passchier, C. W., Gessner, K., & Güngör, T. (2003). Contrasting metamorphic evolution of metasedimentary rocks from the Çine and Selimiye nappes in the Anatolide belt, western Turkey. *Journal of Metamorphic Geology*, *21*(7), 699–721. https://doi.org/10.1046/j.1525-1314.2003.00473.x

Reilinger, R., McClusky, S., Vernant, P., Lawrence, S., Ergintav, S. (2006). GPS constraints on continental deformation in the Africa-Arabia-Eurasia continental collision zone and implications for the dynamics of plate interactions. Journal of Geophysical Research 111: 1-26. doi: 10.1016/j.epsl.2013.10.018

Richter, A. (2018). The U.S. Department of Energy has announced funding of $4.45 million for early stage development of enhanced geothermal systems (EGS) tools and technologies. Think Geoenergy. https://www.thinkgeoenergy.com/u-s-doe-announces-4-45m-funding-for-enhanced-geothermal-systems-egs-tools-technologies/

Ring, U., Glodny, J., Will, T., Thomson, S.N. (2010). The Hellenic subduction system: high-pressure metamorphism, exhumation, normal faulting, and large-scale extension. Annu. Rev. Earth Planet. Sci. 38, 45–76.

Ring, U., Johnson, C., Hetzel, R., Gessner, K. (2003). Tectonic denudation of a Late Cretaceous–Tertiary collisional belt: regionally symmetric cooling patterns and their relation to extensional faults in the Anatolide belt of western Turkey. Geol. Mag. 140 (4), 421–441.

Rountree, C. L., Kalia, R. K., Lidorikis, E., Nakano, A., Van Brutzel, L., & Vashishta, P. (2002). Atomistic aspects of crack propagation in brittle materials: Multimillion atom molecular dynamics simulations. *Annual Review of Materials Science*, *32*, 377–400. https://doi.org/10.1146/annurev.matsci.32.111201.142017

Sacramento, R. N., Yang, Y., You, Z., Waldmann, A., Martins, A. L., Vaz, A. S. L., Zitha, P. L. J., & Bedrikovetsky, P. (2015). Journal of Petroleum Science and Engineering Deep bed and cake fi ltration of two-size particle suspension in porous media. *Journal of Petroleum Science and Engineering*, *126*, 201–210. https://doi.org/10.1016/j.petrol.2014.12.001

Sanyal, S.K., Butler, S.J. (2005). An analysis of power generation Prospects from enhanced geothermal systems. Geothermal Resources Council Transactions 29.

Sneddon, I. N., & Elliot, H. A. (1946). The opening of a Griffith crack under internal pressure. *Quarterly of Applied Mathematics*, *4*(3), 262–267. https://doi.org/10.1090/qam/17161.

Siefert, D., Wolfgramm, M., Kölbel, T., Glodny, J., Kolb, J., & Eiche, E. (2021). Geothermal reservoir rocks of the Büyük Menderes Graben (Turkey): stratigraphic correlation by a multiproxy approach. Turkish Journal of Earth Sciences, 30(SI-2), 1008–1031. https://doi.org/10.3906/yer-2104-11

Sorkhabi, R., (2015). *Know Your Faults! Part II. GEO ExPro*. https://www.geoexpro.com/articles/2013/06/know-your-faults-part-ii

Sözbilir, H. (2020). The West Anatolian Regional Geology, Seismicity and the Relationship with Geothermal Resources. *MoEU-EBRD Geothermal Final Cia Report*, 450-525.

Şengör, A.M.Ç., Satır, M., Akkök, R. (1984). Timing of tectonic events in the Menderes Massif, Western Turkey: implications for tectonic evolution and evidence for Pan-

African basement in Turkey. Tectonics 3, 697–707

Şengör, A.M.C. (1987). Cross-faults and differential stretching of hanging walls in regions of low-angle normal faulting: Examples from western Turkey. Geological Society Special Publication, 28(28), 575–589. https://doi.org/10.1144/GSL.SP.1987.028.01.38

Şimşek, Ş. (1985). Geothermal model of Denizli, Sarayköy-Buldan area. *Geothermics*, *14*(2–3), 393–417. https://doi.org/10.1016/0375-6505(85)90078-1

Tenzer, H., Park, C. H., Kolditz, O., & McDermott, C. I. (2010). Application of the geomechanical facies approach and comparison of exploration and evaluation methods used at Soultz-sous-Forêts (France) and Spa Urach (Germany) geothermal sites. *Environmental Earth Sciences*, *61*(4), 853–880. https://doi.org/10.1007/s12665-009-0403-z

Testa, S. M. (2017). Historic Development of Well Stimulation and Hydraulic Fracturing Technologies. *AAPG Pacific Section and Rocky Mountain Section Joint Meeting*, *60053*(60053), 1–46.

Tester, J.W., Smith, M.C. (1977). Energy Extraction Characteristics of Hot Dry Rock Geothermal Systems. Proceedings of the Twelfth Intersociety Energy Conversion Engineering Conference, Washington, D.C. American Nuclear Society, 1:816.

Roberts, Edward A.L. (1866). Improvement of the method of increasing the capacity of oil-wells. US patent 59936.

van Hinsbergen, D.J.J., Hafkenscheid, E., Spakman, W., Meulenkamp, J.E., Wortel, M.J.R. (2005). Nappe stacking resulting from subduction of oceanic and continental lithosphere below Greece. Geology 33 (4), 325–328

van Hinsbergen, D.J.J., Kaymakci, N., Spakman, W., Torsvik, T.H. (2010). Reconciling the geological history of western Turkey with plate circuits and mantle tomography. Earth and Planetary Science Letters 297: 674-686. doi: 10.1016/j.epsl.2010.07.024

Wallace, R.E. (1951). Geometry of shearing stress and relation to faulting. The Journal of geology, 59(2), 118-130.

Wang, H.Y. (2019). Hydraulic fracture propagation in naturally fractured reservoirs: Complex fracture or fracture networks. *Journal of Natural Gas Science and Engineering*, *68*(2010). https://doi.org/10.1016/j.jngse.2019.102911

Williams, B.B., Gidley, J.L. and Schechter, R.S. (1979). Acidizing Fundamentals, Richardson, Texas, USA, Society of Petroleum Engineers.

Xie, L., Min, K. B., & Song, Y. (2015). Observations of hydraulic stimulations in seven enhanced geothermal system projects. *Renewable Energy*, *79*(1), 56–65. https://doi.org/10.1016/j.renene.2014.07.044

Yan J., Cai J., Zhao M. (2011). Application of electrical image logging in the study of sedimentary characteristics of sandy conglomerates. Petroleum Exploration and Development, 38(4): 444–451.

Yew, C. H. (1997). Mechanics of hydraulic fracturing. *Mechanics of Hydraulic Fracture*, *210*. https://doi.org/10.2118/686-g

Yin, Z. M., Ranalli, G. (1993). Determination of tectonic stress field from fault slip data: toward a probabilistic model. Journal of Geophysical Research: Solid Earth, 98(B7), 12165-12176

Zendehboudi S., Bahadori, A. (2017). *Exploration and Drilling in Shale Gas and Oil Reserves*. https://doi.org/10.1016/B978-0-12-802100-2.00003-4

Zhang, H., Wan, Z., & Elsworth, D. (2020). Failure Behavior of Hot-Dry-Rock (HDR) in Enhanced Geothermal Systems: Macro to Micro Scale Effects. *Geofluids*, *2020*, 1–13. https://doi.org/10.1155/2020/8878179

Zhang, L. (2017). Rock Discontinuities. *Engineering Properties of Rocks*, 81–136. https://doi.org/10.1016/b978-0-12-802833-9.00004-3

Zimmermann, G., Moeck, I., & Blöcher, G. (2010). Cyclic waterfrac stimulation to develop an Enhanced Geothermal System (EGS)—Conceptual design and experimental results. *Geothermics*, *39*(1), 59–69. https://doi.org/10.1016/j.geothermics.2009.10.003

# APPENDIX A

Scan-Line Survey results from the field studies

| Location | Dip | Dip Direction | Color | Spacing (mm) | Persistence (m) | Filling | Aperture (mm) | Roughness | Degradation Degree |
|---|---|---|---|---|---|---|---|---|---|
| South flank of Menderes Massif | 84 | 330 | Light Grey | 40 | 2 | - | 1 | undulating smooth | slightly degraded |
| | 84 | 332 | Light Grey | 70 | 2.5 | - | 5 | undulating smooth | slightly degraded |
| | 85 | 337 | Light Grey | 120 | 3 | - | 4 | undulating smooth | slightly degraded |
| | 83 | 335 | Light Grey | 300 | 5 | - | 1 | undulating rough | slightly degraded |
| | 85 | 331 | Light Grey | 250 | 4 | - | 2 | undulating rough | slightly degraded |
| | 82 | 333 | Light Grey | 160 | 6 | - | 3 | undulating rough | slightly degraded |
| | 84 | 318 | Light Grey | 60 | 2 | - | 3 | undulating rough | slightly degraded |
| | 25 | 235 | Light Grey | 100 | 1 | - | 8 | undulating smooth | slightly degraded |
| | 28 | 240 | Light Grey | 230 | 5 | - | 10 | undulating rough | slightly degraded |
| | 44 | 244 | Light Grey | 340 | 2 | - | 1 | undulating rough | slightly degraded |
| | 42 | 244 | Light Grey | 400 | 4 | - | 5 | undulating smooth | slightly degraded |
| | 45 | 254 | Light Grey | 170 | 3 | - | 3 | undulating smooth | slightly degraded |
| | 35 | 235 | Light Grey | 200 | 2 | - | 4 | undulating smooth | slightly degraded |
| | 50 | 65 | Light Grey | 100 | 8 | calcite | 10 | undulating smooth | slightly degraded |
| | 52 | 65 | Light Grey | 250 | 10 | calcite | 4 | undulating smooth | slightly degraded |
| | 55 | 64 | Light Grey | 1000 | 9 | calcite | 5 | undulating rough | slightly degraded |
| | 53 | 66 | Light Grey | 830 | 7 | calcite | 8 | undulating rough | slightly degraded |
| | 50 | 61 | Light Grey | 920 | 8 | calcite | 10 | undulating smooth | slightly degraded |
| | 35 | 250 | Light Grey | 750 | 7.5 | calcite | 25 | undulating smooth | slightly degraded |
| | 32 | 248 | Light Grey | 460 | 9 | calcite | 12 | undulating smooth | slightly degraded |
| | 35 | 250 | Light Grey | 300 | 10 | calcite | 30 | undulating rough | slightly degraded |
| | 75 | 13 | Light Grey | 240 | 8 | calcite | 9 | undulating smooth | slightly degraded |
| | 77 | 18 | Light Grey | 120 | 7 | calcite | 7 | undulating rough | slightly degraded |
| | 79 | 13 | Light Grey | 260 | 10 | calcite | 5 | undulating rough | slightly degraded |
| | 75 | 15 | Light Grey | 330 | 8 | calcite | 3 | undulating rough | slightly degraded |
| | 77 | 7 | Light Grey | 850 | 10 | calcite | 2 | undulating smooth | slightly degraded |
| | 80 | 7 | Light Grey | 800 | 9 | calcite | 2 | undulating smooth | slightly degraded |
| | 79 | 6 | Light Grey | 900 | 8 | calcite | 1 | undulating rough | slightly degraded |
| | 76 | 8 | Light Grey | 1000 | 10 | calcite | 8 | undulating smooth | slightly degraded |
| | 77 | 5 | Light Grey | 740 | 8 | calcite | 10 | undulating smooth | slightly degraded |
| | 78 | 7 | Light Grey | 860 | 7.5 | calcite | 12 | undulating smooth | slightly degraded |
| | 65 | 85 | Light Grey | 1100 | 7 | calcite | 20 | undulating rough | slightly degraded |
| | 63 | 87 | Light Grey | 900 | 7.5 | calcite | 16 | undulating rough | slightly degraded |
| | 66 | 85 | Light Grey | 930 | 8 | calcite | 6 | undulating rough | slightly degraded |
| | 67 | 82 | Light Grey | 850 | 10 | calcite | 8 | undulating smooth | slightly degraded |
| | 65 | 84 | Light Grey | 830 | 9 | calcite | 3 | undulating smooth | slightly degraded |
| | 65 | 85 | Light Grey | 800 | 8 | calcite | 1 | undulating smooth | slightly degraded |
| | 25 | 272 | Light Grey | 700 | 8 | calcite | 1 | undulating rough | slightly degraded |
| | 25 | 271 | Light Grey | 750 | 10 | calcite | 4 | undulating smooth | slightly degraded |
| | 28 | 272 | Light Grey | 1500 | 9 | calcite | 9 | undulating smooth | slightly degraded |
| | 30 | 273 | Light Grey | 820 | 8 | calcite | 10 | undulating rough | slightly degraded |
| | 26 | 270 | Light Grey | 710 | 7 | calcite | 4 | undulating rough | slightly degraded |

# APPENDIX B

Point Load Testing Results;

| | | | | | | Diametrica | Axial | | | Diametrica | Axial | Diametrica | Axial | Diametrical | Axial | Diametrica | Axial | Diametrica | Axial | Axial $K_{ic}$(MN/$m^{1/2}$) |
|---|---|---|---|---|---|---|---|---|---|---|---|---|---|---|---|---|---|---|---|---|
| Sample | D_mm | L_mm | w1 | w2 | W_mm | De2_mm2 | De2_mm2 | P_kg | P_N | Is_Mpa | Is_Mpa | F | F | Is(50)_Mpa | Is(50)_Mpa | k | k | sc_Mpa | sc_Mpa | $K_c$(MN/$m^{1/2}$) |
| 1 | 29 | 21 | 41 | 41.5 | 41.25 | 841 | 1523.11 | 452.65 | 4439.02 | 5.28 | 2.91 | 0.78 | 0.89 | 4.13 | 2.61 | 19.33 | 21.03 | 79.85 | 54.84 | 0.54 |
| 2 | 30.5 | 22.25 | 42 | 42 | 42 | 930.25 | 1631.02 | 1105.72 | 10843.40 | 11.66 | 6.65 | 0.80 | 0.91 | 9.33 | 6.04 | 19.585 | 21.27 | 182.76 | 128.43 | 1.26 |
| 3 | 30.5 | 22.25 | 42 | 43 | 42.5 | 930.25 | 1650.44 | 1230.11 | 12063.28 | 12.97 | 7.31 | 0.80 | 0.91 | 10.38 | 6.66 | 19.585 | 21.31 | 203.32 | 141.84 | 1.39 |
| 4 | 26 | 20.75 | 37 | 31 | 34 | 676 | 1125.54 | 513.70 | 5037.66 | 7.45 | 4.48 | 0.75 | 0.84 | 5.55 | 3.74 | 18.82 | 20.10 | 104.50 | 75.19 | 0.78 |
| 5 | 30 | 21.5 | 42.5 | 42 | 42.25 | 900 | 1613.83 | INVALID TEST | | | | | | | | | | | | |
| 6 | 28 | 21.5 | 33 | 33 | 33 | 784 | 1176.47 | 463.02 | 4540.67 | 5.79 | 3.86 | 0.77 | 0.84 | 4.46 | 3.26 | 19.16 | 20.23 | 85.48 | 65.90 | 0.68 |
| 7 | 28.5 | 22.5 | 36 | 35.5 | 35.75 | 812.25 | 1297.27 | 987.08 | 9679.99 | 11.92 | 7.46 | 0.78 | 0.86 | 9.25 | 6.44 | 19.245 | 20.52 | 178.09 | 132.12 | 1.35 |
| 8 | 28.5 | 21 | 39 | 39 | 39 | 812.25 | 1415.21 | 917.98 | 9002.28 | 11.08 | 6.36 | 0.78 | 0.88 | 8.61 | 5.60 | 19.245 | 20.80 | 165.62 | 116.38 | 1.17 |
| 9 | 29 | 21.5 | 40 | 39 | 39.5 | 841 | 1458.50 | 731.39 | 7172.46 | 8.53 | 4.92 | 0.78 | 0.89 | 6.67 | 4.36 | 19.33 | 20.89 | 129.02 | 91.01 | 0.91 |
| 10 | 27.5 | 21.75 | 43 | 41 | 42 | 756.25 | 1470.59 | 537.89 | 5274.86 | 6.98 | 3.59 | 0.76 | 0.89 | 5.33 | 3.18 | 19.075 | 20.92 | 101.67 | 66.59 | 0.67 |
| 11 | 28.5 | 21 | 39 | 38 | 38.5 | 812.25 | 1397.06 | 634.64 | 6223.66 | 7.66 | 4.45 | 0.78 | 0.88 | 5.95 | 3.91 | 19.245 | 20.75 | 114.50 | 81.11 | 0.82 |
| 12 | 30.5 | 21 | 40 | 41 | 40.5 | 930.25 | 1572.77 | 709.50 | 6957.85 | 7.48 | 4.42 | 0.80 | 0.90 | 5.99 | 3.99 | 19.585 | 21.14 | 117.27 | 84.27 | 0.83 |
| 13 | 28.5 | 21 | 41 | 39 | 40 | 812.25 | 1451.49 | 557.47 | 5466.88 | 6.73 | 3.77 | 0.78 | 0.88 | 5.23 | 3.33 | 19.245 | 20.88 | 100.58 | 69.58 | 0.70 |
| 14 | 28.98 | 42.76 | 42.65 | 41.64 | 42.145 | 839.8404 | 1555.09 | | | | | | | | | | | | | |
| 15 | 30.29 | 38.23 | 40.55 | 40.4 | 40.475 | 917.4841 | 1560.98 | INVALID TEST | | | | | | | | | | | | |
| 16 | 31.08 | 41.62 | 38.2 | 38.47 | 38.335 | 965.9664 | 1517.00 | | | | | | | | | | | | | |
| 17 | 28.14 | 39.9 | 40.02 | 39.59 | 39.805 | 791.8596 | 1426.17 | 653.00 | 6403.74 | 8.09 | 4.49 | 0.77 | 0.88 | 6.24 | 3.96 | 19.18 | 20.82 | 119.78 | 82.39 | 0.83 |
| 18 | 27.69 | 38.76 | 37.58 | 38.2 | 37.89 | 766.7361 | 1335.85 | 582.00 | 5707.47 | 7.44 | 4.27 | 0.77 | 0.87 | 5.71 | 3.71 | 19.11 | 20.61 | 109.02 | 76.49 | 0.78 |
| 19 | 30.12 | 42.61 | 33.31 | 34.54 | 33.925 | 907.2144 | 1301.02 | 483.00 | 4736.61 | 5.22 | 3.64 | 0.80 | 0.86 | 4.16 | 3.14 | 19.52 | 20.53 | 81.13 | 64.53 | 0.66 |
| 20 | 27.74 | 38.36 | 39.5 | 39.76 | 39.63 | 769.5076 | 1399.72 | 1337.00 | 13111.49 | 17.04 | 9.37 | 0.77 | 0.88 | 13.07 | 8.22 | 19.12 | 20.76 | 249.86 | 170.67 | 1.72 |
| 21 | 27.98 | 39.03 | 40.4 | 40.88 | 40.64 | 782.8804 | 1447.81 | 1005.00 | 9855.68 | 12.59 | 6.81 | 0.77 | 0.88 | 9.69 | 6.02 | 19.16 | 20.87 | 185.72 | 125.63 | 1.26 |
| 22 | 30.1 | 41.59 | 40.26 | 40.44 | 40.35 | 906.01 | 1546.39 | 562.00 | 5511.34 | 6.08 | 3.56 | 0.80 | 0.90 | 4.84 | 3.20 | 19.52 | 21.09 | 94.48 | 67.45 | 0.67 |
| 23 | 30.46 | 46.54 | 40.6 | 41.3 | 40.95 | 927.8116 | 1588.16 | INVALID TEST | | | | | | | | | | | | |
| 24 | 28.63 | 40.14 | 40.4 | 41.2 | 40.8 | 819.6769 | 1487.28 | 706.00 | 6923.49 | 8.45 | 4.66 | 0.78 | 0.89 | 6.57 | 4.14 | 19.27 | 20.96 | 126.63 | 86.80 | 0.87 |
| 25 | 31.06 | 42.73 | 32.3 | 32.97 | 32.635 | 964.7236 | 1290.61 | 395.00 | 3873.63 | 4.02 | 3.00 | 0.81 | 0.86 | 3.24 | 2.59 | 19.68 | 20.51 | 63.78 | 53.04 | 0.54 |
| 26 | 26.55 | 39.14 | 38.32 | 38.58 | 38.45 | 704.9025 | 1299.78 | 550.00 | 5393.66 | 7.65 | 4.15 | 0.75 | 0.86 | 5.76 | 3.58 | 18.91 | 20.53 | 108.85 | 73.53 | 0.75 |
| 27 | 24.92 | 39.52 | 39.05 | 38.47 | 38.76 | 621.0064 | 1229.82 | 465.00 | 4560.09 | 7.34 | 3.71 | 0.73 | 0.85 | 5.37 | 3.16 | 18.64 | 20.36 | 100.03 | 64.36 | 0.66 |

# APPENDIX C

Sensitivity Analysis of the Young's Modulus

## *Input Data*

Input Volume
Turbulence: Off
Wall Roughness: Off
Tip Effects: Off
Proppant Type: Carbo-Lite

| | | |
|---|---|---|
| Young's Modulus | 42000 | MPa |
| Fracture Toughness | 0.81 | MPa·m^½ |
| Poisson's Ratio | 0.14 | fraction |
| Total Pay Zone Height | 0.03048 | m |
| Total Fracture Height | 150 | m |
| Ellipsoidal Aspect Ratio | 1 | |
| Injection Rate (2-wings) | 0.1 | m³/min |
| Flow Behavior Index - n' | 0.5 | |
| Consistency Index - K' | 0.004788 | kPa·s^n' |
| Total Leak-off Coefficient | 0 | cm/min^½ |
| Spurt Loss Coefficient | 0 | cm |
| Total Volume Injected | 2500 | m³ |
| Max Proppant Concentration | 17 | 100 kg/m³ |

## *Output Solution*

| Parameters | GDK | |
|---|---|---|
| Length | 701.05 | m |
| Height (wellbore) | 150 | m |
| Max. Well Width | 1.5135 | cm |
| Average Well Width | 1.5135 | cm |
| Average Fracture Width | 1.1887 | cm |
| Net Pressure | 294.54 | kPa |
| Efficiency | 1 | fraction |
| Pumping Time | 25000 | min |
| Volume | 2500 | m³ |
| Proppant Mass | 4.25E+06 | kg |
| Percent Propped | 99.186 | % |

## *Input Data*

Input Volume
Turbulence: Off
Wall Roughness: Off
Tip Effects: Off
Proppant Type: Carbo-Lite

| | | |
|---|---|---|
| Young's Modulus | 44000 | MPa |
| Fracture Toughness | 0.81 | MPa·m^½ |
| Poisson's Ratio | 0.14 | fraction |
| Total Pay Zone Height | 0.03048 | m |
| Total Fracture Height | 150 | m |
| Ellipsoidal Aspect Ratio | 1 | |
| Injection Rate (2-wings) | 0.1 | m³/min |
| Flow Behavior Index - n' | 0.5 | |
| Consistency Index - K' | 0.004788 | kPa·s^n' |
| Total Leak-off Coefficient | 0 | cm/min^½ |
| Spurt Loss Coefficient | 0 | cm |
| Total Volume Injected | 2500 | m³ |
| Max Proppant Concentration | 17 | 100 kg/m³ |

## *Output Solution*

| Parameters | GDK | |
|---|---|---|
| Length | 707.88 | m |
| Height (wellbore) | 150 | m |
| Max. Well Width | 1.4989 | cm |
| Average Well Width | 1.4989 | cm |
| Average Fracture Width | 1.1772 | cm |
| Net Pressure | 302.64 | kPa |
| Efficiency | 1 | fraction |
| Pumping Time | 25000 | min |
| Volume | 2500 | m³ |
| Proppant Mass | 4.25E+06 | kg |
| Percent Propped | 99.186 | % |

## *Input Data*

Input Volume
Turbulence: Off
Wall Roughness: Off
Tip Effects: Off
Proppant Type: Carbo-Lite

| | | |
|---|---|---|
| Young's Modulus | 46000 | MPa |
| Fracture Toughness | 0.81 | MPa·m^½ |
| Poisson's Ratio | 0.14 | fraction |
| Total Pay Zone Height | 0.03048 | m |
| Total Fracture Height | 150 | m |
| Ellipsoidal Aspect Ratio | 1 | |
| Injection Rate (2-wings) | 0.1 | m³/min |
| Flow Behavior Index - n' | 0.5 | |
| Consistency Index - K' | 0.004788 | kPa·s^n' |
| Total Leak-off Coefficient | 0 | cm/min^½ |
| Spurt Loss Coefficient | 0 | cm |
| Total Volume Injected | 2500 | m³ |
| Max Proppant Concentration | 17 | 100 kg/m³ |

## *Output Solution*

| Parameters | GDK | |
|---|---|---|
| Length | 714.46 | m |
| Height (wellbore) | 150 | m |
| Max. Well Width | 1.4851 | cm |
| Average Well Width | 1.4851 | cm |
| Average Fracture Width | 1.1664 | cm |
| Net Pressure | 310.6 | kPa |
| Efficiency | 1 | fraction |
| Pumping Time | 25000 | min |
| Volume | 2500 | m³ |
| Proppant Mass | 4.25E+06 | kg |
| Percent Propped | 99.186 | % |

## *Input Data*

Input Volume
Turbulence: Off
Wall Roughness: Off
Tip Effects: Off
Proppant Type: Carbo-Lite

| | | |
|---|---|---|
| Young's Modulus | 48000 | MPa |
| Fracture Toughness | 0.81 | MPa·m^½ |
| Poisson's Ratio | 0.14 | fraction |
| Total Pay Zone Height | 0.03048 | m |
| Total Fracture Height | 150 | m |
| Ellipsoidal Aspect Ratio | 1 | |
| Injection Rate (2-wings) | 0.1 | m³/min |
| Flow Behavior Index - n' | 0.5 | |
| Consistency Index - K' | 0.004788 | kPa·s^n' |
| Total Leak-off Coefficient | 0 | cm/min^½ |
| Spurt Loss Coefficient | 0 | cm |
| Total Volume Injected | 2500 | m³ |
| Max Proppant Concentration | 17 | 100 kg/m³ |

## *Output Solution*

| Parameters | GDK | |
|---|---|---|
| Length | 720.81 | m |
| Height (wellbore) | 150 | m |
| Max. Well Width | 1.472 | cm |
| Average Well Width | 1.472 | cm |
| Average Fracture Width | 1.1561 | cm |
| Net Pressure | 318.42 | kPa |
| Efficiency | 1 | fraction |
| Pumping Time | 25000 | min |
| Volume | 2500 | m³ |
| Proppant Mass | 4.25E+06 | kg |
| Percent Propped | 99.186 | % |

## *Input Data*

Input Volume
Turbulence: Off
Wall Roughness: Off
Tip Effects: Off
Proppant Type: Carbo-Lite

| | | |
|---|---|---|
| Young's Modulus | 50000 | MPa |
| Fracture Toughness | 0.81 | MPa·m^½ |
| Poisson's Ratio | 0.14 | fraction |
| Total Pay Zone Height | 0.03048 | m |
| Total Fracture Height | 150 | m |
| Ellipsoidal Aspect Ratio | 1 | |
| Injection Rate (2-wings) | 0.1 | m³/min |
| Flow Behavior Index - n' | 0.5 | |
| Consistency Index - K' | 0.004788 | kPa·s^n' |
| Total Leak-off Coefficient | 0 | cm/min^½ |
| Spurt Loss Coefficient | 0 | cm |
| Total Volume Injected | 2500 | m³ |
| Max Proppant Concentration | 17 | 100 kg/m³ |

## *Output Solution*

| Parameters | GDK | |
|---|---|---|
| Length | 726.94 | m |
| Height (wellbore) | 150 | m |
| Max. Well Width | 1.4596 | cm |
| Average Well Width | 1.4596 | cm |
| Average Fracture Width | 1.1464 | cm |
| Net Pressure | 326.11 | kPa |
| Efficiency | 1 | fraction |
| Pumping Time | 25000 | min |
| Volume | 2500 | m³ |
| Proppant Mass | 4.25E+06 | kg |
| Percent Propped | 99.186 | % |

## *Input Data*

Input Volume
Turbulence: Off
Wall Roughness: Off
Tip Effects: Off
Proppant Type: Carbo-Lite

| | | |
|---|---|---|
| Young's Modulus | 52000 | MPa |
| Fracture Toughness | 0.81 | MPa·m^½ |
| Poisson's Ratio | 0.14 | fraction |
| Total Pay Zone Height | 0.03048 | m |
| Total Fracture Height | 150 | m |
| Ellipsoidal Aspect Ratio | 1 | |
| Injection Rate (2-wings) | 0.1 | m³/min |
| Flow Behavior Index - n' | 0.5 | |
| Consistency Index - K' | 0.00479 | kPa·s^n' |
| Total Leak-off Coefficient | 0 | cm/min^½ |
| Spurt Loss Coefficient | 0 | cm |
| Total Volume Injected | 2500 | m³ |
| Max Proppant Concentration | 17 | 100 kg/m³ |

## *Output Solution*

| Parameters | GDK | |
|---|---|---|
| Length | 732.88 | m |
| Height (wellbore) | 150 | m |
| Max. Well Width | 1.4478 | cm |
| Average Well Width | 1.4478 | cm |
| Average Fracture Width | 1.1371 | cm |
| Net Pressure | 333.68 | kPa |
| Efficiency | 1 | fraction |
| Pumping Time | 25000 | min |
| Volume | 2500 | m³ |
| Proppant Mass | 4.25E+06 | kg |
| Percent Propped | 99.186 | % |

## *Input Data*

Input Volume
Turbulence: Off
Wall Roughness: Off
Tip Effects: Off
Proppant Type: Carbo-Lite

| | | |
|---|---|---|
| Young's Modulus | 54000 | MPa |
| Fracture Toughness | 0.81 | MPa·m^½ |
| Poisson's Ratio | 0.14 | fraction |
| Total Pay Zone Height | 0.03048 | m |
| Total Fracture Height | 150 | m |
| Ellipsoidal Aspect Ratio | 1 | |
| Injection Rate (2-wings) | 0.1 | m³/min |
| Flow Behavior Index - n' | 0.5 | |
| Consistency Index - K' | 0.004788 | kPa·s^n' |
| Total Leak-off Coefficient | 0 | cm/min^½ |
| Spurt Loss Coefficient | 0 | cm |
| Total Volume Injected | 2500 | m³ |
| Max Proppant Concentration | 17 | 100 kg/m³ |

## *Output Solution*

| Parameters | GDK | |
|---|---|---|
| Length | 738.64 | m |
| Height (wellbore) | 150 | m |
| Max. Well Width | 1.4365 | cm |
| Average Well Width | 1.4365 | cm |
| Average Fracture Width | 1.1282 | cm |
| Net Pressure | 341.14 | kPa |
| Efficiency | 1 | fraction |
| Pumping Time | 25000 | min |
| Volume | 2500 | m³ |
| Proppant Mass | 4.25E+06 | kg |
| Percent Propped | 99.186 | % |

## *Input Data*

Input Volume
Turbulence: Off
Wall Roughness: Off
Tip Effects: Off
Proppant Type: Carbo-Lite

| | | |
|---|---|---|
| Young's Modulus | 56000 | MPa |
| Fracture Toughness | 0.81 | MPa·m^½ |
| Poisson's Ratio | 0.14 | fraction |
| Total Pay Zone Height | 0.03048 | m |
| Total Fracture Height | 150 | m |
| Ellipsoidal Aspect Ratio | 1 | |
| Injection Rate (2-wings) | 0.1 | m³/min |
| Flow Behavior Index - n' | 0.5 | |
| Consistency Index - K' | 0.004788 | kPa·s^n' |
| Total Leak-off Coefficient | 0 | cm/min^½ |
| Spurt Loss Coefficient | 0 | cm |
| Total Volume Injected | 2500 | m³ |
| Max Proppant Concentration | 17 | 100 kg/m³ |

## *Output Solution*

| Parameters | GDK | |
|---|---|---|
| Length | 744.22 | m |
| Height (wellbore) | 150 | m |
| Max. Well Width | 1.4257 | cm |
| Average Well Width | 1.4257 | cm |
| Average Fracture Width | 1.1197 | cm |
| Net Pressure | 348.48 | kPa |
| Efficiency | 1 | fraction |
| Pumping Time | 25000 | min |
| Volume | 2500 | m³ |
| Proppant Mass | 4.25E+06 | kg |
| Percent Propped | 99.186 | % |

## *Input Data*

Input Volume
Turbulence: Off
Wall Roughness: Off
Tip Effects: Off
Proppant Type: Carbo-Lite

| | | |
|---|---|---|
| Young's Modulus | 58000 | MPa |
| Fracture Toughness | 0.81 | MPa·m^½ |
| Poisson's Ratio | 0.14 | fraction |
| Total Pay Zone Height | 0.03048 | m |
| Total Fracture Height | 150 | m |
| Ellipsoidal Aspect Ratio | 1 | |
| Injection Rate (2-wings) | 0.1 | m³/min |
| Flow Behavior Index - n' | 0.5 | |
| Consistency Index - K' | 0.004788 | kPa·s^n' |
| Total Leak-off Coefficient | 0 | cm/min^½ |
| Spurt Loss Coefficient | 0 | cm |
| Total Volume Injected | 2500 | m³ |
| Max Proppant Concentration | 17 | 100 kg/m³ |

## *Output Solution*

| Parameters | GDK | |
|---|---|---|
| Length | 749.64 | m |
| Height (wellbore) | 150 | m |
| Max. Well Width | 1.4154 | cm |
| Average Well Width | 1.4154 | cm |
| Average Fracture Width | 1.1116 | cm |
| Net Pressure | 355.73 | kPa |
| Efficiency | 1 | fraction |
| Pumping Time | 25000 | min |
| Volume | 2500 | m³ |
| Proppant Mass | 4.25E+06 | kg |
| Percent Propped | 99.186 | % |

## *Input Data*

Input Volume
Turbulence: Off
Wall Roughness: Off
Tip Effects: Off
Proppant Type: Carbo-Lite

| | | |
|---|---|---|
| Young's Modulus | 60000 | MPa |
| Fracture Toughness | 0.81 | MPa·m^½ |
| Poisson's Ratio | 0.14 | fraction |
| Total Pay Zone Height | 0.03048 | m |
| Total Fracture Height | 150 | m |
| Ellipsoidal Aspect Ratio | 1 | |
| Injection Rate (2-wings) | 0.1 | m³/min |
| Flow Behavior Index - n' | 0.5 | |
| Consistency Index - K' | 0.004788 | kPa·s^n' |
| Total Leak-off Coefficient | 0 | cm/min^½ |
| Spurt Loss Coefficient | 0 | cm |
| Total Volume Injected | 2500 | m³ |
| Max Proppant Concentration | 17 | 100 kg/m³ |

## *Output Solution*

| Parameters | GDK | |
|---|---|---|
| Length | 754.91 | m |
| Height (wellbore) | 150 | m |
| Max. Well Width | 1.4055 | cm |
| Average Well Width | 1.4055 | cm |
| Average Fracture Width | 1.1039 | cm |
| Net Pressure | 362.87 | kPa |
| Efficiency | 1 | fraction |
| Pumping Time | 25000 | min |
| Volume | 2500 | m³ |
| Proppant Mass | 4.25E+06 | kg |
| Percent Propped | 99.186 | % |

# APPENDIX D

Sensitivity Analysis of the Poisson's Ratio

## *Input Data*

Input Volume
Turbulence: Off
Wall Roughness: Off
Tip Effects: Off
Proppant Type: Carbo-Lite

| | | |
|---|---|---|
| Young's Modulus | 50000 | MPa |
| Fracture Toughness | 0.81 | MPa·m^½ |
| Poisson's Ratio | 0.1 | fraction |
| Total Pay Zone Height | 0.03048 | m |
| Total Fracture Height | 150 | m |
| Ellipsoidal Aspect Ratio | 1 | |
| Injection Rate (2-wings) | 0.1 | m³/min |
| Flow Behavior Index - n' | 0.5 | |
| Consistency Index - K' | 0.00479 | kPa·s^n' |
| Total Leak-off Coefficient | 0 | cm/min^½ |
| Spurt Loss Coefficient | 0 | cm |
| Total Volume Injected | 2500 | m³ |
| Max Proppant Concentration | 17 | 100 kg/m³ |

## *Output Solution*

| Parameters | GDK | |
|---|---|---|
| Length | 725.47 | m |
| Height (wellbore) | 150 | m |
| Max. Well Width | 1.4625 | cm |
| Average Well Width | 1.4625 | cm |
| Average Fracture Width | 1.1487 | cm |
| Net Pressure | 324.26 | kPa |
| Efficiency | 1 | fraction |
| Pumping Time | 25000 | min |
| Volume | 2500 | m³ |
| Proppant Mass | 4.25E+06 | kg |
| Percent Propped | 99.186 | % |

## *Input Data*

Input Volume
Turbulence: Off
Wall Roughness: Off
Tip Effects: Off
Proppant Type: Carbo-Lite

| | | |
|---|---|---|
| Young's Modulus | 50000 | MPa |
| Fracture Toughness | 0.81 | MPa·m^½ |
| Poisson's Ratio | 0.12 | fraction |
| Total Pay Zone Height | 0.03048 | m |
| Total Fracture Height | 150 | m |
| Ellipsoidal Aspect Ratio | 1 | |
| Injection Rate (2-wings) | 0.1 | m³/min |
| Flow Behavior Index - n' | 0.5 | |
| Consistency Index - K' | 0.00479 | kPa·s^n' |
| Total Leak-off Coefficient | 0 | cm/min^½ |
| Spurt Loss Coefficient | 0 | cm |
| Total Volume Injected | 2500 | m³ |
| Max Proppant Concentration | 17 | 100 kg/m³ |

## *Output Solution*

| Parameters | GDK | |
|---|---|---|
| Length | 726.15 | m |
| Height (wellbore) | 150 | m |
| Max. Well Width | 1.4612 | cm |
| Average Well Width | 1.4612 | cm |
| Average Fracture Width | 1.1476 | cm |
| Net Pressure | 325.1 | kPa |
| Efficiency | 1 | fraction |
| Pumping Time | 25000 | min |
| Volume | 2500 | m³ |
| Proppant Mass | 4.25E+06 | kg |
| Percent Propped | 99.186 | % |

## *Input Data*

Input Volume
Turbulence: Off
Wall Roughness: Off
Tip Effects: Off
Proppant Type: Carbo-Lite

| | | |
|---|---|---|
| Young's Modulus | 50000 | MPa |
| Fracture Toughness | 0.81 | MPa·m^½ |
| Poisson's Ratio | 0.14 | fraction |
| Total Pay Zone Height | 0.03048 | m |
| Total Fracture Height | 150 | m |
| Ellipsoidal Aspect Ratio | 1 | |
| Injection Rate (2-wings) | 0.1 | m³/min |
| Flow Behavior Index - n' | 0.5 | |
| Consistency Index - K' | 0.00479 | kPa·s^n' |
| Total Leak-off Coefficient | 0 | cm/min^½ |
| Spurt Loss Coefficient | 0 | cm |
| Total Volume Injected | 2500 | m³ |
| Max Proppant Concentration | 17 | 100 kg/m³ |

## *Output Solution*

| Parameters | GDK | |
|---|---|---|
| Length | 726.94 | m |
| Height (wellbore) | 150 | m |
| Max. Well Width | 1.4596 | cm |
| Average Well Width | 1.4596 | cm |
| Average Fracture Width | 1.1464 | cm |
| Net Pressure | 326.11 | kPa |
| Efficiency | 1 | fraction |
| Pumping Time | 25000 | min |
| Volume | 2500 | m³ |
| Proppant Mass | 4.25E+06 | kg |
| Percent Propped | 99.186 | % |


## *Input Data*

Input Volume
Turbulence: Off
Wall Roughness: Off
Tip Effects: Off
Proppant Type: Carbo-Lite


| | | |
|---|---|---|
| Young's Modulus | 50000 | MPa |
| Fracture Toughness | 0.81 | MPa·m^½ |
| Poisson's Ratio | 0.16 | fraction |
| Total Pay Zone Height | 0.03048 | m |
| Total Fracture Height | 150 | m |
| Ellipsoidal Aspect Ratio | 1 | |
| Injection Rate (2-wings) | 0.1 | m³/min |
| Flow Behavior Index - n' | 0.5 | |
| Consistency Index - K' | 0.00479 | kPa·s^n' |
| Total Leak-off Coefficient | 0 | cm/min^½ |
| Spurt Loss Coefficient | 0 | cm |
| Total Volume Injected | 2500 | m³ |
| Max Proppant Concentration | 17 | 100 kg/m³ |

## *Output Solution*

| Parameters | GDK | |
|---|---|---|
| Length | 727.87 | m |
| Height (wellbore) | 150 | m |
| Max. Well Width | 1.4577 | cm |
| Average Well Width | 1.4577 | cm |
| Average Fracture Width | 1.1449 | cm |
| Net Pressure | 327.28 | kPa |
| Efficiency | 1 | fraction |
| Pumping Time | 25000 | min |
| Volume | 2500 | m³ |
| Proppant Mass | 4.25E+06 | kg |
| Percent Propped | 99.186 | % |

## *Input Data*

Input Volume
Turbulence: Off
Wall Roughness: Off
Tip Effects: Off
Proppant Type: Carbo-Lite

| | | |
|---|---|---|
| Young's Modulus | 50000 | MPa |
| Fracture Toughness | 0.81 | MPa·m^½ |
| Poisson's Ratio | 0.18 | fraction |
| Total Pay Zone Height | 0.03048 | m |
| Total Fracture Height | 150 | m |
| Ellipsoidal Aspect Ratio | 1 | |
| Injection Rate (2-wings) | 0.1 | m³/min |
| Flow Behavior Index - n' | 0.5 | |
| Consistency Index - K' | 0.00479 | kPa·s^n' |
| Total Leak-off Coefficient | 0 | cm/min^½ |
| Spurt Loss Coefficient | 0 | cm |
| Total Volume Injected | 2500 | m³ |
| Max Proppant Concentration | 17 | 100 kg/m³ |

## *Output Solution*

| Parameters | GDK | |
|---|---|---|
| Length | 728.93 | m |
| Height (wellbore) | 150 | m |
| Max. Well Width | 1.4556 | cm |
| Average Well Width | 1.4556 | cm |
| Average Fracture Width | 1.1432 | cm |
| Net Pressure | 328.63 | kPa |
| Efficiency | 1 | fraction |
| Pumping Time | 25000 | min |
| Volume | 2500 | m³ |
| Proppant Mass | 4.25E+06 | kg |
| Percent Propped | 99.186 | % |


## *Input Data*

Input Volume
Turbulence: Off
Wall Roughness: Off
Tip Effects: Off
Proppant Type: Carbo-Lite


| | | |
|---|---|---|
| Young's Modulus | 50000 | MPa |
| Fracture Toughness | 0.81 | MPa·m^½ |
| Poisson's Ratio | 0.2 | fraction |
| Total Pay Zone Height | 0.03048 | m |
| Total Fracture Height | 150 | m |
| Ellipsoidal Aspect Ratio | 1 | |
| Injection Rate (2-wings) | 0.1 | m³/min |
| Flow Behavior Index - n' | 0.5 | |
| Consistency Index - K' | 0.00479 | kPa·s^n' |
| Total Leak-off Coefficient | 0 | cm/min^½ |
| Spurt Loss Coefficient | 0 | cm |
| Total Volume Injected | 2500 | m³ |
| Max Proppant Concentration | 17 | 100 kg/m³ |

## *Output Solution*

| Parameters | GDK | |
|---|---|---|
| Length | 730.12 | m |
| Height (wellbore) | 150 | m |
| Max. Well Width | 1.4532 | cm |
| Average Well Width | 1.4532 | cm |
| Average Fracture Width | 1.1414 | cm |
| Net Pressure | 330.15 | kPa |
| Efficiency | 1 | fraction |
| Pumping Time | 25000 | min |
| Volume | 2500 | m³ |
| Proppant Mass | 4.25E+06 | kg |
| Percent Propped | 99.186 | % |

## *Input Data*

Input Volume
Turbulence: Off
Wall Roughness: Off
Tip Effects: Off
Proppant Type: Carbo-Lite

| | | |
|---|---|---|
| Young's Modulus | 50000 | MPa |
| Fracture Toughness | 0.81 | MPa·m^½ |
| Poisson's Ratio | 0.22 | fraction |
| Total Pay Zone Height | 0.03048 | m |
| Total Fracture Height | 150 | m |
| Ellipsoidal Aspect Ratio | 1 | |
| Injection Rate (2-wings) | 0.1 | m³/min |
| Flow Behavior Index - n' | 0.5 | |
| Consistency Index - K' | 0.00479 | kPa·s^n' |
| Total Leak-off Coefficient | 0 | cm/min^½ |
| Spurt Loss Coefficient | 0 | cm |
| Total Volume Injected | 2500 | m³ |
| Max Proppant Concentration | 17 | 100 kg/m³ |

## *Output Solution*

| Parameters | GDK | |
|---|---|---|
| Length | 731.45 | m |
| Height (wellbore) | 150 | m |
| Max. Well Width | 1.4506 | cm |
| Average Well Width | 1.4506 | cm |
| Average Fracture Width | 1.1393 | cm |
| Net Pressure | 331.85 | kPa |
| Efficiency | 1 | fraction |
| Pumping Time | 25000 | min |
| Volume | 2500 | m³ |
| Proppant Mass | 4.25E+06 | kg |
| Percent Propped | 99.186 | % |


## *Input Data*

Input Volume
Turbulence: Off
Wall Roughness: Off
Tip Effects: Off
Proppant Type: Carbo-Lite


| | | |
|---|---|---|
| Young's Modulus | 50000 | MPa |
| Fracture Toughness | 0.81 | MPa·m^½ |
| Poisson's Ratio | 0.24 | fraction |
| Total Pay Zone Height | 0.03048 | m |
| Total Fracture Height | 150 | m |
| Ellipsoidal Aspect Ratio | 1 | |
| Injection Rate (2-wings) | 0.1 | m³/min |
| Flow Behavior Index - n' | 0.5 | |
| Consistency Index - K' | 0.00479 | kPa·s^n' |
| Total Leak-off Coefficient | 0 | cm/min^½ |
| Spurt Loss Coefficient | 0 | cm |
| Total Volume Injected | 2500 | m³ |
| Max Proppant Concentration | 17 | 100 kg/m³ |

## *Output Solution*

| Parameters | GDK | |
|---|---|---|
| Length | 732.93 | m |
| Height (wellbore) | 150 | m |
| Max. Well Width | 1.4477 | cm |
| Average Well Width | 1.4477 | cm |
| Average Fracture Width | 1.137 | cm |
| Net Pressure | 333.74 | kPa |
| Efficiency | 1 | fraction |
| Pumping Time | 25000 | min |
| Volume | 2500 | m³ |
| Proppant Mass | 4.25E+06 | kg |
| Percent Propped | 99.186 | % |

## *Input Data*

Input Volume
Turbulence: Off
Wall Roughness: Off
Tip Effects: Off
Proppant Type: Carbo-Lite

| | | |
|---|---|---|
| Young's Modulus | 50000 | MPa |
| Fracture Toughness | 0.81 | MPa·m^½ |
| Poisson's Ratio | 0.26 | fraction |
| Total Pay Zone Height | 0.03048 | m |
| Total Fracture Height | 150 | m |
| Ellipsoidal Aspect Ratio | 1 | |
| Injection Rate (2-wings) | 0.1 | m³/min |
| Flow Behavior Index - n' | 0.5 | |
| Consistency Index - K' | 0.00479 | kPa·s^n' |
| Total Leak-off Coefficient | 0 | cm/min^½ |
| Spurt Loss Coefficient | 0 | cm |
| Total Volume Injected | 2500 | m³ |
| Max Proppant Concentration | 17 | 100 kg/m³ |

## *Output Solution*

| Parameters | GDK | |
|---|---|---|
| Length | 734.55 | m |
| Height (wellbore) | 150 | m |
| Max. Well Width | 1.4445 | cm |
| Average Well Width | 1.4445 | cm |
| Average Fracture Width | 1.1345 | cm |
| Net Pressure | 335.83 | kPa |
| Efficiency | 1 | fraction |
| Pumping Time | 25000 | min |
| Volume | 2500 | m³ |
| Proppant Mass | 4.25E+06 | kg |
| Percent Propped | 99.186 | % |

## *Input Data*

Input Volume
Turbulence: Off
Wall Roughness: Off
Tip Effects: Off
Proppant Type: Carbo-Lite

| | | |
|---|---|---|
| Young's Modulus | 50000 | MPa |
| Fracture Toughness | 0.81 | MPa·m^½ |
| Poisson's Ratio | 0.28 | fraction |
| Total Pay Zone Height | 0.03048 | m |
| Total Fracture Height | 150 | m |
| Ellipsoidal Aspect Ratio | 1 | |
| Injection Rate (2-wings) | 0.1 | m³/min |
| Flow Behavior Index - n' | 0.5 | |
| Consistency Index - K' | 0.00479 | kPa·s^n' |
| Total Leak-off Coefficient | 0 | cm/min^½ |
| Spurt Loss Coefficient | 0 | cm |
| Total Volume Injected | 2500 | m³ |
| Max Proppant Concentration | 17 | 100 kg/m³ |

## *Output Solution*

| Parameters | GDK | |
|---|---|---|
| Length | 736.33 | m |
| Height (wellbore) | 150 | m |
| Max. Well Width | 1.441 | cm |
| Average Well Width | 1.441 | cm |
| Average Fracture Width | 1.1317 | cm |
| Net Pressure | 338.13 | kPa |
| Efficiency | 1 | fraction |
| Pumping Time | 25000 | min |
| Volume | 2500 | m³ |
| Proppant Mass | 4.25E+06 | kg |
| Percent Propped | 99.186 | % |

# APPENDIX E

Sensitivity Analysis of the Fracture Toughness

### *Input Data*

Input Volume
Turbulence: Off
Wall Roughness: Off
Tip Effects: Off
Proppant Type: Carbo-Lite

| | | |
|---|---|---|
| Young's Modulus | 60000 | MPa |
| Fracture Toughness | 0.1 | MPa·m^½ |
| Poisson's Ratio | 0.14 | fraction |
| Total Pay Zone Height | 0.03048 | m |
| Total Fracture Height | 150 | m |
| Ellipsoidal Aspect Ratio | 1 | |
| Injection Rate (2-wings) | 0.1 | m³/min |
| Flow Behavior Index - n' | 0.5 | |
| Consistency Index - K' | 0.004788 | kPa·s^n' |
| Total Leak-off Coefficient | 0 | cm/min^½ |
| Spurt Loss Coefficient | 0 | cm |
| Total Volume Injected | 2500 | m³ |
| Max Proppant Concentration | 17 | 100 kg/m³ |

### *Output Solution*

| Parameters | GDK | |
|---|---|---|
| Length | 761.16 | m |
| Height (wellbore) | 150 | m |
| Max. Well Width | 1.394 | cm |
| Average Well Width | 1.394 | cm |
| Average Fracture Width | 1.0948 | cm |
| Net Pressure | 356.94 | kPa |
| Efficiency | 1 | fraction |
| Pumping Time | 25000 | min |
| Volume | 2500 | m³ |
| Proppant Mass | 4.25E+06 | kg |
| Percent Propped | 99.186 | % |

### *Input Data*

Input Volume
Turbulence: Off
Wall Roughness: Off
Tip Effects: Off
Proppant Type: Carbo-Lite

| | | |
|---|---|---|
| Young's Modulus | 60000 | MPa |
| Fracture Toughness | 0.2 | MPa·m^½ |
| Poisson's Ratio | 0.14 | fraction |
| Total Pay Zone Height | 0.03048 | m |
| Total Fracture Height | 150 | m |
| Ellipsoidal Aspect Ratio | 1 | |
| Injection Rate (2-wings) | 0.1 | m³/min |
| Flow Behavior Index - n' | 0.5 | |
| Consistency Index - K' | 0.004788 | kPa·s^n' |
| Total Leak-off Coefficient | 0 | cm/min^½ |
| Spurt Loss Coefficient | 0 | cm |
| Total Volume Injected | 2500 | m³ |
| Max Proppant Concentration | 17 | 100 kg/m³ |

### *Output Solution*

| Parameters | GDK | |
|---|---|---|
| Length | 760.28 | m |
| Height (wellbore) | 150 | m |
| Max. Well Width | 1.3956 | cm |
| Average Well Width | 1.3956 | cm |
| Average Fracture Width | 1.0961 | cm |
| Net Pressure | 357.77 | kPa |
| Efficiency | 1 | fraction |
| Pumping Time | 25000 | min |
| Volume | 2500 | m³ |
| Proppant Mass | 4.25E+06 | kg |
| Percent Propped | 99.186 | % |

## *Input Data*

Input Volume
Turbulence: Off
Wall Roughness: Off
Tip Effects: Off
Proppant Type: Carbo-Lite

| | | |
|---|---|---|
| Young's Modulus | 60000 | MPa |
| Fracture Toughness | 0.3 | MPa·m^½ |
| Poisson's Ratio | 0.14 | fraction |
| Total Pay Zone Height | 0.03048 | m |
| Total Fracture Height | 150 | m |
| Ellipsoidal Aspect Ratio | 1 | |
| Injection Rate (2-wings) | 0.1 | m³/min |
| Flow Behavior Index - n' | 0.5 | |
| Consistency Index - K' | 0.004788 | kPa·s^n' |
| Total Leak-off Coefficient | 0 | cm/min^½ |
| Spurt Loss Coefficient | 0 | cm |
| Total Volume Injected | 2500 | m³ |
| Max Proppant Concentration | 17 | 100 kg/m³ |

## *Output Solution*

| Parameters | GDK | |
|---|---|---|
| Length | 759.4 | m |
| Height (wellbore) | 150 | m |
| Max. Well Width | 1.3972 | cm |
| Average Well Width | 1.3972 | cm |
| Average Fracture Width | 1.0974 | cm |
| Net Pressure | 358.59 | kPa |
| Efficiency | 1 | fraction |
| Pumping Time | 25000 | min |
| Volume | 2500 | m³ |
| Proppant Mass | 4.25E+06 | kg |
| Percent Propped | 99.186 | % |


## *Input Data*

Input Volume
Turbulence: Off
Wall Roughness: Off
Tip Effects: Off
Proppant Type: Carbo-Lite


| | | |
|---|---|---|
| Young's Modulus | 60000 | MPa |
| Fracture Toughness | 0.4 | MPa·m^½ |
| Poisson's Ratio | 0.14 | fraction |
| Total Pay Zone Height | 0.03048 | m |
| Total Fracture Height | 150 | m |
| Ellipsoidal Aspect Ratio | 1 | |
| Injection Rate (2-wings) | 0.1 | m³/min |
| Flow Behavior Index - n' | 0.5 | |
| Consistency Index - K' | 0.004788 | kPa·s^n' |
| Total Leak-off Coefficient | 0 | cm/min^½ |
| Spurt Loss Coefficient | 0 | cm |
| Total Volume Injected | 2500 | m³ |
| Max Proppant Concentration | 17 | 100 kg/m³ |

## *Output Solution*

| Parameters | GDK | |
|---|---|---|
| Length | 758.52 | m |
| Height (wellbore) | 150 | m |
| Max. Well Width | 1.3988 | cm |
| Average Well Width | 1.3988 | cm |
| Average Fracture Width | 1.0986 | cm |
| Net Pressure | 359.42 | kPa |
| Efficiency | 1 | fraction |
| Pumping Time | 25000 | min |
| Volume | 2500 | m³ |
| Proppant Mass | 4.25E+06 | kg |
| Percent Propped | 99.186 | % |

## *Input Data*

Input Volume
Turbulence: Off
Wall Roughness: Off
Tip Effects: Off
Proppant Type: Carbo-Lite

| | | |
|---|---|---|
| Young's Modulus | 60000 | MPa |
| Fracture Toughness | 0.5 | MPa·m^½ |
| Poisson's Ratio | 0.14 | fraction |
| Total Pay Zone Height | 0.03048 | m |
| Total Fracture Height | 150 | m |
| Ellipsoidal Aspect Ratio | 1 | |
| Injection Rate (2-wings) | 0.1 | m³/min |
| Flow Behavior Index - n' | 0.5 | |
| Consistency Index - K' | 0.004788 | kPa·s^n' |
| Total Leak-off Coefficient | 0 | cm/min^½ |
| Spurt Loss Coefficient | 0 | cm |
| Total Volume Injected | 2500 | m³ |
| Max Proppant Concentration | 17 | 100 kg/m³ |

## *Output Solution*

| Parameters | GDK | |
|---|---|---|
| Length | 757.65 | m |
| Height (wellbore) | 150 | m |
| Max. Well Width | 1.4004 | cm |
| Average Well Width | 1.4004 | cm |
| Average Fracture Width | 1.0999 | cm |
| Net Pressure | 360.26 | kPa |
| Efficiency | 1 | fraction |
| Pumping Time | 25000 | min |
| Volume | 2500 | m³ |
| Proppant Mass | 4.25E+06 | kg |
| Percent Propped | 99.186 | % |

## *Input Data*

Input Volume
Turbulence: Off
Wall Roughness: Off
Tip Effects: Off
Proppant Type: Carbo-Lite

| | | |
|---|---|---|
| Young's Modulus | 60000 | MPa |
| Fracture Toughness | 0.6 | MPa·m^½ |
| Poisson's Ratio | 0.14 | fraction |
| Total Pay Zone Height | 0.03048 | m |
| Total Fracture Height | 150 | m |
| Ellipsoidal Aspect Ratio | 1 | |
| Injection Rate (2-wings) | 0.1 | m³/min |
| Flow Behavior Index - n' | 0.5 | |
| Consistency Index - K' | 0.00479 | kPa·s^n' |
| Total Leak-off Coefficient | 0 | cm/min^½ |
| Spurt Loss Coefficient | 0 | cm |
| Total Volume Injected | 2500 | m³ |
| Max Proppant Concentration | 17 | 100 kg/m³ |

## *Output Solution*

| Parameters | GDK | |
|---|---|---|
| Length | 756.77 | m |
| Height (wellbore) | 150 | m |
| Max. Well Width | 1.4021 | cm |
| Average Well Width | 1.4021 | cm |
| Average Fracture Width | 1.1012 | cm |
| Net Pressure | 361.1 | kPa |
| Efficiency | 1 | fraction |
| Pumping Time | 25000 | min |
| Volume | 2500 | m³ |
| Proppant Mass | 4.25E+06 | kg |
| Percent Propped | 99.186 | % |

## *Input Data*

Input Volume
Turbulence: Off
Wall Roughness: Off
Tip Effects: Off
Proppant Type: Carbo-Lite

| | | |
|---|---|---|
| Young's Modulus | 60000 | MPa |
| Fracture Toughness | 0.7 | MPa·m^½ |
| Poisson's Ratio | 0.14 | fraction |
| Total Pay Zone Height | 0.03048 | m |
| Total Fracture Height | 150 | m |
| Ellipsoidal Aspect Ratio | 1 | |
| Injection Rate (2-wings) | 0.1 | m³/min |
| Flow Behavior Index - n' | 0.5 | |
| Consistency Index - K' | 0.004788 | kPa·s^n' |
| Total Leak-off Coefficient | 0 | cm/min^½ |
| Spurt Loss Coefficient | 0 | cm |
| Total Volume Injected | 2500 | m³ |
| Max Proppant Concentration | 17 | 100 kg/m³ |

## *Output Solution*

| Parameters | GDK | |
|---|---|---|
| Length | 755.88 | m |
| Height (wellbore) | 150 | m |
| Max. Well Width | 1.4037 | cm |
| Average Well Width | 1.4037 | cm |
| Average Fracture Width | 1.1025 | cm |
| Net Pressure | 361.94 | kPa |
| Efficiency | 1 | fraction |
| Pumping Time | 25000 | min |
| Volume | 2500 | m³ |
| Proppant Mass | 4.25E+06 | kg |
| Percent Propped | 99.186 | % |


## *Input Data*

Input Volume
Turbulence: Off
Wall Roughness: Off
Tip Effects: Off
Proppant Type: Carbo-Lite


| | | |
|---|---|---|
| Young's Modulus | 60000 | MPa |
| Fracture Toughness | 0.8 | MPa·m^½ |
| Poisson's Ratio | 0.14 | fraction |
| Total Pay Zone Height | 0.03048 | m |
| Total Fracture Height | 150 | m |
| Ellipsoidal Aspect Ratio | 1 | |
| Injection Rate (2-wings) | 0.1 | m³/min |
| Flow Behavior Index - n' | 0.5 | |
| Consistency Index - K' | 0.004788 | kPa·s^n' |
| Total Leak-off Coefficient | 0 | cm/min^½ |
| Spurt Loss Coefficient | 0 | cm |
| Total Volume Injected | 2500 | m³ |
| Max Proppant Concentration | 17 | 100 kg/m³ |

## *Output Solution*

| Parameters | GDK | |
|---|---|---|
| Length | 755 | m |
| Height (wellbore) | 150 | m |
| Max. Well Width | 1.4053 | cm |
| Average Well Width | 1.4053 | cm |
| Average Fracture Width | 1.1037 | cm |
| Net Pressure | 362.79 | kPa |
| Efficiency | 1 | fraction |
| Pumping Time | 25000 | min |
| Volume | 2500 | m³ |
| Proppant Mass | 4.25E+06 | kg |
| Percent Propped | 99.186 | % |

## *Input Data*

Input Volume
Turbulence: Off
Wall Roughness: Off
Tip Effects: Off
Proppant Type: Carbo-Lite

| | | |
|---|---|---|
| Young's Modulus | 60000 | MPa |
| Fracture Toughness | 0.9 | MPa·m^½ |
| Poisson's Ratio | 0.14 | fraction |
| Total Pay Zone Height | 0.03048 | m |
| Total Fracture Height | 150 | m |
| Ellipsoidal Aspect Ratio | 1 | |
| Injection Rate (2-wings) | 0.1 | m³/min |
| Flow Behavior Index - n' | 0.5 | |
| Consistency Index - K' | 0.004788 | kPa·s^n' |
| Total Leak-off Coefficient | 0 | cm/min^½ |
| Spurt Loss Coefficient | 0 | cm |
| Total Volume Injected | 2500 | m³ |
| Max Proppant Concentration | 17 | 100 kg/m³ |

## *Output Solution*

| Parameters | GDK | |
|---|---|---|
| Length | 754.12 | m |
| Height (wellbore) | 150 | m |
| Max. Well Width | 1.407 | cm |
| Average Well Width | 1.407 | cm |
| Average Fracture Width | 1.105 | cm |
| Net Pressure | 363.64 | kPa |
| Efficiency | 1 | fraction |
| Pumping Time | 25000 | min |
| Volume | 2500 | m³ |
| Proppant Mass | 4.25E+06 | kg |
| Percent Propped | 99.186 | % |


## *Input Data*

Input Volume
Turbulence: Off
Wall Roughness: Off
Tip Effects: Off
Proppant Type: Carbo-Lite


| | | |
|---|---|---|
| Young's Modulus | 60000 | MPa |
| Fracture Toughness | 0.1 | MPa·m^½ |
| Poisson's Ratio | 0.14 | fraction |
| Total Pay Zone Height | 0.03048 | m |
| Total Fracture Height | 150 | m |
| Ellipsoidal Aspect Ratio | 1 | |
| Injection Rate (2-wings) | 0.1 | m³/min |
| Flow Behavior Index - n' | 0.5 | |
| Consistency Index - K' | 0.004788 | kPa·s^n' |
| Total Leak-off Coefficient | 0 | cm/min^½ |
| Spurt Loss Coefficient | 0 | cm |
| Total Volume Injected | 2500 | m³ |
| Max Proppant Concentration | 17 | 100 kg/m³ |

## *Output Solution*

| Parameters | GDK | |
|---|---|---|
| Length | 761.16 | m |
| Height (wellbore) | 150 | m |
| Max. Well Width | 1.394 | cm |
| Average Well Width | 1.394 | cm |
| Average Fracture Width | 1.0948 | cm |
| Net Pressure | 356.94 | kPa |
| Efficiency | 1 | fraction |
| Pumping Time | 25000 | min |
| Volume | 2500 | m³ |
| Proppant Mass | 4.25E+06 | kg |
| Percent Propped | 99.186 | % |

# APPENDIX F

## Sensitivity Analysis of the Flow Behavior Index

| Input Data | | Input Data | | Input Data | | |
|---|---|---|---|---|---|---|
| Input Volume | | Input Volume | | Input Volume | | |
| Turbulence: Off | | Turbulence: Off | | Turbulence: Off | | |
| Wall Roughness: Off | | Wall Roughness: Off | | Wall Roughness: Off | | |
| Tip Effects: Off | | Tip Effects: Off | | Tip Effects: Off | | |
| Proppant Type: Carbo-Lite | | Proppant Type: Carbo-Lite | | Proppant Type: Carbo-Lite | | |
| Young's Modulus | 50000 | Young's Modulus | 50000 | Young's Modulus | 50000 | MPa |
| Fracture Toughness | 0.81 | Fracture Toughness | 0.81 | Fracture Toughness | 0.81 | MPa·m^½ |
| Poisson's Ratio | 0.14 | Poisson's Ratio | 0.14 | Poisson's Ratio | 0.14 | fraction |
| Total Pay Zone Height | 0.03048 | Total Pay Zone Height | 0.03048 | Total Pay Zone Height | 0.03048 | m |
| Total Fracture Height | 150 | Total Fracture Height | 150 | Total Fracture Height | 150 | m |
| Ellipsoidal Aspect Ratio | 1 | Ellipsoidal Aspect Ratio | 1 | Ellipsoidal Aspect Ratio | 1 | |
| Injection Rate (2-wings) | 5 | Injection Rate (2-wings) | 5 | Injection Rate (2-wings) | 5 | m³/min |
| Flow Behavior Index - n' | 0.6 | Flow Behavior Index - n' | 0.5 | Flow Behavior Index - n' | 0.4 | |
| Consistency Index - K' | 0.004788 | Consistency Index - K' | 0.004788 | Consistency Index - K' | 0.004788 | kPa·s^n' |
| Total Leak-off Coefficient | 0 | Total Leak-off Coefficient | 0 | Total Leak-off Coefficient | 0 | cm/min^½ |
| Spurt Loss Coefficient | 0 | Spurt Loss Coefficient | 0 | Spurt Loss Coefficient | 0 | cm |
| Total Volume Injected | 2500 | Total Volume Injected | 2500 | Total Volume Injected | 2500 | m³ |
| Max Proppant Concentration | 17 | Max Proppant Concentration | 17 | Max Proppant Concentration | 17 | 100 kg/m³ |
| Output Solution | | Output Solution | | Output Solution | | |
| Parameters | GDK | Parameters | GDK | Parameters | GDK | |
| Length | 484.15 | Length | 493.94 | Length | 505.29 | m |
| Height (wellbore) | 150 | Height (wellbore) | 150 | Height (wellbore) | 150 | m |
| Max. Well Width | 2.1915 | Max. Well Width | 2.1481 | Max. Well Width | 2.0999 | cm |
| Average Well Width | 2.1915 | Average Well Width | 2.1481 | Average Well Width | 2.0999 | cm |
| Average Fracture Width | 1.7212 | Average Fracture Width | 1.6871 | Average Fracture Width | 1.6492 | cm |
| Net Pressure | 735.2 | Net Pressure | 706.35 | Net Pressure | 674.98 | kPa |
| Efficiency | 1 | Efficiency | 1 | Efficiency | 1 | fraction |
| Pumping Time | 500 | Pumping Time | 500 | Pumping Time | 500 | min |
| Volume | 2500 | Volume | 2500 | Volume | 2500 | m³ |
| Proppant Mass | 4.25E+06 | Proppant Mass | 4.25E+06 | Proppant Mass | 4.25E+06 | kg |
| Percent Propped | 99.186 | Percent Propped | 99.186 | Percent Propped | 99.186 | % |

| Input Data | | Input Data | | Input Data | | |
|---|---|---|---|---|---|---|
| Input Volume | | Input Volume | | Input Volume | | |
| Turbulence: Off | | Turbulence: Off | | Turbulence: Off | | |
| Wall Roughness: Off | | Wall Roughness: Off | | Wall Roughness: Off | | |
| Tip Effects: Off | | Tip Effects: Off | | Tip Effects: Off | | |
| Proppant Type: Carbo-Lite | | Proppant Type: Carbo-Lite | | Proppant Type: Carbo-Lite | | |
| Young's Modulus | 50000 | Young's Modulus | 50000 | Young's Modulus | 50000 | MPa |
| Fracture Toughness | 0.81 | Fracture Toughness | 0.81 | Fracture Toughness | 0.81 | MPa·m^½ |
| Poisson's Ratio | 0.14 | Poisson's Ratio | 0.14 | Poisson's Ratio | 0.14 | fraction |
| Total Pay Zone Height | 0.03048 | Total Pay Zone Height | 0.03048 | Total Pay Zone Height | 0.03048 | m |
| Total Fracture Height | 150 | Total Fracture Height | 150 | Total Fracture Height | 150 | m |
| Ellipsoidal Aspect Ratio | 1 | Ellipsoidal Aspect Ratio | 1 | Ellipsoidal Aspect Ratio | 1 | |
| Injection Rate (2-wings) | 10 | Injection Rate (2-wings) | 10 | Injection Rate (2-wings) | 10 | m³/min |
| Flow Behavior Index - n' | 0.6 | Flow Behavior Index - n' | 0.5 | Flow Behavior Index - n' | 0.4 | |
| Consistency Index - K' | 0.004788 | Consistency Index - K' | 0.004788 | Consistency Index - K' | 0.004788 | kPa·s^n' |
| Total Leak-off Coefficient | 0 | Total Leak-off Coefficient | 0 | Total Leak-off Coefficient | 0 | cm/min^½ |
| Spurt Loss Coefficient | 0 | Spurt Loss Coefficient | 0 | Spurt Loss Coefficient | 0 | cm |
| Total Volume Injected | 2500 | Total Volume Injected | 2500 | Total Volume Injected | 2500 | m³ |
| Max Proppant Concentration | 17 | Max Proppant Concentration | 17 | Max Proppant Concentration | 17 | 100 kg/m³ |
| Output Solution | | Output Solution | | Output Solution | | |
| Parameters | GDK | Parameters | GDK | Parameters | GDK | |
| Length | 447.22 | Length | 461.13 | Length | 477.18 | m |
| Height (wellbore) | 150 | Height (wellbore) | 150 | Height (wellbore) | 150 | m |
| Max. Well Width | 2.3725 | Max. Well Width | 2.3009 | Max. Well Width | 2.2235 | cm |
| Average Well Width | 2.3725 | Average Well Width | 2.3009 | Average Well Width | 2.2235 | cm |
| Average Fracture Width | 1.8634 | Average Fracture Width | 1.8071 | Average Fracture Width | 1.7464 | cm |
| Net Pressure | 861.65 | Net Pressure | 810.43 | Net Pressure | 756.83 | kPa |
| Efficiency | 1 | Efficiency | 1 | Efficiency | 1 | fraction |
| Pumping Time | 250 | Pumping Time | 250 | Pumping Time | 250 | min |
| Volume | 2500 | Volume | 2500 | Volume | 2500 | m³ |
| Proppant Mass | 4.25E+06 | Proppant Mass | 4.25E+06 | Proppant Mass | 4.25E+06 | kg |
| Percent Propped | 99.186 | Percent Propped | 99.186 | Percent Propped | 99.186 | % |

| Input Data | | Input Data | | Input Data | | |
|---|---|---|---|---|---|---|
| Input Volume | | Input Volume | | Input Volume | | |
| Turbulence: Off | | Turbulence: Off | | Turbulence: Off | | |
| Wall Roughness: Off | | Wall Roughness: Off | | Wall Roughness: Off | | |
| Tip Effects: Off | | Tip Effects: Off | | Tip Effects: Off | | |
| Proppant Type: Carbo-Lite | | Proppant Type: Carbo-Lite | | Proppant Type: Carbo-Lite | | |
| Young's Modulus | 50000 | Young's Modulus | 50000 | Young's Modulus | 50000 | MPa |
| Fracture Toughness | 0.81 | Fracture Toughness | 0.81 | Fracture Toughness | 0.81 | MPa·m^½ |
| Poisson's Ratio | 0.14 | Poisson's Ratio | 0.14 | Poisson's Ratio | 0.14 | fraction |
| Total Pay Zone Height | 0.03048 | Total Pay Zone Height | 0.03048 | Total Pay Zone Height | 0.03048 | m |
| Total Fracture Height | 150 | Total Fracture Height | 150 | Total Fracture Height | 150 | m |
| Ellipsoidal Aspect Ratio | 1 | Ellipsoidal Aspect Ratio | 1 | Ellipsoidal Aspect Ratio | 1 | |
| Injection Rate (2-wings) | 1 | Injection Rate (2-wings) | 1 | Injection Rate (2-wings) | 1 | m³/min |
| Flow Behavior Index - n' | 0.6 | Flow Behavior Index - n' | 0.5 | Flow Behavior Index - n' | 0.4 | |
| Consistency Index - K' | 0.004788 | Consistency Index - K' | 0.004788 | Consistency Index - K' | 0.004788 | kPa·s^n' |
| Total Leak-off Coefficient | 0 | Total Leak-off Coefficient | 0 | Total Leak-off Coefficient | 0 | cm/min^½ |
| Spurt Loss Coefficient | 0 | Spurt Loss Coefficient | 0 | Spurt Loss Coefficient | 0 | cm |
| Total Volume Injected | 2500 | Total Volume Injected | 2500 | Total Volume Injected | 2500 | m³ |
| Max Proppant Concentration | 17 | Max Proppant Concentration | 17 | Max Proppant Concentration | 17 | 100 kg/m³ |
| Output Solution | | Output Solution | | Output Solution | | |
| Parameters | GDK | Parameters | GDK | Parameters | GDK | |
| Length | 581.91 | Length | 579.25 | Length | 576.99 | m |
| Height (wellbore) | 150 | Height (wellbore) | 150 | Height (wellbore) | 150 | m |
| Max. Well Width | 1.8234 | Max. Well Width | 1.8317 | Max. Well Width | 1.8389 | cm |
| Average Well Width | 1.8234 | Average Well Width | 1.8317 | Average Well Width | 1.8389 | cm |
| Average Fracture Width | 1.4321 | Average Fracture Width | 1.4386 | Average Fracture Width | 1.4443 | cm |
| Net Pressure | 508.93 | Net Pressure | 513.61 | Net Pressure | 517.65 | kPa |
| Efficiency | 1 | Efficiency | 1 | Efficiency | 1 | fraction |
| Pumping Time | 2500 | Pumping Time | 2500 | Pumping Time | 2500 | min |
| Volume | 2500 | Volume | 2500 | Volume | 2500 | m³ |
| Proppant Mass | 4.25E+06 | Proppant Mass | 4.25E+06 | Proppant Mass | 4.25E+06 | kg |
| Percent Propped | 99.186 | Percent Propped | 99.186 | Percent Propped | 99.186 | % |

# APPENDIX G

Sensitivity Analysis of the Consistency Index

### *Input Data*

Input Volume
Turbulence: Off
Wall Roughness: Off
Tip Effects: Off
Proppant Type: Carbo-Lite

| | | |
|---|---|---|
| Young's Modulus | 50000 | MPa |
| Fracture Toughness | 0.81 | MPa·m^½ |
| Poisson's Ratio | 0.14 | fraction |
| Total Pay Zone Height | 0.03048 | m |
| Total Fracture Height | 150 | m |
| Ellipsoidal Aspect Ratio | 1 | |
| Injection Rate (2-wings) | 0.1 | m³/min |
| Flow Behavior Index - n' | 0.5 | |
| Consistency Index - K' | 0.00479 | kPa·s^n' |
| Total Leak-off Coefficient | 0 | cm/min^½ |
| Spurt Loss Coefficient | 0 | cm |
| Total Volume Injected | 2500 | m³ |
| Max Proppant Concentration | 17 | 100 kg/m³ |

### *Output Solution*

| Parameters | GDK | |
|---|---|---|
| Length | 726.94 | m |
| Height (wellbore) | 150 | m |
| Max. Well Width | 1.4596 | cm |
| Average Well Width | 1.4596 | cm |
| Average Fracture Width | 1.1464 | cm |
| Net Pressure | 326.11 | kPa |
| Efficiency | 1 | fraction |
| Pumping Time | 25000 | min |
| Volume | 2500 | m³ |
| Proppant Mass | 4.25E+06 | kg |
| Percent Propped | 99.186 | % |

### *Input Data*

Input Volume
Turbulence: Off
Wall Roughness: Off
Tip Effects: Off
Proppant Type: Carbo-Lite

| | | |
|---|---|---|
| Young's Modulus | 50000 | MPa |
| Fracture Toughness | 0.81 | MPa·m^½ |
| Poisson's Ratio | 0.14 | fraction |
| Total Pay Zone Height | 0.03048 | m |
| Total Fracture Height | 150 | m |
| Ellipsoidal Aspect Ratio | 1 | |
| Injection Rate (2-wings) | 0.1 | m³/min |
| Flow Behavior Index - n' | 0.5 | |
| Consistency Index - K' | 0.00958 | kPa·s^n' |
| Total Leak-off Coefficient | 0 | cm/min^½ |
| Spurt Loss Coefficient | 0 | cm |
| Total Volume Injected | 2500 | m³ |
| Max Proppant Concentration | 17 | 100 kg/m³ |

### *Output Solution*

| Parameters | GDK | |
|---|---|---|
| Length | 634.12 | m |
| Height (wellbore) | 150 | m |
| Max. Well Width | 1.6732 | cm |
| Average Well Width | 1.6732 | cm |
| Average Fracture Width | 1.3142 | cm |
| Net Pressure | 428.57 | kPa |
| Efficiency | 1 | fraction |
| Pumping Time | 25000 | min |
| Volume | 2500 | m³ |
| Proppant Mass | 4.25E+06 | kg |
| Percent Propped | 99.186 | % |

## *Input Data*

Input Volume

Turbulence: Off

Wall Roughness: Off

Tip Effects: Off

Proppant Type: Carbo-Lite

| | | |
|---|---|---|
| Young's Modulus | 50000 | MPa |
| Fracture Toughness | 0.81 | MPa·m^½ |
| Poisson's Ratio | 0.14 | fraction |
| Total Pay Zone Height | 0.03048 | m |
| Total Fracture Height | 150 | m |
| Ellipsoidal Aspect Ratio | 1 | |
| Injection Rate (2-wings) | 0.1 | m³/min |
| Flow Behavior Index - n' | 0.5 | |
| Consistency Index - K' | 0.01436 | kPa·s^n' |
| Total Leak-off Coefficient | 0 | cm/min^½ |
| Spurt Loss Coefficient | 0 | cm |
| Total Volume Injected | 2500 | m³ |
| Max Proppant Concentration | 17 | 100 kg/m³ |

## *Output Solution*

| Parameters | GDK | |
|---|---|---|
| Length | 585.31 | m |
| Height (wellbore) | 150 | m |
| Max. Well Width | 1.8128 | cm |
| Average Well Width | 1.8128 | cm |
| Average Fracture Width | 1.4237 | cm |
| Net Pressure | 503.03 | kPa |
| Efficiency | 1 | fraction |
| Pumping Time | 25000 | min |
| Volume | 2500 | m³ |
| Proppant Mass | 4.25E+06 | kg |
| Percent Propped | 99.186 | % |


## *Input Data*

Input Volume

Turbulence: Off

Wall Roughness: Off

Tip Effects: Off

Proppant Type: Carbo-Lite


| | | |
|---|---|---|
| Young's Modulus | 50000 | MPa |
| Fracture Toughness | 0.81 | MPa·m^½ |
| Poisson's Ratio | 0.14 | fraction |
| Total Pay Zone Height | 0.03048 | m |
| Total Fracture Height | 150 | m |
| Ellipsoidal Aspect Ratio | 1 | |
| Injection Rate (2-wings) | 0.1 | m³/min |
| Flow Behavior Index - n' | 0.5 | |
| Consistency Index - K' | 0.01915 | kPa·s^n' |
| Total Leak-off Coefficient | 0 | cm/min^½ |
| Spurt Loss Coefficient | 0 | cm |
| Total Volume Injected | 2500 | m³ |
| Max Proppant Concentration | 17 | 100 kg/m³ |

## *Output Solution*

| Parameters | GDK | |
|---|---|---|
| Length | 552.94 | m |
| Height (wellbore) | 150 | m |
| Max. Well Width | 1.9189 | cm |
| Average Well Width | 1.9189 | cm |
| Average Fracture Width | 1.5071 | cm |
| Net Pressure | 563.65 | kPa |
| Efficiency | 1 | fraction |
| Pumping Time | 25000 | min |
| Volume | 2500 | m³ |
| Proppant Mass | 4.25E+06 | kg |
| Percent Propped | 99.186 | % |

## *Input Data*

Input Volume
Turbulence: Off
Wall Roughness: Off
Tip Effects: Off
Proppant Type: Carbo-Lite

| | | |
|---|---|---|
| Young's Modulus | 50000 | MPa |
| Fracture Toughness | 0.81 | MPa·m^½ |
| Poisson's Ratio | 0.14 | fraction |
| Total Pay Zone Height | 0.03048 | m |
| Total Fracture Height | 150 | m |
| Ellipsoidal Aspect Ratio | 1 | |
| Injection Rate (2-wings) | 0.1 | m³/min |
| Flow Behavior Index - n' | 0.5 | |
| Consistency Index - K' | 0.02394 | kPa·s^n' |
| Total Leak-off Coefficient | 0 | cm/min^½ |
| Spurt Loss Coefficient | 0 | cm |
| Total Volume Injected | 2500 | m³ |
| Max Proppant Concentration | 17 | 100 kg/m³ |

## *Output Solution*

| Parameters | GDK | |
|---|---|---|
| Length | 529.05 | m |
| Height (wellbore) | 150 | m |
| Max. Well Width | 2.0056 | cm |
| Average Well Width | 2.0056 | cm |
| Average Fracture Width | 1.5752 | cm |
| Net Pressure | 615.71 | kPa |
| Efficiency | 1 | fraction |
| Pumping Time | 25000 | min |
| Volume | 2500 | m³ |
| Proppant Mass | 4.25E+06 | kg |
| Percent Propped | 99.186 | % |

## *Input Data*

Input Volume
Turbulence: Off
Wall Roughness: Off
Tip Effects: Off
Proppant Type: Carbo-Lite

| | | |
|---|---|---|
| Young's Modulus | 50000 | MPa |
| Fracture Toughness | 0.81 | MPa·m^½ |
| Poisson's Ratio | 0.14 | fraction |
| Total Pay Zone Height | 0.03048 | m |
| Total Fracture Height | 150 | m |
| Ellipsoidal Aspect Ratio | 1 | |
| Injection Rate (2-wings) | 0.1 | m³/min |
| Flow Behavior Index - n' | 0.5 | |
| Consistency Index - K' | 0.02873 | kPa·s^n' |
| Total Leak-off Coefficient | 0 | cm/min^½ |
| Spurt Loss Coefficient | 0 | cm |
| Total Volume Injected | 2500 | m³ |
| Max Proppant Concentration | 17 | 100 kg/m³ |

## *Output Solution*

| Parameters | GDK | |
|---|---|---|
| Length | 510.28 | m |
| Height (wellbore) | 150 | m |
| Max. Well Width | 2.0793 | cm |
| Average Well Width | 2.0793 | cm |
| Average Fracture Width | 1.6331 | cm |
| Net Pressure | 661.83 | kPa |
| Efficiency | 1 | fraction |
| Pumping Time | 25000 | min |
| Volume | 2500 | m³ |
| Proppant Mass | 4.25E+06 | kg |
| Percent Propped | 99.186 | % |

## *Input Data*

Input Volume
Turbulence: Off
Wall Roughness: Off
Tip Effects: Off
Proppant Type: Carbo-Lite

| | | |
|---|---|---|
| Young's Modulus | 50000 | MPa |
| Fracture Toughness | 0.81 | MPa·m^½ |
| Poisson's Ratio | 0.14 | fraction |
| Total Pay Zone Height | 0.03048 | m |
| Total Fracture Height | 150 | m |
| Ellipsoidal Aspect Ratio | 1 | |
| Injection Rate (2-wings) | 0.1 | m³/min |
| Flow Behavior Index - n' | 0.5 | |
| Consistency Index - K' | 0.03352 | kPa·s^n' |
| Total Leak-off Coefficient | 0 | cm/min^½ |
| Spurt Loss Coefficient | 0 | cm |
| Total Volume Injected | 2500 | m³ |
| Max Proppant Concentration | 17 | 100 kg/m³ |

## *Output Solution*

| Parameters | GDK | |
|---|---|---|
| Length | 494.93 | m |
| Height (wellbore) | 150 | m |
| Max. Well Width | 2.1438 | cm |
| Average Well Width | 2.1438 | cm |
| Average Fracture Width | 1.6837 | cm |
| Net Pressure | 703.53 | kPa |
| Efficiency | 1 | fraction |
| Pumping Time | 25000 | min |
| Volume | 2500 | m³ |
| Proppant Mass | 4.25E+06 | kg |
| Percent Propped | 99.186 | % |

## *Input Data*

Input Volume
Turbulence: Off
Wall Roughness: Off
Tip Effects: Off
Proppant Type: Carbo-Lite

| | | |
|---|---|---|
| Young's Modulus | 50000 | MPa |
| Fracture Toughness | 0.81 | MPa·m^½ |
| Poisson's Ratio | 0.14 | fraction |
| Total Pay Zone Height | 0.03048 | m |
| Total Fracture Height | 150 | m |
| Ellipsoidal Aspect Ratio | 1 | |
| Injection Rate (2-wings) | 0.1 | m³/min |
| Flow Behavior Index - n' | 0.5 | |
| Consistency Index - K' | 0.0383 | kPa·s^n' |
| Total Leak-off Coefficient | 0 | cm/min^½ |
| Spurt Loss Coefficient | 0 | cm |
| Total Volume Injected | 2500 | m³ |
| Max Proppant Concentration | 17 | 100 kg/m³ |

## *Output Solution*

| Parameters | GDK | |
|---|---|---|
| Length | 482 | m |
| Height (wellbore) | 150 | m |
| Max. Well Width | 2.2013 | cm |
| Average Well Width | 2.2013 | cm |
| Average Fracture Width | 1.7289 | cm |
| Net Pressure | 741.78 | kPa |
| Efficiency | 1 | fraction |
| Pumping Time | 25000 | min |
| Volume | 2500 | m³ |
| Proppant Mass | 4.25E+06 | kg |
| Percent Propped | 99.186 | % |

## *Input Data*

Input Volume
Turbulence: Off
Wall Roughness: Off
Tip Effects: Off
Proppant Type: Carbo-Lite

| | | |
|---|---|---|
| Young's Modulus | 50000 | MPa |
| Fracture Toughness | 0.81 | MPa·m^½ |
| Poisson's Ratio | 0.14 | fraction |
| Total Pay Zone Height | 0.03048 | m |
| Total Fracture Height | 150 | m |
| Ellipsoidal Aspect Ratio | 1 | |
| Injection Rate (2-wings) | 0.1 | m³/min |
| Flow Behavior Index - n' | 0.5 | |
| Consistency Index - K' | 0.04309 | kPa·s^n' |
| Total Leak-off Coefficient | 0 | cm/min^½ |
| Spurt Loss Coefficient | 0 | cm |
| Total Volume Injected | 2500 | m³ |
| Max Proppant Concentration | 17 | 100 kg/m³ |

## *Output Solution*

| Parameters | GDK | |
|---|---|---|
| Length | 470.87 | m |
| Height (wellbore) | 150 | m |
| Max. Well Width | 2.2533 | cm |
| Average Well Width | 2.2533 | cm |
| Average Fracture Width | 1.7698 | cm |
| Net Pressure | 777.25 | kPa |
| Efficiency | 1 | fraction |
| Pumping Time | 25000 | min |
| Volume | 2500 | m³ |
| Proppant Mass | 4.25E+06 | kg |
| Percent Propped | 99.186 | % |


## *Input Data*

Input Volume
Turbulence: Off
Wall Roughness: Off
Tip Effects: Off
Proppant Type: Carbo-Lite


| | | |
|---|---|---|
| Young's Modulus | 50000 | MPa |
| Fracture Toughness | 0.81 | MPa·m^½ |
| Poisson's Ratio | 0.14 | fraction |
| Total Pay Zone Height | 0.03048 | m |
| Total Fracture Height | 150 | m |
| Ellipsoidal Aspect Ratio | 1 | |
| Injection Rate (2-wings) | 0.1 | m³/min |
| Flow Behavior Index - n' | 0.5 | |
| Consistency Index - K' | 0.04788 | kPa·s^n' |
| Total Leak-off Coefficient | 0 | cm/min^½ |
| Spurt Loss Coefficient | 0 | cm |
| Total Volume Injected | 2500 | m³ |
| Max Proppant Concentration | 17 | 100 kg/m³ |

## *Output Solution*

| Parameters | GDK | |
|---|---|---|
| Length | 461.13 | m |
| Height (wellbore) | 150 | m |
| Max. Well Width | 2.3009 | cm |
| Average Well Width | 2.3009 | cm |
| Average Fracture Width | 1.8071 | cm |
| Net Pressure | 810.43 | kPa |
| Efficiency | 1 | fraction |
| Pumping Time | 25000 | min |
| Volume | 2500 | m³ |
| Proppant Mass | 4.25E+06 | kg |
| Percent Propped | 99.186 | % |

# APPENDIX H

Sensitivity Analysis of the Pumping time

## *Input Data*

Input Volume
Turbulence: Off
Wall Roughness: Off
Tip Effects: Off
Proppant Type: Carbo-Lite

| | | |
|---|---|---|
| Young's Modulus | 50000 | MPa |
| Fracture Toughness | 0.81 | MPa·m^½ |
| Poisson's Ratio | 0.14 | fraction |
| Total Pay Zone Height | 1 | m |
| Total Fracture Height | 150 | m |
| Ellipsoidal Aspect Ratio | 1 | |
| Injection Rate (2-wings) | 0.8 | m³/min |
| Flow Behavior Index - n' | 0.5 | |
| Consistency Index - K' | 0.00479 | kPa·s^n' |
| Total Leak-off Coefficient | 0 | cm/min^½ |
| Spurt Loss Coefficient | 0 | cm |
| Total Volume Injected | 2500 | m³ |
| Max Proppant Concentration | 17 | 100 kg/m³ |

## *Output Solution*

| Parameters | GDK | |
|---|---|---|
| Length | 592.17 | m |
| Height (wellbore) | 150 | m |
| Max. Well Width | 1.7918 | cm |
| Average Well Width | 1.7918 | cm |
| Average Fracture Width | 1.4073 | cm |
| Net Pressure | 491.45 | kPa |
| Efficiency | 1 | fraction |
| Pumping Time | 3125 | min |
| Volume | 2500 | m³ |
| Proppant Mass | 4.25E+06 | kg |
| Percent Propped | 99.186 | % |

## *Input Data*

Input Volume
Turbulence: Off
Wall Roughness: Off
Tip Effects: Off
Proppant Type: Carbo-Lite

| | | |
|---|---|---|
| Young's Modulus | 50000 | MPa |
| Fracture Toughness | 0.81 | MPa·m^½ |
| Poisson's Ratio | 0.14 | fraction |
| Total Pay Zone Height | 1 | m |
| Total Fracture Height | 150 | m |
| Ellipsoidal Aspect Ratio | 1 | |
| Injection Rate (2-wings) | 0.7 | m³/min |
| Flow Behavior Index - n' | 0.5 | |
| Consistency Index - K' | 0.00479 | kPa·s^n' |
| Total Leak-off Coefficient | 0 | cm/min^½ |
| Spurt Loss Coefficient | 0 | cm |
| Total Volume Injected | 2500 | m³ |
| Max Proppant Concentration | 17 | 100 kg/m³ |

## *Output Solution*

| Parameters | GDK | |
|---|---|---|
| Length | 600.03 | m |
| Height (wellbore) | 150 | m |
| Max. Well Width | 1.7683 | cm |
| Average Well Width | 1.7683 | cm |
| Average Fracture Width | 1.3888 | cm |
| Net Pressure | 478.65 | kPa |
| Efficiency | 1 | fraction |
| Pumping Time | 3571.4 | min |
| Volume | 2500 | m³ |
| Proppant Mass | 4.25E+06 | kg |
| Percent Propped | 99.186 | % |

## *Input Data*

Input Volume
Turbulence: Off
Wall Roughness: Off
Tip Effects: Off
Proppant Type: Carbo-Lite

| | | |
|---|---|---|
| Young's Modulus | 50000 | MPa |
| Fracture Toughness | 0.81 | MPa·m^½ |
| Poisson's Ratio | 0.14 | fraction |
| Total Pay Zone Height | 1 | m |
| Total Fracture Height | 150 | m |
| Ellipsoidal Aspect Ratio | 1 | |
| Injection Rate (2-wings) | 0.6 | m³/min |
| Flow Behavior Index - n' | 0.5 | |
| Consistency Index - K' | 0.00479 | kPa·s^n' |
| Total Leak-off Coefficient | 0 | cm/min^½ |
| Spurt Loss Coefficient | 0 | cm |
| Total Volume Injected | 2500 | m³ |
| Max Proppant Concentration | 17 | 100 kg/m³ |

## *Output Solution*

| Parameters | GDK | |
|---|---|---|
| Length | 609.24 | m |
| Height (wellbore) | 150 | m |
| Max. Well Width | 1.7416 | cm |
| Average Well Width | 1.7416 | cm |
| Average Fracture Width | 1.3678 | cm |
| Net Pressure | 464.29 | kPa |
| Efficiency | 1 | fraction |
| Pumping Time | 4166.7 | min |
| Volume | 2500 | m³ |
| Proppant Mass | 4.25E+06 | kg |
| Percent Propped | 99.186 | % |


## *Input Data*

Input Volume
Turbulence: Off
Wall Roughness: Off
Tip Effects: Off
Proppant Type: Carbo-Lite


| | | |
|---|---|---|
| Young's Modulus | 50000 | MPa |
| Fracture Toughness | 0.81 | MPa·m^½ |
| Poisson's Ratio | 0.14 | fraction |
| Total Pay Zone Height | 1 | m |
| Total Fracture Height | 150 | m |
| Ellipsoidal Aspect Ratio | 1 | |
| Injection Rate (2-wings) | 0.5 | m³/min |
| Flow Behavior Index - n' | 0.5 | |
| Consistency Index - K' | 0.00479 | kPa·s^n' |
| Total Leak-off Coefficient | 0 | cm/min^½ |
| Spurt Loss Coefficient | 0 | cm |
| Total Volume Injected | 2500 | m³ |
| Max Proppant Concentration | 17 | 100 kg/m³ |

## *Output Solution*

| Parameters | GDK | |
|---|---|---|
| Length | 620.31 | m |
| Height (wellbore) | 150 | m |
| Max. Well Width | 1.7105 | cm |
| Average Well Width | 1.7105 | cm |
| Average Fracture Width | 1.3434 | cm |
| Net Pressure | 447.87 | kPa |
| Efficiency | 1 | fraction |
| Pumping Time | 5000 | min |
| Volume | 2500 | m³ |
| Proppant Mass | 4.25E+06 | kg |
| Percent Propped | 99.186 | % |

## *Input Data*

Input Volume
Turbulence: Off
Wall Roughness: Off
Tip Effects: Off
Proppant Type: Carbo-Lite

| | | |
|---|---|---|
| Young's Modulus | 50000 | MPa |
| Fracture Toughness | 0.81 | MPa·m^½ |
| Poisson's Ratio | 0.14 | fraction |
| Total Pay Zone Height | 1 | m |
| Total Fracture Height | 150 | m |
| Ellipsoidal Aspect Ratio | 1 | |
| Injection Rate (2-wings) | 0.4 | m³/min |
| Flow Behavior Index - n' | 0.5 | |
| Consistency Index - K' | 0.00479 | kPa·s^n' |
| Total Leak-off Coefficient | 0 | cm/min^½ |
| Spurt Loss Coefficient | 0 | cm |
| Total Volume Injected | 2500 | m³ |
| Max Proppant Concentration | 17 | 100 kg/m³ |

## *Output Solution*

| Parameters | GDK | |
|---|---|---|
| Length | 634.12 | m |
| Height (wellbore) | 150 | m |
| Max. Well Width | 1.6732 | cm |
| Average Well Width | 1.6732 | cm |
| Average Fracture Width | 1.3142 | cm |
| Net Pressure | 428.57 | kPa |
| Efficiency | 1 | fraction |
| Pumping Time | 6250 | min |
| Volume | 2500 | m³ |
| Proppant Mass | 4.25E+06 | kg |
| Percent Propped | 99.186 | % |


## *Input Data*

Input Volume
Turbulence: Off
Wall Roughness: Off
Tip Effects: Off
Proppant Type: Carbo-Lite


| | | |
|---|---|---|
| Young's Modulus | 50000 | MPa |
| Fracture Toughness | 0.81 | MPa·m^½ |
| Poisson's Ratio | 0.14 | fraction |
| Total Pay Zone Height | 1 | m |
| Total Fracture Height | 150 | m |
| Ellipsoidal Aspect Ratio | 1 | |
| Injection Rate (2-wings) | 0.3 | m³/min |
| Flow Behavior Index - n' | 0.5 | |
| Consistency Index - K' | 0.00479 | kPa·s^n' |
| Total Leak-off Coefficient | 0 | cm/min^½ |
| Spurt Loss Coefficient | 0 | cm |
| Total Volume Injected | 2500 | m³ |
| Max Proppant Concentration | 17 | 100 kg/m³ |

## *Output Solution*

| Parameters | GDK | |
|---|---|---|
| Length | 652.38 | m |
| Height (wellbore) | 150 | m |
| Max. Well Width | 1.6264 | cm |
| Average Well Width | 1.6264 | cm |
| Average Fracture Width | 1.2774 | cm |
| Net Pressure | 404.92 | kPa |
| Efficiency | 1 | fraction |
| Pumping Time | 8333.3 | min |
| Volume | 2500 | m³ |
| Proppant Mass | 4.25E+06 | kg |
| Percent Propped | 99.186 | % |

## *Input Data*

Input Volume
Turbulence: Off
Wall Roughness: Off
Tip Effects: Off
Proppant Type: Carbo-Lite

| | | |
|---|---|---|
| Young's Modulus | 50000 | MPa |
| Fracture Toughness | 0.81 | MPa·m^½ |
| Poisson's Ratio | 0.14 | fraction |
| Total Pay Zone Height | 1 | m |
| Total Fracture Height | 150 | m |
| Ellipsoidal Aspect Ratio | 1 | |
| Injection Rate (2-wings) | 0.2 | m³/min |
| Flow Behavior Index - n' | 0.5 | |
| Consistency Index - K' | 0.00479 | kPa·s^n' |
| Total Leak-off Coefficient | 0 | cm/min^½ |
| Spurt Loss Coefficient | 0 | cm |
| Total Volume Injected | 2500 | m³ |
| Max Proppant Concentration | 17 | 100 kg/m³ |

## *Output Solution*

| Parameters | GDK | |
|---|---|---|
| Length | 678.98 | m |
| Height (wellbore) | 150 | m |
| Max. Well Width | 1.5627 | cm |
| Average Well Width | 1.5627 | cm |
| Average Fracture Width | 1.2273 | cm |
| Net Pressure | 373.81 | kPa |
| Efficiency | 1 | fraction |
| Pumping Time | 12500 | min |
| Volume | 2500 | m³ |
| Proppant Mass | 4.25E+06 | kg |
| Percent Propped | 99.186 | % |


## *Input Data*

Input Volume
Turbulence: Off
Wall Roughness: Off
Tip Effects: Off
Proppant Type: Carbo-Lite


| | | |
|---|---|---|
| Young's Modulus | 50000 | MPa |
| Fracture Toughness | 0.81 | MPa·m^½ |
| Poisson's Ratio | 0.14 | fraction |
| Total Pay Zone Height | 1 | m |
| Total Fracture Height | 150 | m |
| Ellipsoidal Aspect Ratio | 1 | |
| Injection Rate (2-wings) | 0.1 | m³/min |
| Flow Behavior Index - n' | 0.5 | |
| Consistency Index - K' | 0.00479 | kPa·s^n' |
| Total Leak-off Coefficient | 0 | cm/min^½ |
| Spurt Loss Coefficient | 0 | cm |
| Total Volume Injected | 2500 | m³ |
| Max Proppant Concentration | 17 | 100 kg/m³ |

## *Output Solution*

| Parameters | GDK | |
|---|---|---|
| Length | 726.94 | m |
| Height (wellbore) | 150 | m |
| Max. Well Width | 1.4596 | cm |
| Average Well Width | 1.4596 | cm |
| Average Fracture Width | 1.1464 | cm |
| Net Pressure | 326.11 | kPa |
| Efficiency | 1 | fraction |
| Pumping Time | 25000 | min |
| Volume | 2500 | m³ |
| Proppant Mass | 4.25E+06 | kg |
| Percent Propped | 99.186 | % |